

Dissertation
submitted to the
Combined Faculties of the Natural Sciences and Mathematics
of the Ruperto-Carola-University of Heidelberg, Germany
for the degree of
Doctor of Natural Sciences

Put forward by

ARIANNA MUSSO BARCUCCI

born in Moncalieri, Italy

Oral examination: 23 July 2020

THE RELATION BETWEEN DISCS
AND YOUNG COMPANIONS
-
OBSERVATIONAL STUDIES

REFEREES:

PROF. DR. THOMAS HENNING

PROF. DR. KEES DULLEMOND

ABSTRACT

The direct imaging technique brings advantages with respect to other, indirect methods of detecting planets. It is sensitive to larger separations, it can detect companions on a variety of orbital configurations, and it allows to simultaneously image both a companion and the circumstellar disc it resides in, thus being the perfect tool to study companion-disc interactions. Direct observations of $H\alpha$ emission from young planetary and low-mass stellar companions can also shed light on the early gas accretion phase of planet formation. In this Thesis I use the direct imaging technique to study various aspects of planet-disc interaction and planet formation and evolution. I present the detection of a previously unknown low-mass stellar companion around HD 193571, observed as part of the NaCo Imaging Survey for Planets around Young Stars (ISPY). The companion appears to reside within the gap between the host star and its surrounding disc, making this the third low-mass stellar companion discovered within a debris disc. This system is thus the perfect laboratory where to study the relative importance between self- and companion-stirring models in discs.

I also present the detection of $H\alpha$ emission from the known substellar companion around the young star PZ Tel. The derived $H\alpha$ luminosity, combined with age and disc information, indicates that the emission is likely due to chromospheric activity of the companion. This detection further proves the capability of using high-contrast imaging instruments and techniques to detect $H\alpha$ signatures from companions around young stars.

On a larger scale, I present the L' band Imaging Survey to find Exoplanets in the North (LIStEN), which targeted ~ 30 nearby stars with known and well characterised circumstellar discs. LIStEN focuses on characterising the population of wide-orbit giant planets around disc-hosting stars, as well as studying the intricacies of companion-disc interactions. I present the survey's scientific goals, data selection and observational strategy, as well as the data reduction and analysis. No new planetary companions were detected, and the mass detection limits derived from the observations are combined with information on the disc size and morphology to constrain the presence of unseen planetary and low-mass stellar companion around these disc-hosting stars.

ZUSAMMENFASSUNG

Die Methodik der direkten Beobachtung hat Vorteile gegenüber anderen, indirekten Methoden zum Nachweis von Exoplaneten. Sie ist empfindlicher für größere Separationen, kann planetare und stellare Begleitobjekte auf einer Vielzahl von Bahnkonfigurationen nachweisen, und erlaubt es, gleichzeitig sowohl ein Begleitobjekt als auch die zirkumstellare Scheibe abzubilden, was diese Methodik zum perfekten Werkzeug zur Untersuchung von Wechselwirkungen zwischen dem Begleiter und der Scheibe macht. Die direkte Beobachtung der $H\alpha$ -Emission von jungen planetaren und massearmen stellaren Begleitern kann zudem Aufschluss über die frühe Gasakkretionsphase der Planetenbildung geben. In dieser Dissertation verwende ich die Methodik der direkten Beobachtung, um verschiedene Aspekte der Planeten-Scheiben-Wechselwirkung und der Entstehung und Entwicklung von Planeten zu untersuchen. Ich präsentiere den Nachweis eines bisher unbekanntes massearmen stellaren Begleiters um HD 193571, der im Rahmen der NaCo “Imaging Survey for Planets around Young Star” (ISPY) Beobachtungskampagne entdeckt wurde. Der Begleiter befindet sich in der Lücke zwischen dem Zentralstern und der ihn umgebenden Scheibe; dieses massearme stellare Begleitobjekt ist bislang erst das dritte, das in einer Trümmerscheibe entdeckt wurde. Dies macht dieses System daher zum idealen Kandidaten zur Untersuchung der relativen Bedeutung von Eigen- und Fremdanregung bei der Entstehung und Entwicklung von Trümmerscheiben. Ich präsentiere des Weiteren eine Detektion von $H\alpha$ Emission für das bekannte substellare Begleitobjekt um den jungen Stern PZ Tel. Die hergeleitete $H\alpha$ Leuchtkraft, kombiniert mit Informationen über das Alter und die Scheibe, weist darauf hin, dass die Emission wahrscheinlich auf die chromosphärische Aktivität des Begleiters zurückzuführen ist. Diese Entdeckung ist ein weiterer Nachweis, dass Instrumente und Techniken zur Abbildung mit hohem Kontrast großes Potential haben, $H\alpha$ -Signaturen von Begleitern um junge Sterne zu entdecken. Schließlich präsentiere ich Ergebnisse der Beobachtungskampagne “L’ band Imaging Survey to find Exoplanets in the North” (LISStEN), welche ~ 30 nahe Sterne mit bekannten und gut charakterisierten zirkumstellaren Scheiben beinhaltet. LISStEN konzentriert sich auf die Charakterisierung der Population von Riesenplaneten mit großer Umlaufbahn in zirkumstellaren Scheiben von Sternen sowie auf die Untersuchung der Wechselwirkungen zwischen Begleiter und Scheibe. Ich diskutiere die wissenschaftlichen Ziele der Studie, die Auswahl der Objekte und Beobachtungsstrategie, sowie die Analyse und Reduktion der Beobachtungsdaten. Obwohl keine neuen Planeten entdeckt wurden, kann ich die aus den Beobachtungen abgeleiteten Grenzen für die Masse von Begleitobjekten in Kombination mit Informationen über die Größe und Morphologie der Scheiben benutzen um die Präsenz von nicht detektierten planetaren oder massearmen stellaren Begleitern in den Stern-Scheiben-Systemen einzuschränken.

Ai miei genitori...

LIST OF FIGURES	xiii
LIST OF TABLES	xv
List of Abbreviations	xvii
1 Introduction	1
1.1 Planets and where to find them	2
1.1.1 Circumstellar discs	3
1.1.2 Detection techniques	4
1.1.3 Current state of the field	6
1.2 Direct imaging	7
1.2.1 Advantages and drawbacks	7
1.2.2 Direct imaging observations	9
1.3 What can we learn from direct imaging?	9
1.3.1 Companion-disc interaction	9
1.3.2 H α emission from low-mass stellar companions	11
1.3.3 Direct imaging surveys	12
1.3.3.1 The NaCo-ISPY and the LISStEN survey	14
1.4 Thesis outlook and scope	15
2 ISPY - NaCo Imaging Survey for Planets around Young stars	
Discovery of an M dwarf in the gap between HD 193571 and its debris ring	17
2.1 Introduction	17
2.2 HD 193571	18
2.3 Observations and data reduction	20
2.3.1 VLT/NaCo	20
2.3.2 Gemini/GPI	20
2.4 Analysis and results	22
2.4.1 Astrometry and photometry	22
2.4.2 Physical properties	25
2.4.3 Orbital motion	26
2.5 Stirring mechanisms	27

2.6	Conclusions	30
3	Detection of Hα emission from PZ Tel B using SPHERE/ZIMPOL	33
3.1	Introduction	33
3.2	PZ Tel B	33
3.3	Observations and data reduction	35
3.4	Analysis and results	36
3.4.1	Astrometry and flux contrast	37
3.4.2	Photometry	37
3.4.3	Orbital constraints	38
3.5	Discussion and conclusions	42
4	LIStEN - the L' band Imaging Survey to find Exoplanets in the North	45
4.1	Introduction	45
4.2	Target Selection	46
4.2.1	Target master list	46
4.2.2	Notes on individual targets	47
4.2.2.1	HD 206860	48
4.2.2.2	HD 183324, HD 191174 and HD 192425	48
4.2.2.3	HD 48682, HD 143894, HD 161868, HD 212695 and HD 127821	49
4.2.2.4	HD 110897	49
4.2.2.5	HD 50554	49
4.2.2.6	HD 8907	50
4.2.2.7	HIP 83043	50
4.2.2.8	HD 128311	50
4.2.2.9	HD 113337	51
4.3	Observations	53
4.4	Data Reduction & Analysis	53
4.4.1	Data processing	53
4.4.2	PynPoint analysis	56
4.4.3	Contrast curves & Mass limits	57
4.4.4	Infrared excess characterisation	60
4.5	Planetary constraints and disc analysis	61
4.5.1	Self-stirring analysis	61
4.5.2	Double-belt analysis	64
4.5.3	Planetary constraints from proper motion anomaly	66
4.6	Conclusions	72
5	Summary and future perspective	75
5.1	Summary	75
5.2	Future perspective	77
5.2.1	Follow-up observations	77
5.2.2	A large and coherent H α survey	77
5.2.3	Deepening our understanding of companion-disc interaction	78
A	Supplementary material for Chapter 2	81

A.1	IRDIS disc non-detection	81
A.2	Stirring mechanisms	82
A.3	Orbital constraints with OFTI	84
B	Supplementary material for Chapter 3	87
B.1	Angular spectral differential imaging	87
B.2	Photometry	88
B.3	Alternative Photometric Analysis	89
C	Supplementary material for Chapter 4	91
C.1	Master flat and bad pixel mask creation	91
C.2	Stacked VS unstacked frames	92
	Bibliography	99
	Publications	107
	Acknowledgements	110

List of Figures

1.1	Overview of the different detection methods and their parameter space: companion mass VS semi-major axis for a subset of all the confirmed exoplanets so far.	4
1.2	The directly imaged multi-planetary system around HR 8799. Figure originally published in Marois et al. (2010)	10
2.1	Spectral energy distribution of HD 193571.	19
2.2	ADI NaCo and GPI observations of HD 193571: detection of an M-dwarf companion.	22
2.3	Proper motion analysis of the newly discovered companion around HD 193571: confirming co-motion with the host star.	24
2.4	GPI spectrum of the companion around HD 193571: comparison with observed spectra of early M dwarfs.	25
2.5	Colour-magnitude diagram for the HD 193571 companion: comparison with BT-Settl evolutionary tracks.	26
2.6	Stirring analysis for the disc around HD 193571: testing the self-stirring VS companion-stirring hypothesis.	29
3.1	SPHERE/ZIMPOL observations of PZ Tel B in the continuum and narrow-band H α filter.	36
3.2	Updating the orbital analysis of PZ Tel B: position angles and separations at various epochs.	39
3.3	Updating the orbital analysis of PZ Tel B: best orbital solution found with PyAstrOFit.	40
3.4	Updating the orbital analysis of PZ Tel B: posterior distributions of the orbital elements.	42
4.1	Age, distance and spectral type distributions for all the L $IStEN$ targets.	48
4.2	Example of data reduction for the L $IStEN$ survey: ADI reduced images of HD 206860.	57
4.3	Contrast curves for all the DD-hosting L $IStEN$ targets.	58
4.4	L $IStEN$ survey detection probability as a function of companion mass and semi-major axis.	59
4.5	Example of SED fitting for the L $IStEN$ survey: HD 50554.	60
4.6	Self-stirring analysis for the single belt debris discs systems in the L $IStEN$ survey.	63

4.7	Self-stirring analysis for the double belts debris discs systems in the L ^I StEN survey.	64
4.8	Visualisation of the minimal planetary system that can carve a disc gap. Figure originally published in Shannon et al. (2016) .	65
4.9	Visualisation of the proper motion anomaly concept. Figure originally published in Kervella et al. (2019) .	67
4.10	Analysis of the proper motion anomaly for HD 161868.	70
4.11	Analysis of the proper motion anomaly for HD 8907.	71
4.12	Analysis of the proper motion anomaly for HD 113337.	71
A.1	SPHERE/IRDIS observations of HD 193571: disc non-detection.	82
C.1	Posterior distribution function for the orbital parameters of the companion around HD 193571.	84
C.1	Comparison between the 5σ detection limits achieved using the unstacked and stacked frames for all the DD-hosting targets in the L ^I StEN survey.	93
C.2	SED fitting for all the DD-hosting targets in the L ^I StEN survey.	94
C.3	ADI reduced images for all the DD-hosting targets in the L ^I StEN survey observed in single-sided mode.	95
C.4	ADI reduced images for all the DD-hosting targets in the L ^I StEN survey observed in double-sided mode.	96
C.5	ADI reduced images for all the DD-hosting targets in the L ^I StEN survey observed in double-sided mode: continuation.	97

List of Tables

2.1	Fundamental stellar parameters and properties for HD 193571.	18
2.2	VLT/NaCo summary of observations	21
2.3	Astrometry and photometry of the companion candidate for all three datasets	23
3.1	Fundamental parameters and properties of the PZ Tel system.	34
3.2	Summary of observations and detector characteristics.	35
3.3	Astrometry and flux contrast evaluated with <i>ANDROMEDA</i> , for both continuum and narrow band filter.	37
3.4	Astrometric measurements for PZ Tel B available in the literature	39
3.5	Best solutions in terms of reduced χ^2 and $1 - \sigma$ confidence intervals for all the orbital elements. These orbital elements have an associated χ_{red}^2 of 2.15.	41
4.1	LIStEN survey: summary of targets parameters	47
4.2	LIStEN survey: summary of resolved discs and hosted planets	51
4.3	LIStEN survey: summary of observations	52
4.4	Disc parameters from SED fitting	61
4.5	Minimal planetary system parameters	66
4.6	Proper Motion anomaly values	69
C.1	5σ contrast curves and mass detection limits for all the LIStEN targets	95

List of Abbreviations

ADI	Angular Differential Imaging	IWA	Inner Working Angle
ADU	Analog to Digital Unit	LBT	Large Binocular Telescope
AGPM	Annular Groove Phase Mask	LMIRCam	L/M-band mid-InfraRed Camera
AO	Adaptive Optics	MCMC	Markov Chain Monte Carlo
ASDI	Angular Spectral Differential Imaging	PA	Position Angle
		PCA	Principal Component Analysis
BB	Black Body	PMa	Proper Motion anomaly
DD	Debris Disc	PPD	ProtoPlanetary Disc
DI	Direct Imaging	PSF	Point Spread Function
FPF	False Positive Fraction	RV	Radial Velocity
FWHM	Full Width at Half Maximum	SED	Spectral Energy Distribution
GP	Giant Planet	VLT	Very Large Telescope
GPI	Gemini Planet Imager	ZIMPOL	Zurich Imaging POLarimeter
IR	InfraRed		

1

Introduction

Based on work published in [Musso Barcucci et al. 2019a](#) and in [Musso Barcucci et al. 2019b](#).

3549

This is the number of confirmed extrasolar planets that had been discovered when I started my PhD, and by the time I am submitting this Thesis this number has grown to 4264 confirmed planets, and it keeps increasing¹.

The field of exoplanets grew rapidly from the first discoveries in the early 1990s, developing new techniques to detect planets, and new algorithms, theories and models to understand them. After the first planetary companions were discovered (the multiplanetary system around the millisecond pulsar PSR B1257+12 by [Wolszczan & Frail 1992](#) and the planetary companion around the main sequence star 51 Pegasi by [Mayor & Queloz 1995](#)), more and more detections showed a wide range of objects, composing a rich zoology of planetary systems. From single Jupiter-like planets orbiting single main sequence stars, to multiplanetary systems of 6 or more Earth-like objects in a tightly packed orbit (see, e.g.: TRAPPIST 1, [Gillon et al. 2017](#)), to exoplanets orbiting around binary stars, to even wilder and weirder worlds of free-floating planets (orphan objects without a

¹Data from the Extrasolar Planets Encyclopaedia at <http://exoplanet.eu>

parent star, wandering around in space, like the Jupiter-sized planet PSO J318.5-22 discovered by [Liu et al. 2013](#)), and even a planet tidally locked to its star with a never-ending day side where metals evaporate and an eternal night side where it rains iron (the strange world of Wasp-76b, see [Ehrenreich et al. 2020](#); [West et al. 2016](#)).

While the final goal for many astronomers and scientists is to find the so-called “Earth 2.0”, an Earth-like planet orbiting a Sun-like star and capable of hosting life as we know it, there are many more aspects of exoplanetary science that are inherently interesting: the intricacies of planet formation and evolution, the complexity of their internal structures and atmospheres, the variety of their morphology and orbital characteristics, and the diverse ways they can interact both among each other, and with the disc and stellar environment they reside in. This sparked a fast growing network of inter-related sub-fields dedicated to understanding various aspects of the exoplanetary puzzle, deploying various detection techniques and tools.

This Thesis focuses on the direct imaging technique for detecting exoplanets, and on the specific sub-set of questions that this method can help addressing.

1.1 Planets and where to find them

The concept of ‘planet’ is not easily defined and various suggestions have been made. A widely used one is a mass-based definition, where a planet is an object with a true mass inferior to the minimum mass required for thermonuclear fusion of deuterium, commonly set at 13 Jupiter masses. This definition, while being classically widespread in the community, is by no means the only one, and it has the drawback of being variable, since the deuterium burning mass depends on the planet composition and accretion history. [Soter 2006](#) suggested a different definition based on the formation mechanism, in which a planet is an object formed by the accretion of material in a circumstellar disc, while a star is formed by disc fragmentation under gravitational collapse. This definition places the upper limit for a planet mass between ~ 25 to 30 Jupiter masses, but being able to distinguish between these two formation scenarios is not always easy.

While low-mass objects can be more intuitively labelled as ‘planets’, the classification becomes more challenging for objects with limiting masses, the so-called giant planets (GP’s). For these objects it can be difficult to ascertain the planetary status, either because their true mass is uncertain or because their formation scenario cannot be clearly established. For this reason, throughout this Thesis I will often refer to objects whose status is unclear as ‘companions’, a term that refers to a body orbiting a star more massive than itself, and that encompasses planets, brown dwarfs and stellar companions.

In the following sections I will give an overview of circumstellar discs (which are thought to be the birthplaces of planets), of the various observational techniques and detection methods used to

detect planetary and low-mass stellar companions, as well as a brief overview of the current state of the exoplanetary field.

1.1.1 Circumstellar discs

Circumstellar discs are the natural by-products of the protostellar accretion process and they are the birthplaces of planetary systems. The initial protoplanetary discs (PPD's) are remnants of stellar formation and tend to have a high gas-to-dust ratio. The material that form them dissipates over time through several processes, like photoevaporation, stellar winds, agglomeration on solid bodies, and accretion onto the central star or onto a forming companion. The last one is an important step in the early phases of planetary formation, and can be studied through $H\alpha$ observations (see Section 1.3.2).

The original PPD usually disappears within ~ 10 Myr (Ercolano & Pascucci 2017). After that, a new generation of dust is created and continuously replenished via planetesimal collisions, forming a second generation debris disc (DD), often found around older (> 10 Myr) stars. However, distinguishing between these two classes of circumstellar discs is not always straightforward, since both PPD's and DD's have been found to coexist in the age range of ~ 5 to 15 Myr. Another criterion often used to distinguish between the two is the fractional luminosity of the disc with respect to the host star ($f = L_{\text{disc}}/L_{\star}$) which is a proxy for the optical depth: DD's are optically thin while PPD's tend to be optically thick (particularly at optical wavelengths). The exact boundary is again not easy to define, and lies between 10^{-3} and 10^{-2} (see, e.g.: Hughes et al. 2018 and Wyatt et al. 2015).

The presence of a DD around a star is usually inferred via its spectral energy distribution (SED), since the material in the disc scatters the light from the host star and shows up as an 'infrared excess' in the SED. This excess can be modelled to characterise the disc in terms of its fractional luminosity, its radial distance from the star, the average temperature of its debris components, and the grain size distribution. Multi-component models are sometimes required to fit the SED, and point to the presence of two belts: an inner, warm one and an outer and cold one, analogous to the exozodiacal dust and the Kuiper belt in the Solar System. More and more DD's are being detected and sometimes resolved in their scattered light, using dedicated telescope facilities like the Atacama Large Millimeter Array (ALMA) in Chile. These resolved images are showing a variety of radial distances from their host star (up to hundreds of au) and physical extents, as well as interesting features such as spirals, gaps, and belts, which are thought to be signpost of planetary formation. Discs and companions can interact in a variety of ways, for example with the companion stirring the planetesimals and carving gaps in the disc (see Section 1.3.1).

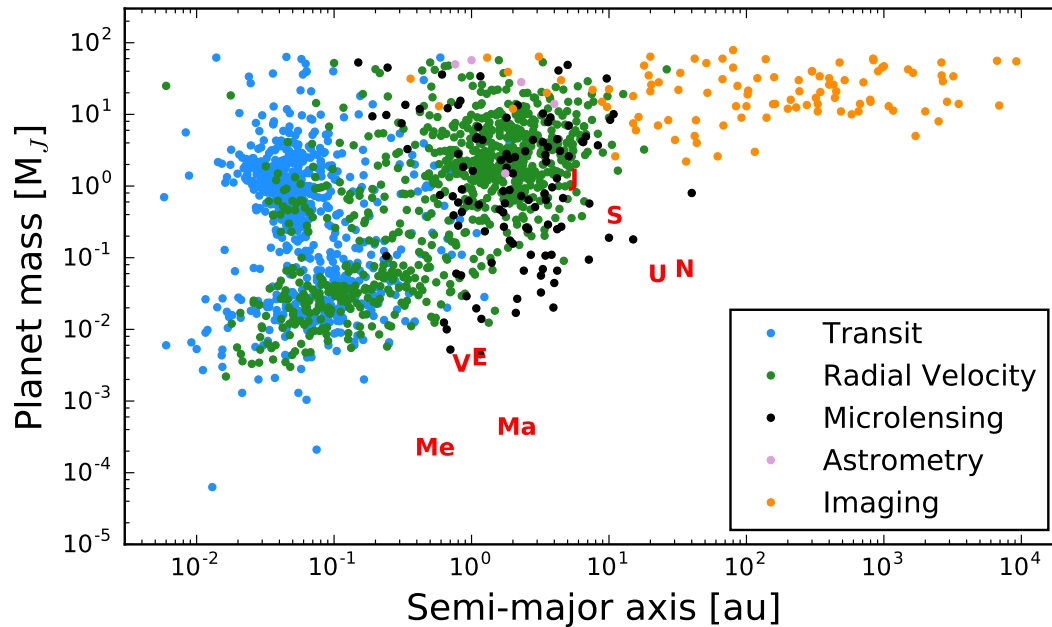


Figure 1.1: Companion mass in Jupiter masses versus semi-major axis in astronomical units for a subset of all the confirmed planetary or low-mass stellar companions discovered so far. The different colours indicate the primary method of discovery, and the bold red letters indicate the Solar System planets. For companions discovered with the RV method (green dots) I plot the $m_p \sin i$ mass estimate. The data comes from the Extrasolar Planets Encyclopaedia¹. We excluded objects for which an estimate of the mass or of the semi-major axis was not available.

1.1.2 Detection techniques

Planets can be detected using various techniques, each with its own advantages, drawbacks and biases. A detailed analysis of all of these methods is beyond the scope of this Thesis, and in the following I simply summarise the main techniques and the physical principles behind them, as well as underlying their general strengths and challenges.

- **Transit**

The most prolific detection method is the transit technique, which relies on detecting the dip in luminosity of the host star due to the passage of a companion in front of it (with respect to the observer), which obstructs part of the stellar light. Measuring this change in brightness can give information on the relative ratio between the host star and the companion radius, which can be translated into a mass estimate assuming a given density. By design, this technique favours companions on edge-on orbits, high planet-to-star radius ratio, and nearby systems. Since multiple transits are often required to confirm a detection, this technique is biased towards companions with a short orbital period, often of a few months or less.

- **Radial velocity**

The second most prolific detection method is the radial velocity technique (RV), which takes advantage of the gravitational pull that a companion exerts on its host star and the consequent Doppler shift in its spectrum due to the star orbiting around the common centre of mass. The lines in the spectrum of the host star are periodically red-shifted (when the star is moving away from the observer) or blue-shifted (when it is moving towards the observer). The amplitude of these variations depends on the companion's eccentricity, period, mass and orbital inclination, and on the host star's mass. This technique relies on the capability of modelling the stellar spectrum and detecting tiny shifts in its lines, and therefore favours somewhat old and calm stars, with slow-rotation (to avoid line broadening) and no surface inhomogeneities or other stellar activities, which would complicate the observations. The mass of the companion can be estimated only as a lower limit, due to the unknown inclination of the orbit on the sky (the RV amplitude signal being strongest for edge-on orbits, and zero for face-on ones). This technique is biased towards high planet-to-stellar mass ratio, high eccentricity orbits and small orbital periods. The RV signal yielded the first detection of a planetary companion around a main sequence star in 1995, when [Mayor & Queloz \(1995\)](#) discovered a Jupiter mass planet around 51 Pegasi.

- **Astrometry**

Another method of detecting planets is the astrometry technique, which relies on the misalignment between the stellar centre of mass and the system centre of mass, due to the gravitational pull of a companion. Detecting the movement of the star on the sky around this common centre of mass can hint at the presence of an unseen companion. The astrometry signal is dependent on the mass ratio between the companion and the host star, and decreases with the distance of the system. Given the inherent difficulty of detecting very small stellar misplacements (of the order of less than a milliarcsecond), this technique has so far proved less effective than the transit or the RV method.

- **Microlensing**

Worth mentioning is the microlensing technique, with which a planet can be detected through the distortions that its gravitational field induces on the light of a background star. This technique is, opposed to the previous ones, independent of the host star mass, age, or brightness, and can therefore probe a complementary parameter space with respect to the other methods. However, relying mostly on chance alignments, it can typically provide only single measurements and does not allow for follow-up observations.

- **Direct imaging**

All of the aforementioned techniques are 'indirect' ones, since they infer the presence of a planet through the influence that it has on its host star, as opposed to the direct imaging technique, which is the focus of this Thesis and is detailed in Section 1.2.

All of these detection methods, whether direct or indirect, have yielded important results, probing different parameter spaces and answering various questions about the formation, evolution, morphology and demographics of exoplanets. A sub-set of all the detected planets so far is shown in Figure 1.1, where each symbol depicts a different detection technique. This plot is classically used to illustrate the variety of planets discovered so far, with semi-major axis spanning from a fraction to several hundreds of au, and masses encompassing three orders of magnitude. All of these detections are slowly coming together to paint a picture of the exoplanet population in our Galaxy, an overview of which is given in the following section.

1.1.3 Current state of the field

A good overview of the current knowledge of exoplanet occurrence rate and architecture can be found in, e.g. [Winn & Fabrycky \(2015\)](#) and [Perryman \(2018\)](#). In this section, I simply summarise in broad brushstrokes the main exoplanet findings so far in terms of demographics, population and architecture. More data and more work is continuously being put into comprehending these results, which should be merely viewed as the current understanding based on the data gathered so far, and might change or even be dismissed as our understanding of exoplanetary science deepens.

Combining results from various surveys and detection techniques, the current picture seems to be the following: occurrence rate decreases strongly with planetary mass, with giant planets being less abundant than their smaller counterparts, and objects between a few tens up to 80 Jupiter mass orbiting within 3 to 5 au from their host star being exceedingly rare, a phenomenon labelled as the ‘brown dwarf desert’. One of the findings of the RV technique is that low mass planets (i.e. less than $0.1 M_J$) are more frequently found around low mass stars and seem to prefer multiplanetary systems. Transit observations indicate that there is a trend of lower mass planets to be interior to high mass ones in multiplanetary systems, as well as an anti-correlation between system multiplicity and eccentricities. This seems to be in agreement with the GP population having a broader eccentricity distributions (ranging from 0 to 0.9) and preferring single planet systems, while low mass planets tend to have lower eccentricities (≤ 0.1) and tend to be found in multiplanetary systems.

Up to one in two Sun-like stars is thought to harbour several small planets with short periods (within 1 year), while only around $\sim 10\%$ would be expected to host a giant planet. Super earths and Neptune-like planets seem also to be common, with up to 50% of G and K dwarfs hosting one.

The direct imaging technique can constraint GP’s on wide orbit, and the current findings seems to indicate that these types of objects are rare, with an occurrence rate of $\sim 1\%$ (see Section 1.3.3).

1.2 Direct imaging

In this section I give an overview of the direct imaging technique (DI), which aims at directly observing the photons from the companion, either as reflected light from the host star or as the companion's own thermal emission (self-luminous planet).

The main challenges for DI are posed by the relatively small projected separation on sky between the companion and the host star, which favours nearby systems with planets on wide orbits, and the unfavourable planet to star light ratio (with typical values ranging between 10^{-5} in the infrared to 10^{-10} in the optical), which favours self-luminous giant planets (with the current facilities and post-processing techniques, at the moment of writing DI can only detect self-luminous planets).

The brightness of a self-luminous GP will decrease over time while the planet cools radiatively releasing the heat generated during its formation and gravitational contraction, and so a GP is more bright at an early stage. Moreover, the host star's brightness will reach a plateau on the main sequence, while the GP brightness will keep decreasing over time, and so the planet to star brightness ratio is more favourable at an early stage. For these reasons, the best targets for the direct imaging technique are young, nearby stars.

1.2.1 Advantages and drawbacks

The DI technique offers a unique opportunity to probe a complementary parameters space with respect to the other indirect detection techniques, as it is shown in Figure 1.1. Both the transit and the RV techniques are biased towards short period planets, while DI favours companions on wide-orbits. Moreover, the DI technique is capable of detecting objects in a variety of orbital configurations, including face-on orbits which are not detectable with the other two most successful indirect methods. Another advantage lays in the capability of DI of observing very young systems, where the host star might not have reached the main sequence yet, and stellar activity might be high: this is a unique opportunity of studying the very early stages of planetary formation, with groundbreaking discoveries such as PDS 70 b (Keppler et al. 2018) where a planetary mass object was imaged while still embedded in its protoplanetary disc. Direct imaging also allows to observe systems where a companion and a circumstellar disc can be imaged and studied at the same time, casting light on the intricacies of companion-disc interaction (see Section 1.3.1). Directly detecting the photons of a companion also allows us to study its atmosphere, a rapidly growing sub-field of exoplanetary science.

However, this technique is by no means flawless or unbiased: DI cannot probe the lower-mass end of the planet population, where the companion-to-star light contrast is too unfavourable. To try to compensate for this, DI observations are preferably carried out in the infrared part of the spectrum, where the stellar emission decreases while the thermal emission from the planet

increases. However, the angular resolution of a telescope Θ (which dictates the closest angular separation at which two point sources can be distinguished) behaves as:

$$\Theta = 1.22 \frac{\lambda}{D}$$

With D being the telescope diameter and λ being the observed wavelength. This implies that at longer wavelengths the angular resolution gets worse, and so does the closest angular separation from the host star at which a companion could be resolved (often referred to as the inner working angle, IWA), meaning that only wide-orbit objects can be detected.

Even in the case of a detection, multi-epoch observations are required to confirm (or deny) that the observed object is gravitationally bound to its host star, as opposed to being a background star that happens to be in the field of view. For this reason, high-proper motion stars are often good targets for DI observations, though even in the best scenario several months are often needed as baseline between follow-up observations before any detectable movement is seen.

The main directly observable quantity that can be obtained with DI is the magnitude contrast between the companion and the host star, in a given band. With distance information, as well as photometric information about the host star, this contrast can be translated into an absolute magnitude for the companion. Planetary evolutionary models (see, e.g., [Allard et al. 2012](#); [Baraffe et al. 2002](#)) predict, at a given age and for a given mass, the photometry of the planet in various bands; using the observed magnitude and the information on the system age it is then possible to infer a mass for the companion.

There are of course several assumptions involved: the brightness at a given age and for a given mass can vary wildly based on the chosen initial conditions for the formation scenario, the stellar age can be a challenging parameter to estimate and its uncertainty dominates the uncertainty on the inferred mass and, finally, the exact epoch of planet formation with respect to the stellar age is often unknown, but it tends to be less of an issue for intermediate and older age stars since the difference becomes negligible. Other uncertainties include atmospheric models of the planet and planet composition, which can impact the radiative cooling behaviour of an object and thus its luminosity evolution.

The most model-independent and robust way of assessing the mass of a companion would be via gravitational interaction with other objects and/or with its host star. However, the dynamical timescales involved are unfavourable for far away planets, for which several years of observations would cover only a fraction of their orbits. Combining RV observations (which provide lower limits estimate for the mass) and DI observations would also help in this regard, which is why improving the instrumentation and tools for DI observations to push the accessible parameter space more and more towards the RV dominated regime is important.

1.2.2 Direct imaging observations

Even in the best conditions, the direct observation of a companion orbiting a star would still be dominated by the stellar luminosity. This can be mitigated at an instrumental level, using a coronagraph to suppress the light from the central star, at an observational level, with the angular differential imaging (ADI) technique, and at a data processing level, using algorithms like PynPoint (Amara & Quanz 2012; Stolker et al. 2019) and *ANDROMEDA* (Cantalloube et al. 2015) to model and subtract the point spread function (PSF) of the central star in each observed image.

In the ADI technique (see Marois et al. 2006) the observations are carried out in pupil stabilised mode, so that in each frame the field of view (and every physical signal in it) is allowed to rotate, while the PSF patterns and the instrument and telescope-dependent speckles are in a fixed position. The PSF and speckle pattern can then be modelled and subtracted from each frame (using various post-processing algorithms) so that a companion signal, if present, can be more easily recovered. Observations are often carried out during the meridian passage of the star, to optimise the total field rotation achieved.

There are additional telescope and instrument-dependent issues to be taken into account while performing DI observations, like the adaptive optic system-dependent brightness range for the star, or the necessity to avoid close-in binaries with similar magnitude (which brightness might saturate the observations), among others.

1.3 What can we learn from direct imaging?

The direct imaging technique offers a unique opportunity to deepen our knowledge on various aspects of exoplanetary science, and this Thesis focuses on three of them: understating companion-disc interaction, gaining information on the gas-accretion phase in the early-stages of planet formation through $H\alpha$ observations, and augmenting the sample of detected GP's via dedicated exoplanet survey(s) to better understand their demographics in the broader context of planet population.

1.3.1 Companion-disc interaction

Debris disc are formed of second-generation material that is created and replenished via planetesimal collisions. These destructive encounters are triggered when the planetesimals are dynamically excited such that their relative velocities increase above a critical value (low-velocity collisions can happen in non-excited DDs as well, but they produce a different and recognisable emission spectrum, see Heng & Tremaine 2010). Three possible stirring processes have been

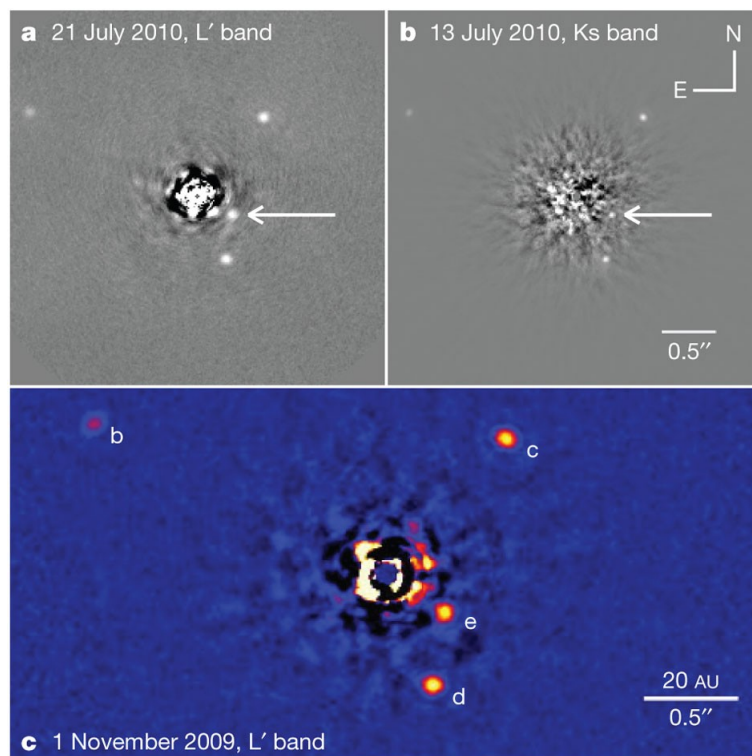


Figure 1.2: Detection of the multi-planetary system around HR 8799, in three different epochs and two different bands (L' and Ks). All the four planets are visible and marked with different letters. Figure originally published in [Marois et al. \(2010\)](#).

proposed so far that could induce such an excitation in the disc: stellar encounters, self-stirring and companion-stirring. Of these three, the first scenario is the least likely one to be observed, since close stellar encounters are rare (particularly among field stars) and the disc brightness resulting from dust production drops too quickly to be detectable ([Kenyon & Bromley 2002](#)). In the self-stirring scenario ([Kenyon & Bromley 2008](#); [Krivov & Booth 2018](#)), planetesimals with low relative velocities form increasingly large bodies that in return dynamically excite smaller neighbours above the critical threshold for planetesimal destruction. The planetesimal growth scales with orbital period, resulting in an inside-out collisional cascade. Since a maximum growth speed is set by the host star and disc parameters, at any given time there is a maximum disc size that can be explained by self-stirring.

In the companion-stirring case ([Mustill & Wyatt 2009](#)), the planetesimals are excited by the companion's secular perturbations, and the maximum disc size at a given time is a function of the physical properties of both the central star and the companion. More details on the analytical models are given in Appendix A.2.

The optimal scenario to investigate these processes is therefore the one in which the disc and the companion(s) are observed and characterised at the same time, and DI is the perfect detection method. At the moment of writing, only a handful of such systems have been found: HR 8799 is one of the most extensively studied ([Marois et al. 2008](#), see also Figure 1.2), alongside HD 95086

(Rameau et al. 2013) and β Pic (Lagrange et al. 2010). In addition, only two systems are currently known where the companion is in the stellar mass regime: HR 2562 (Konopacky et al. 2016) and HD 206893 (Milli et al. 2017).

The limited number of systems suitable to investigate the companion-disc interaction does not allow us to fully comprehend this phenomenon, and therefore augmenting this sample is a primary goal. Moreover, observing and understanding the interaction between companion(s) and the disc they reside in could also help calibrate the flux-based planetary mass estimates from evolutionary models, since the dynamical interaction is a function of the companion mass.

In Chapter 2 we present the detection of a newly discovered low-mass stellar companion within the disc around the star HD 193571, which constitutes the perfect opportunity to test companion-disc interaction theories; and in Chapter 4 we carry out an homogeneous study of several DD-hosting stars combining direct imaging observations and companion-disc interaction models to constraint the presence of planetary and low-mass stellar companions.

1.3.2 $H\alpha$ emission from low-mass stellar companions

$H\alpha$ emission from low-mass stars and brown dwarfs can have multiple origins. In the case of young objects (<10 Myr) gas from the circumstellar disc can be accreted onto a circumsecondary disc and, due to the high temperatures of the shock front, this can lead to dissociation of H_2 molecules and consequent $H\alpha$ emission (Aoyama et al. 2018; Szulágyi & Mordasini 2017). In the case of young non-accreting stars, chromospheric activity produces well-known emission lines, with $H\alpha$ being one of the most prominent ones.

$H\alpha$ emission from single low-mass stars and brown dwarfs has been extensively studied through the years. West et al. (2004) used around 8000 single M dwarf spectra from the Sloan Digital Sky Survey (SDSS) to evaluate their $H\alpha$ flux and investigate the activity fraction and strength as a function of spectral type. They quantified the activity as logarithm of the ratio between the $H\alpha$ luminosity and bolometric luminosity, and they found a peak in the fraction of active stars around spectral type M8, where more than 70% of stars were active. They also evaluated the mean activity strength as the ratio between the $H\alpha$ luminosity and the bolometric luminosity, finding that it is constant between M0 and M5 and that it declines at later spectral types. Similar trends were recovered by subsequent surveys: Lee et al. (2009) studied the short-term $H\alpha$ variability of 43 single M dwarf, finding a similar decrease in the activity strength for later spectral types, as well as an increase in the variability level up to spectral type M7. Kruse et al. (2010) also focused on short-timescale $H\alpha$ variability using nearly 53000 spectra from SDSS; they recovered both the $\log(L_{H\alpha}/L_{bol})$ activity trend (that increases until \sim M6 with subsequent decrease) and the same variability trend (that increases with later spectral type). More recently, Robertson et al. (2013) studied the correlation between activity, mass, spectral type, and metallicity of 93 stars ranging

from K5 to M5. They find that the activity trend is recovered and, at a given stellar mass, metal rich stars appear to be more active.

However, much less is known about the $H\alpha$ emission from companions in binary systems, the main reason being the difficulty in disentangling the two components in the spectrum (with few exceptions, see e.g. [Bowler et al. 2014](#), [Santamaría-Miranda et al. 2018](#)). Few remarkable $H\alpha$ detections, often associated with accretion, have been made using high-contrast imaging techniques, which allow to differentiate between the two components in a binary system and evaluate the $H\alpha$ flux from the companion. One example is HD 142527 B, an accreting M-dwarf companion first detected in $H\alpha$ by [Close et al. \(2014\)](#) with the Magellan Adaptive Optics system (MagAO). The companion was later re-detected using the Zurich Imaging POLarimeter (ZIMPOL) of the SPHERE instrument at the Very Large Telescope (VLT) by [Cugno et al. \(2019\)](#), who also searched for local accretion signals in other objects suspected of hosting forming giant planets. More recently, [Wagner et al. \(2018\)](#) claimed the detection of $H\alpha$ emission from the young planet PDS 70 b. [Haffert et al. \(2019\)](#) were also able to detect $H\alpha$ emission from PDS 70 b with the MUSE Integral Field Spectrograph at the VLT ([Bacon et al. 2010](#)) and identified another accreting protoplanet in the same system, PDS 70 c. [Sallum et al. \(2015\)](#) claimed to have detected accretion from the companion orbiting around LkCa 15, but recent studies from [Thalmann et al. \(2016\)](#) and [Currie et al. \(2019\)](#) could not confirm it, also doubting whether the companions exist at all. Other remarkable $H\alpha$ detections include GQ Lup b and DH Tau b, both detected by [Zhou et al. \(2014\)](#) using the Hubble Space Telescope, and three newly detected brown dwarf companions from the Upper Sco region ([Petrus et al. 2020](#)).

These detections are fundamental for various reasons: firstly, they prove that it is feasible to detect planets and low-mass stellar companions using $H\alpha$ emission as a tracer; secondly, they give initial insight into the gas-accretion phase of planet and brown dwarf formation; and thirdly, they show that it is possible to use state of the art high-contrast imaging instruments and techniques to detect $H\alpha$ emission in binary systems.

In order to learn more about the early stages of planet formation and evolution, increasing the number of directly imaged known companions with $H\alpha$ detection is our primary goal. In this framework, in Chapter 3 we present ADI $H\alpha$ observations of the known companion around the star PZ Tel.

1.3.3 Direct imaging surveys

As already discussed in Section 1.2, the DI technique allows to probe a different (and complementary) space with respect to the RV, astrometry, and transit techniques, both in terms of type of targeted stars and in terms of detectable orbital configurations. DI is therefore an important tool to extend our knowledge of exoplanet population, but so far the number of directly detected

companions remains scarce (45 confirmed planets with mass $\leq 13 M_J$, at the time this Thesis is being written¹). Augmenting this sample is an important scientific goal, and several direct imaging surveys have contributed through the years, targeting different stars and aiming at slightly different scientific goals.

In the following I summarise some of the main surveys carried out in the last years, together with their main contributions and discoveries. This is by no means an exhaustive and comprehensive list, and additional information can be found in a number of different reviews, see e.g.: [Bowler \(2016\)](#) and [Perryman \(2018\)](#).

The International Deep Planet Survey (IDPS, [Vigan et al. 2012](#)) targeted a total of 292 stars between A and M spectral type, with a focus on massive stars. They collected data in H and K band for 14 years using various instruments and facilities: Keck II, the Gemini North and South, and the Very Large Telescope.

A series of surveys were carried out at the VLT using the NaCo instrument. Two of the largest ones are the VLT/NaCo large program to probe the occurrence of exoplanets and brown dwarfs at wide orbits (NaCo-LP, [Chauvin et al. 2015](#); [Desidera et al. 2015](#)) which targeted 86 stars of various spectral types in H and K band, and the NaCo Imaging Survey for Planets around Young stars (ISPY, [Launhardt et al. 2020](#), see also Section 1.3.3.1).

The SpHERE Infrared survey for Exoplanets (SHINE, [Chauvin et al. 2017](#)) is also carried out at the VLT, and makes use of the SPHERE instrument to target ~ 600 young and nearby stars. The survey led to important results, like the groundbreaking discovery of a newly formed planet around PDS 70, still embedded in its PPD ([Keppler et al. 2018](#)).

The SEEDS survey (Strategic Exploration of Exoplanets and Disks with Subaru) was carried out at the SUBARU telescope in both polarised differential imaging and angular differential imaging, targeting hundreds of disc-hosting stars ([Janson et al. 2013](#); [Tamura 2009](#)).

The Gemini NICI Planet-Finding Campaign ([Liu et al. 2010](#)) and the GPI Exoplanet Survey (GPIES, [Macintosh 2013](#); [Macintosh et al. 2014](#); [Nielsen et al. 2019](#)), are both large direct imaging exoplanet surveys carried out at the Gemini telescope, targeting hundreds of stars in total.

In the northern hemisphere, the Large Binocular Telescope (LBT) was used to carry out the LBT-LEECH survey ([Skemer et al. 2014](#); [Stone et al. 2018](#)), a 100 night imaging survey in the L' band observing 98 stars of various spectral types. The author of this Thesis is the main investigator of another imaging survey carried out at the LBT: the LISTEN survey, which is presented in Section 1.3.3.1 and detailed in Chapter 4.

As previously mentioned, the number of directly imaged companions is still low. This is likely a reflection of two factors: current instruments and post-processing algorithms must be improved

to lower the minimum mass of detectable planets and being able to probe regions closer to the host star, and the true occurrence rate of GP's on a wide orbit is naturally small. Given these low-number detections, many of the aforementioned direct imaging surveys emphasise the scientific significance of their non-detections (often in terms of achieved magnitude contrast at a given angular separation), which can be extremely valuable when trying to constraint the giant planet population occurrence rate.

However, these surveys use different instruments and data processing techniques, observe in different wavelengths, and target different stellar types, all of which make it very difficult to combine their results in a statistically significant way. [Bowler \(2016\)](#) attempted such an analysis, combining results from multiple survey ending up with 384 stars with spectral types between B2 and M6. The contrast curves for each target were assembled from the literature and used to derive sensitivity maps and planet occurrence rate in a coherent way. They obtain an occurrence rate estimate of $0.6^{+0.7}_{-0.5}\%$ planets with masses between 5 to $13 M_J$ and semi-major axis between 30 and 300 au, orbiting around single stars of age 5 to 300 Myr and mass between 0.1 and $3.0 M_\odot$. As a function of spectral type, the occurrence rates are $2.8^{+3.7}_{-2.3}\%$ for BA stars, and have 95% confidence upper limits of $< 4.1\%$ for FGK stars and $< 3.9\%$ for M stars. The overall occurrence rate is in agreement with what was found by [Galicher et al. \(2016\)](#), which combined results from the IDPS, the Gemini deep planet survey ([Lafrenière et al. 2007](#)) and the NaCo Survey of Young Nearby Austral Stars ([Chauvin et al. 2010](#)) to obtain an occurrence rate of $1.05^{+2.80}_{-0.70}\%$ planets with masses between 0.5 and $14 M_J$, between 20 and 300 au, based on a sample of 356 stars. More recently, [Vigan et al. \(2017\)](#) combined the results from the NaCo-LP survey with 12 other imaging surveys to obtain a coherent sample of 100 FGK stars. They estimated a sub-stellar companion frequency of 0.75 – 5.70% for objects of mass between 0.5 and $75 M_J$ within 20 to 300 au from their host star.

While all of these occurrence rate estimates agree with each other, they are still highly uncertain and rely on many assumptions, like the underlying planet formation and evolution theories, planet-disc interactions, and planet migration, among others. Trying to understand these various aspects is an important goal, and well-tailored surveys with a coherent target sample and investigating specific scientific goals are useful to this end. In the following I detail two additional direct imaging surveys which have been designed to tackle the specifics of companion-disc interactions with the direct imaging technique.

1.3.3.1 The NaCo-ISPY and the LStEN survey

The NaCo-ISPY ([Launhardt et al. 2020](#)) is a direct imaging survey currently being carried out using the NaCo instrument at the VLT telescope, in Chile. The survey targets ~ 200 young and nearby stars with known and well-characterised circumstellar discs, of which ~ 50 are PPD's and

~150 are more evolved DD's. The main scientific goals of the ISPY survey are: *a)* increasing the number of directly imaged GP's on wide (≥ 5 au) orbits, *b)* testing the capability of detecting GP's in the early phases of planet formation, while they are still embedded in their PPD's, and *c)* investigating the relation between the DD's properties and the presence of a wide-separation GP.

The survey started in December 2015 and all the observations are carried out in the L' filter in pupil-tracking ADI mode. Each target is typically observed for 2 to 4 hours around its meridian passage, so to maximise the achieved field rotation. The data is homogeneously reduced with a version of the GRAPHIC pipeline (Hagelberg et al. 2016) optimised for the ISPY observation strategy. The last follow-up observations are expected to be carried out shortly, and a statistical analysis of the whole survey will be presented in an upcoming paper. The presentation of the survey and the results from the first 2.5 years of observations are presented in Launhardt et al. 2020, and one of its discoveries include the detection of a low-mass stellar companion around the DD-hosting star HD 193571, which is presented in Musso Barucci et al. 2019b and discussed in Chapter 2.

The L' band Imaging Survey to find Exoplanets in the North (LISStEN, of which the author of this Thesis is the primary investigator), has been designed to be the ISPY extension in the northern hemisphere. The survey focuses on nearby, young stars with known circumstellar discs, and observations were carried out between Autumn 2017 and Spring 2019 using the LMIRCam at the LBT, in Arizona, for a total of 29 observed targets. The survey data selection, observations, scientific goals, data reduction and results are presented in Chapter 4 of this Thesis, and will be published in an upcoming paper (Musso Barucci in prep.).

1.4 Thesis outlook and scope

This Thesis focuses on the direct imaging technique, and on the planet formation and evolution questions that it can help to tackle, namely: the intricacies of companion-disc interactions, both for single objects and in a broader survey context, as well as the capability of detecting companions using $H\alpha$ as a tracer.

In Chapter 2 I present the discovery of a low-mass stellar companion around the debris disc hosting star HD 193571, which was observed as part of the NaCo-ISPY survey. In Chapter 3 I discuss the $H\alpha$ emission detected from the known M dwarf companion to PZ Tel, which was observed using the SPHERE/ZIMPOL instrument at the VLT. In Chapter 4 I present the LISStEN survey, detailing its data selection, observations and data reduction, as well as its main preliminary results in terms of companion-disc interaction analysis and achieved magnitude contrast. Finally, in Chapter 5 I summarise the main results of this Thesis and discuss the possible future steps.

2

ISPY - NaCo Imaging Survey for Planets around Young stars Discovery of an M dwarf in the gap between HD 193571 and its debris ring

*This chapter was published as a refereed article ([Musso Barcucci et al. 2019b](#)) in *Astronomy & Astrophysics*, for which I am the lead author and which has been adapted for this Thesis.*

2.1 Introduction

Detecting and characterising giant planets around debris disc hosting stars is one of the scientific goals of the ISPY survey ([Launhardt et al. 2020](#)). The survey makes use of the NaCo instrument ([Lenzen et al. 2003](#); [Rousset et al. 2003](#)) at the VLT to observe ~ 200 targets in the L' band, and observations are carried out in angular differential imaging mode ([Marois et al. 2006](#)).

In this Chapter we present the detection of a newly discovered low-mass stellar companion around the star HD 193571, which was observed as part of the ISPY survey. In Section 2.2 we give information about the target star and its surrounding debris disc; in Section 2.3 we detail the observations and the data reduction; in Section 2.4 we analyse the data to obtain constraints on the astrometry and photometry of the companion, as well as on its orbital motion; in Section 2.5 we study the interaction between the companion and the disc in terms of stirring mechanisms, and we finally summarise the results in Section 2.6.

Table 2.1: Fundamental stellar parameters and properties for HD 193571.

Parameter	Value	Ref.
RA [hh:mm:ss]	20:22:27.50	e
DEC [dd:mm:ss]	-42:02:58.43	e
Parallax [mas]	14.61 ± 0.17	a
Distance [pc]	68.45 ± 0.82	a
Proper motion [mas/yr]	$\mu_\alpha \times \cos\delta = 41.31 \pm 0.22$	a
	$\mu_\delta = -83.74 \pm 0.19$	a
Sp. Type	A0V	f
T_{eff} [K]	9740 ± 100	c
Mass [M_\odot]	2.2 ± 0.1	b
Radius [R_\odot]	1.85 ± 0.1	c
$v \sin i$ [km/s]	71	b
L [L_\odot]	27.7 ± 1	c
$f = L_{\text{disc}}/L_\star$	$2.3 \times 10^{-5} \pm 1 \times 10^{-6}$	c
Bayesian Age [Myr]	161^{+247}_{-35}	b
Interp. Age [Myr]	66	b
m_L [mag]	5.614 ± 0.030	d
m_H [mag]	5.609 ± 0.030	d

References. ^(a) Gaia Collaboration et al. (2018, 2016). ^(b) David & Hillenbrand (2015). ^(c) This work (see Section 2.2). ^(d) Apparent magnitude of the host star in the L' band, derived from SED fitting (see Section 2.2) and correcting for the NaCo L' band transmission curve. ^(e) Value taken from the online Simbad catalogue. ^(f) Chen et al. (2014).

2.2 HD 193571

Within the NaCo-ISPY survey, we observed HD 193571 (HR 7779, GJ 969, κ 01 Sgr), an A0V field star at a distance of 68.45 pc (Gaia Collaboration et al. 2018), which is part of a wide-separation ($>40''$) three-component system¹ (WDS Catalogue, see Mason et al. 2014).

The age of this target is uncertain: David & Hillenbrand (2015) derived stellar parameters for more than 3000 nearby early-type (BAF) field stars, and compared them with stellar isochrones. They computed final ages and masses with both a Bayesian inference approach and classical isochrone interpolation, obtaining 161 Myr and 66 Myr, respectively. They presented criteria to decide between the two values, but for HD 193571 it is unclear which age or mass estimate should be preferred. Throughout this study we use a primary mass of $M = 2.2 \pm 0.1 M_\odot$, which encompasses both the Bayesian inferred mass and the mass derived via interpolation. The age estimates for HD 193571 are presented in Table 2.1, together with the main stellar properties.

HD 193571 is known to harbour a debris disc, inferred from its infrared excess ($f = 2.3 \times 10^{-5}$). We fit its SED to derive the stellar luminosity and effective temperature, and the debris belt radius. We fit simultaneously a stellar atmosphere (PHOENIX; Husser et al. 2013) plus a

¹The B and C components were observed in 2000 and 1999, and have a distance of $39.30''$ and $56.80''$, with a P.A. of 312° and 283° , respectively.

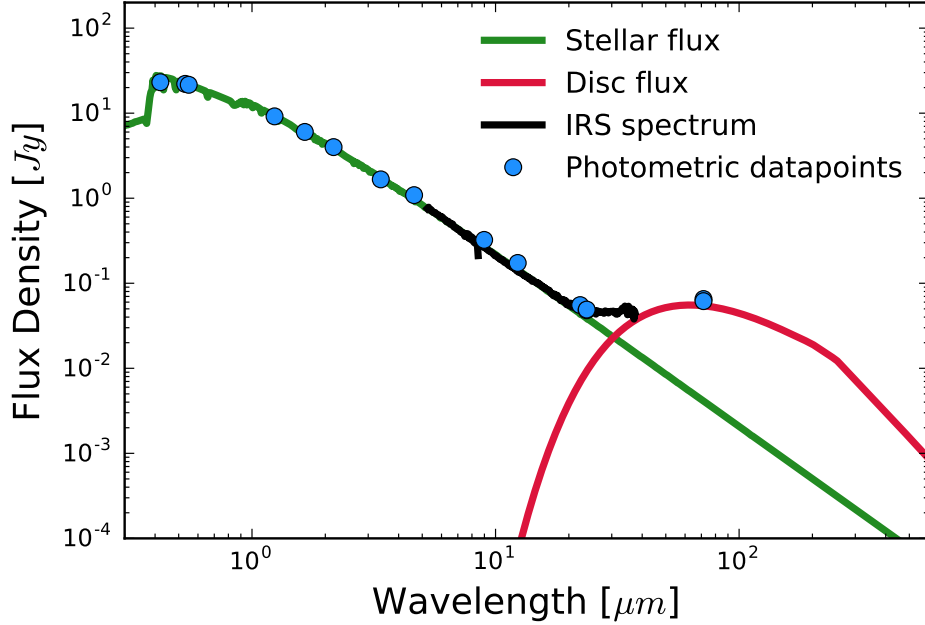


Figure 2.1: Flux density distribution of HD 193571, showing the photometric datapoints found in the literature (in blue) and the IRS spectrum (in black), together with the fitted stellar (green) and disc (red) fluxes.

single black-body (BB) model to the observed photometry and the Spitzer IRS spectrum. The photometry includes a wide range of filters and wavelengths, from: "Heritage" Stromgren and UVB (Paunzen 2015), 2MASS (Skrutskie et al. 2006), Hipparcos/Tycho-2 (Esa 1997), AKARI (Ishihara et al. 2010), WISE (Wright et al. 2010), and Spitzer (Chen et al. 2014). The fitting method uses synthetic photometry of grids of models, and finds the best-fitting model with the MultiNest code (Feroz et al. 2009). The SED of HD 193571 is best fit by an A0 stellar model plus a one-temperature BB model locating the dust at a distance of $R_{\text{BB}} = 62 \pm 4$ au, with a temperature of 81 ± 3 K. The best fit is shown in Figure 2.1. The BB radius of the dust disc is given by (Pawellek & Krivov 2015):

$$R_{\text{BB}} = \left(\frac{278 \text{ K}}{T_{\text{dust}}} \right)^2 \left(\frac{L}{L_{\odot}} \right)^{1/2}$$

An estimate of the 'true' disc radius, R_{disc} , is then obtained by applying a stellar luminosity-dependent correction factor, Γ , which accounts for the radiation pressure blowout grain size (Pawellek & Krivov 2015):

$$\Gamma = a (L_*/L_{\odot})^b$$

using the new coefficients given in Pawellek (2016): $a = 7.0$ and $b = -0.39$. After applying this correction, the estimated disc size for HD 193571 is 120 ± 15 au. The disc has never been imaged

in scattered light, and additional SPHERE/IRDIS observations were inconclusive in this respect (see Appendix A.1).

We used the fitted stellar spectrum to derive the stellar H and L' magnitudes (reported in Table 2.1), integrating over the NaCo H - and L' -band filters. We used zero points of 1.139×10^{-10} erg/cm²/s/Å and 5.151×10^{-12} erg/cm²/s/Å, respectively².

2.3 Observations and data reduction

HD 193571 was observed at two different epochs with NaCo at the Very Large Telescope, and an additional third epoch was obtained with the Gemini Planet Imager (GPI, [Macintosh et al. 2014](#)) through the Fast Turnaround observing mode (Program ID: GS-2018A-FT-111).

2.3.1 VLT/NaCo

Coronagraphic ADI observations of HD 193571 were obtained in May 2016 and June 2018 in L' band (see Table 2.2), making use of the Annular Groove Phase Mask (AGPM, [Mawet et al. 2013](#)) vector vortex coronagraph to suppress as much as possible the diffraction pattern from the host star. We used cube-mode, saving 100 frames per cube. The observations were interlaced with frequent sky observations for background subtraction (every ~ 8 minutes) and bracketed with non-coronagraphic flux measurements to create an unsaturated PSF reference. The data was reduced with the ISPY end-to-end modular reduction pipeline GRAPHIC ([Hagelberg et al. 2016](#)). The main reduction steps comprise background subtraction, flat field correction, bad pixel cleaning, and centring. Each cosmetically reduced cube is then median combined. For a more detailed explanation on how the data reduction is performed we refer to the ISPY overview paper ([Launhardt et al. 2020](#)). The observations are summarised in Table 2.2.

2.3.2 Gemini/GPI

HD 193571 was observed in the H band with GPI in coronagraphic ADI mode on the 12th of August 2018, obtaining 76 frames and achieving a total field rotation of 88 degrees. The integration time for each exposure was 60 seconds.

The photometry of GPI data can be calibrated using the satellite spots, which are four reference spots created by diffraction of the central star light from a square grid superimposed on the pupil plane ([Wang et al. 2014](#)). They can be used to extract the photometry and spectroscopy of the

²<http://svo2.cab.inta-csic.es/svo/theory/fps3/index.php?mode=browse&name=Paranal&gname2=NACO>

Table 2.2: VLT/NaCo summary of observations

Parameter	Epoch 1	Epoch 2
Obs.	30/05/2016	21/06/2018
Prog. ID	097.C-0206	1101.C-0092
#cubes	91	196
Tot. P.A.	78°	84°
DIT Obs. ^a [s]	0.35	0.35
DIT Flux ^b [s]	0.07	0.07
DIMM ^c	~1'0	~1'1
Tot. time ^d [m]	53	114
Sky time ^e [m]	4.1	9.3

References. ^(a) Detector Integration Time for the observations, chosen to avoid saturation outside $\sim 0''.1$. ^(b) Detector Integration Time for the non-coronagraphic flux measurements. ^(c) Mean DIMM seeing during the observations. ^(d) Total on-source integration time, in minutes. ^(e) Total on-sky time, in minutes: 7 sky visits for the 2016 dataset and 16 sky visits for the 2018 dataset.

central star. During the observations there was a misalignment of the grid that produces the satellite spots, resulting in a diffraction spike above two of the four satellite spots, thus rendering them unusable for photometric calibration. Therefore, in the following analysis when referring to the satellite spots we only refer to the two unbiased ones.

The data were reduced making use of the publicly available GPI Data Pipeline (Maire et al. 2010), with the following reduction steps:

- Calibration files were created using the ‘Dark’ and ‘Wavelength Solution 2D’ recipes, applied to the dark frame and the Argon lamp calibration snapshot taken as part of the observations.
- A bad pixel map was created combining the results of the ‘Hot Bad Pixel Map’ and ‘Cold Bad Pixel Map’ recipes, which have been applied respectively to a set of 15 dark frames and a set of 5 daytime Wollaston disperser flat frames for each filter (Y, J, H, K1, and K2). The calibration files were chosen from the Gemini Data Archive to be the closest in time to the observations.
- The data were reduced applying the ‘Calibrated Datacube Extraction’ recipe, using the above-mentioned newly created calibration files. This recipe also includes an automatic search and characterisation of the four satellite spots, storing in the header the location and peak flux (in ADU) of all the spots, for each wavelength channel.
- The flux-calibrated cubes were oriented using the internal GPI recipe ‘Rotate North Up’.

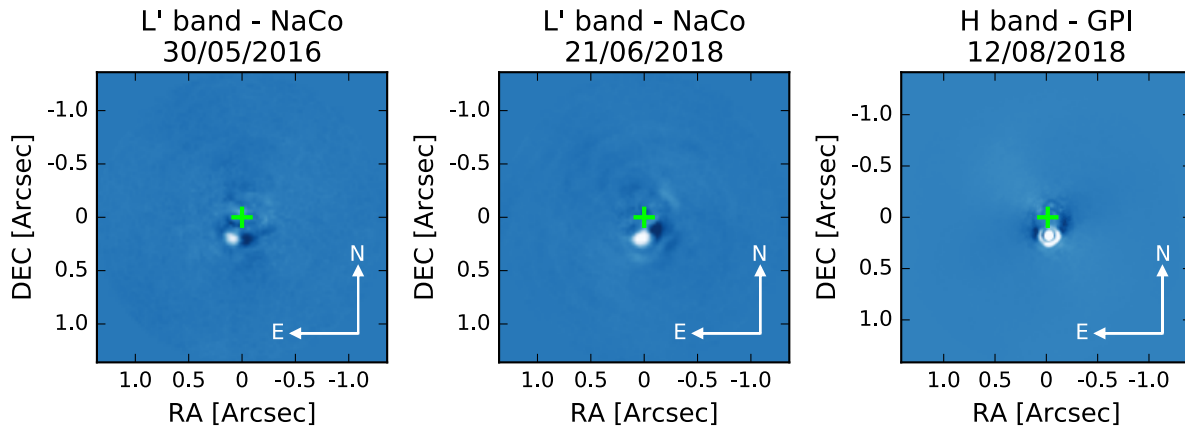


Figure 2.2: Classically ADI reduced images for the two NaCo datasets (left and centre) and for the GPI dataset (right). The images are oriented with North up and East left, and the green cross indicates the position of the central star. The companion is clearly visible close to the centre in all three datasets. The images are normalised and the colour map was chosen for a better visualisation of the data.

2.4 Analysis and results

The final classically ADI reduced images for all the three epochs are shown in Figure 2.2. A close-in companion is clearly visible in all three epochs south of the star.

2.4.1 Astrometry and photometry

To analyse the two NaCo datasets we used the *ANDROMEDA* (Cantalloube et al. 2015)³ package, which uses a maximum likelihood estimation approach together with negative fake signal injection to evaluate the astrometry and photometry of a companion in an ADI dataset. The algorithm needs as inputs the reduced frames (corrected for the AGPM throughput), the parallactic angles, and an unsaturated and exposure time-scaled image of the central star. Since we were interested in analysing only the known companion, we set the inner working angle and outer working angle keywords to $0.2 \lambda/D$ and $20 \lambda/D$, respectively (we refer to Cantalloube et al. 2015 for a detailed explanation of the *ANDROMEDA* package). The final x and y offsets (and relative 3σ uncertainties) were converted into separation and position angle using a platescale for NaCo of 27.2 mas/pix , assuming a conservative error of 0.5 pixels on the centring of the frames, and correcting for the true North offset of $0^\circ 486 \pm 0^\circ 180$ (Launhardt et al. 2020). Given the target’s distance and L' band magnitude (see Table 2.1), we converted the flux evaluated with *ANDROMEDA*, and relative 3σ uncertainties, into an absolute L' magnitude for both epochs accounting for the uncertainties on the host star magnitude and distance from the system. The

³<http://www.theses.fr/2016GREAY017>

Table 2.3: Astrometry and photometry of the companion candidate for all three datasets

Date of obs.	FPF 5σ	Separation [arcsec]	P.A. [deg]	Projected semi-major axis [au]	Abs. Mag. [mag]
30/05/2016	4.4×10^{-4}	0.180 ± 0.014	152.35 ± 4.46	12.30 ± 0.97	$M_L = 6.12 \pm 0.14$
21/06/2018	3.6×10^{-5}	0.167 ± 0.014	170.27 ± 4.81	11.42 ± 0.97	$M_L = 6.28 \pm 0.11$
12/08/2018	1.00×10^{-13}	0.155 ± 0.012	176.90 ± 3.71	10.60 ± 0.83	$M_H = 6.89 \pm 0.06$

Given the small angular separation of the companion, the false probability fraction (FPF) values were evaluated on the classically ADI reduced images following the prescription in Mawet et al. (2014), which accounts for small sample statistics. The final magnitudes are absolute values calculated taking into account the distance to the target and its uncertainties.

final astrometry and photometry values for the two NaCo epochs, as well as the GPI epoch, are given in Table 2.3.

For the GPI dataset we evaluated astrometry and photometry of the companion in a slightly different way since no unsaturated exposure of the central star was obtained. For the astrometry, we made use of the satellite spots (visible in all the reduced frames) to create a PSF reference: we first averaged the two satellite spots in each frame, and then we averaged over the 76 frames, obtaining a PSF for each spectral channel. We use this PSF, together with the *ANDROMEDA* package, to obtain the astrometry of the companion (as was done for the NaCo datasets) in each spectral cube. The final astrometry is the weighted mean of the astrometric positions at each wavelength, and is given in Table 2.3 taking into account the GPI pixel scale of 14.166 mas/pix, the additional true North offset of $0.10 \pm 0.13^\circ$ as reported in Rosa et al. 2015, and a conservative error on the centring of 0.5 pixels.

To obtain the photometry of the companion we calibrated the cubes extracted in Section 2.3.2 in the following way:

- For each spectral channel, we averaged the satellite spots peak flux (stored in the header), obtaining a mean satellite flux in ADU, and relative standard deviation;
- We then converted the frame from ADU to physical units, using the following equation (as detailed on the GPI website⁴):

$$\text{frame}[\text{units}] = \frac{\text{frame}[\text{ADU}]}{\text{Satellite spectrum}[\text{ADU}]} \times \frac{\text{Star Spectrum}[\text{units}]}{\text{Star-to-Satellite Flux ratio}}$$

The ‘Star-to-Satellite Flux ratio’ was calibrated by the GPI team⁵, and it is $= (2 \times 10^{-4})^{-1}$. The ‘Star Spectrum’ (in the desired flux units) is obtained from the stellar spectrum fitted in Section 2.2. We accounted for the uncertainty on the ‘Star-to-Satellite Flux ratio’, the uncertainties on the stellar spectrum, and the standard deviation of the satellite spots flux.

⁴http://docs.planetimager.org/pipeline/usage/tutorial_spectrophotometry.html

⁵See footnote 4.

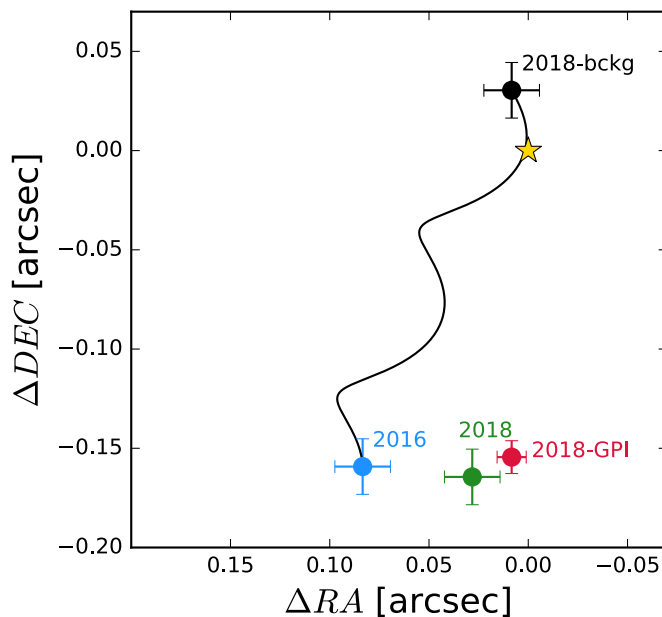


Figure 2.3: Proper motion analysis of the companion showing the astrometry for the three epochs. The black data point is the position that the companion would have at the epoch of the GPI observation if it were a background star with no motion, using its position in 2016 as starting point and considering the proper motion of the host star. The companion is clearly co-moving with the star (shown in yellow).

- To account for possible contamination from the stellar halo, we median combined all the frames in each spectral channel, and then subtracted this median from each photometrically calibrated cube.
- We then extracted a spectrum for the companion from each median-subtracted, photometrically calibrated cube, fitting a Gaussian to the companion to get the peak flux. The final spectrum is the weighted average of the spectra in all cubes.

The final spectrum of the companion is shown in Figure 2.4. We integrated this spectrum over the NaCo H-band filter, obtaining a NaCo H-band apparent magnitude of 11.07 ± 0.06 . This corresponds to an absolute magnitude of 6.89 ± 0.06 . The final astrometry and photometry for the companion is given in Table 2.3.

The close separation makes it unlikely for the companion to be a background star. Nevertheless, we evaluated the position that the object would have on the sky at epoch 2018, starting from its position in epoch 2016, if it were a background object with no significant proper motion. The results are shown in Figure 2.3. The object is clearly co-moving with the host star, at a projected separation of ~ 11 au.

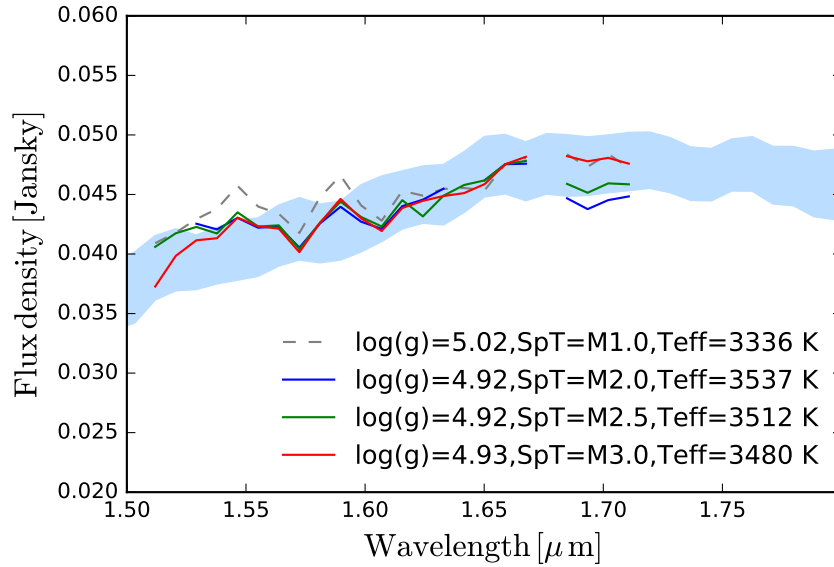


Figure 2.4: Comparison between the spectrum of the companion and observed spectra of early M dwarfs. The blue shaded area is the flux density of the companion in the GPI H-band, in Jansky. The spectrum is the weighted average of the spectra extracted from the 76 GPI datacubes and the area encompass the uncertainties (derived from the uncertainty on the flux of the host star). The solid lines are three spectra from the CARMENES stellar spectral library, for various T_{eff} and $\log g$ values (evaluated in Hintz et al. 2019) and the dotted grey line is an additional spectrum of an M1 object.

2.4.2 Physical properties

We compared the GPI H-band spectrum with observed spectra of early M dwarfs from the stellar spectral library⁶ of the CARMENES survey (Reiners et al. 2018), which is the first large library of M dwarfs with high-resolution spectra in the infrared. We plot three of the best matching spectra (binned to the GPI H-band resolution) in Figure 2.4, a non-matching spectrum (dotted grey line) for comparison, and the H-band spectrum of HD 193571 B. From the comparison, we can infer a surface gravity of $\log g \sim 4.9$, a temperature of ~ 3500 K, and a spectral type between M3 and M2, which seem to fit the data reasonably well. However, a high-resolution and/or broader band spectrum would be needed to properly constrain the surface gravity and spectral type of the companion.

We estimated the mass of the companion using the BT-Settl evolutionary tracks (Allard et al. 2012)⁷, by comparing them with the observed L' - and H -band photometry. In the colour-magnitude diagram of Figure 2.5 we show the companion L' -band absolute photometry of 6.19 ± 0.08 mag (evaluated as the weighted mean of the two NaCo epochs), as well as evolutionary tracks for two representative ages of 60 Myr (dashed line) and 150 Myr (solid line). As shown in Figure 2.5, the

⁶<http://carmenes.cab.inta-csic.es/gto/jsp/reinersetal2018.jsp>

⁷<http://svo2.cab.inta-csic.es/theory/newov/>

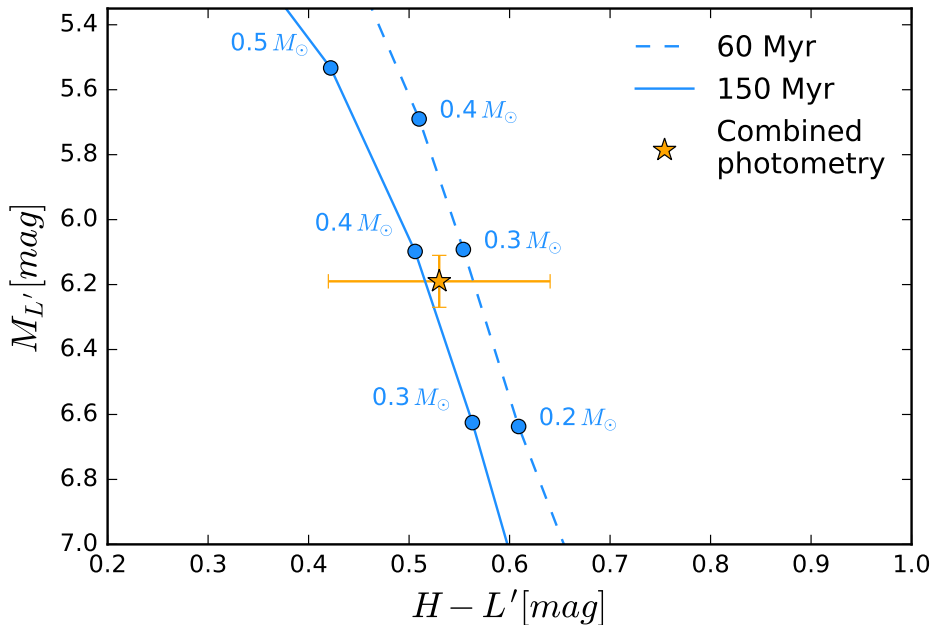


Figure 2.5: Colour-magnitude diagram showing the weighted mean L' -band magnitude derived from the 2016 and 2018 NaCo datasets, together with the H -band magnitude derived from the GPI dataset. We plot the evolutionary tracks for the BT-Settl models from Allard et al. (2012), for ages of 60 and 150 Myr. The photometry does not allow us to distinguish between the two age estimates.

photometry does not allow us to distinguish between the two age estimates, so we use both age values in the rest of the analysis. We interpolated the BT-Settl models to estimate the mass of the companion for both L' - and H -band photometry, in mass steps of 0.034 dex. Taking into account the photometric uncertainty in both bands, we obtained a weighted mass of $0.395 \pm 0.007 M_{\odot}$ for an age of 161 Myr, and $0.305 \pm 0.025 M_{\odot}$ for an age of 66 Myr.

2.4.3 Orbital motion

The astrometry of the companion between the three epochs shows signs of orbital motion. Following the prescription in Pearce et al. (2015), we can explore the possible orbital solutions for a companion imaged over a short orbital arc, using the dimensionless parameter B ($\sqrt{B} = V_{\text{sky}}/V_{\text{esc}}$ is the sky-plane velocity of the companion divided by the escape velocity), and the direction of motion φ , where $\varphi = 0^{\circ}$ is motion along a vector from the primary to the companion.

We assumed a total system mass of $2.6 \pm 0.1 M_{\odot}$ (for an age of 161 Myr) and $2.55 \pm 0.1 M_{\odot}$ (for an age of 66 Myr) and we derived⁸ B and φ for the three epochs (NaCo 2016, NaCo 2018, and GPI 2018). For both age estimates the values agree within the uncertainties, and we obtain

⁸<http://drgmk.com/iorbel/>

$B = 0.25^{+0.16}_{-0.11}$ and $\varphi = 100 \pm 15^\circ$, which leads to a minimum semi-major axis of $a_{\min} = 8.20 \pm 1.77$ au (see eq. (5) in Pearce et al. 2015). Following Pearce et al. (2015), we can draw the following conclusions:

- Even considering the uncertainties, the B value is < 1 , so the companion’s sky-plane motion is below the escape velocity. While the object could be unbound if the line of sight velocity (or separation) is high, this is unlikely.
- We cannot place constraints on the eccentricity of the orbit, meaning that a circular orbit cannot be ruled out (this will have an impact on our stirring mechanisms study in Section 2.4).
- We can place a loose upper limit of $\sim 80^\circ$ on the inclination.

We also explored the possible orbital motion parameters using the python package *orbitize*⁹ with the Orbit For The Impatient (OFTI) algorithm detailed in Blunt et al. (2017) (see Appendix A.3). While the uncertainties on the astrometry and the limited amount of datapoints do not place any meaningful constraints on the orbital elements, the periastron distance is restricted to $\lesssim 15$ au. This result is confirmed by exploring the possible orbital parameters using the method of Pearce et al. (2015). Therefore, if the companion’s orbit is nearly coplanar with the disc, the entire orbit should be interior to the disc, otherwise the companion would have disrupted the disc on a dynamical timescale. Assuming a circular orbit and a semi-major axis of 11 au, the companion would have a minimum period of ~ 23 years, implying that a baseline of several years would be needed before any additional astrometric datapoint could provide better constraints on the orbital elements. The companion is massive enough that even in the unlucky case of an almost face-on orbit ($i \sim 1^\circ$) it would produce a radial velocity signal strong enough to be detected (semi-amplitude $K \gtrsim 120$ m/s); however, this would also require a time baseline of many years.

2.5 Stirring mechanisms

The relative importance of self- and companion-stirring mechanisms is a non-trivial problem. It depends on the companion’s physical and orbital parameters, the host star age and mass, and the disc mass in solids. The equations used in this section are from Wyatt (2008) and Mustill & Wyatt (2009), and are summarised in Appendix A.2. We note that to be consistent with the underlying assumptions of these two papers, we use the black-body disc radius of 62 au while working with equations from Wyatt (2008), and the corrected disc radius of 120 au for the Mustill & Wyatt (2009) equations (see Appendix A.2). That is, the model in Wyatt (2008) uses

⁹<https://orbitize.readthedocs.io/en/latest/>

parameters derived by fitting to black-body radii, while the model of [Mustill & Wyatt \(2009\)](#) uses orbital dynamics, so is based on physical disc radii.

Assuming that the mutual inclination between the plane of the orbit and the disc is not too large, there are two conditions that need to be satisfied for a companion to dominate the stirring process at a certain distance from the star, and at a given time: *a*) the companion must be able to stir planetesimals, at that location, to relative destructive velocities and *b*) the timescale for companion-stirring at that distance must be greater than the self-stirring timescale.

The first condition is encapsulated by Eqs A.2 and A.3 in Appendix A.2, which give the maximum distance at which a companion with a given semi-major axis a_{pl} and eccentricity e_{pl} can stir planetesimals above the disruption threshold velocity v_{rel} . This velocity is a function of the planetesimal size R and, as shown by Eq. A.2, has a minimum at $R \sim 80$ m. We set this maximum distance equal to the estimated true disc radius of 120 au, and we plotted the $a_{\text{pl}}-e_{\text{pl}}$ relationship in Figure 2.6 for the $R = 80$ m case (solid light blue curve). The companion would not be able to stir planetesimals at that distance if its semi-major axis and eccentricity were below this curve. The planetesimals might be smaller or larger than 80 m, and this would increase v_{rel} and push the light blue curve rightwards and upwards. While R has a definite minimum (particles smaller than a certain size, typically around few μm , would be blown away by radiation pressure from the central star) it is not straightforward to define a maximum R value. We proceeded as follows:

- At any given time, there is a maximum size of planetesimals that participate in the collisional cascade (because larger objects will have collision timescales longer than the stellar age). This maximum size R_{max} can be evaluated by inverting Eq. A.1. For a disc size of 62 au, and with a fractional luminosity of the disc f , stellar mass and stellar luminosity as in Table 2.1, we have $R_{\text{max}} = 132$ m. This is the maximum value for R , assuming that the disc has been stirred for all of its life ($t_{\text{stir}} = t_{\text{age}} = 66$ Myr. In the 161 Myr case we obtain $R_{\text{max}} = 790$ m).
- An internal perturber can influence the timescale of orbit crossings for planetesimals, and thus t_{stir} might be less than the stellar age (i.e. the disc was stirred more recently). We use Eq. A.4 to calculate this orbit crossing timescale t_{cross} as a function of the perturber properties (eccentricity, semi-major axis, and mass).
- We now have a revised value for the total time the disc has been stirred as $t_{\text{stir}} = t_{\text{age}} - t_{\text{cross}}$, and consequently a revised R_{max} value as a function of the perturber properties (i.e. we have a relationship between R_{max} , a_{pl} , and e_{pl}).
- Combining this relationship with Eqs. A.2 and A.3, we can trace R_{max} in the $(a_{\text{pl}}, e_{\text{pl}})$ parameter space.

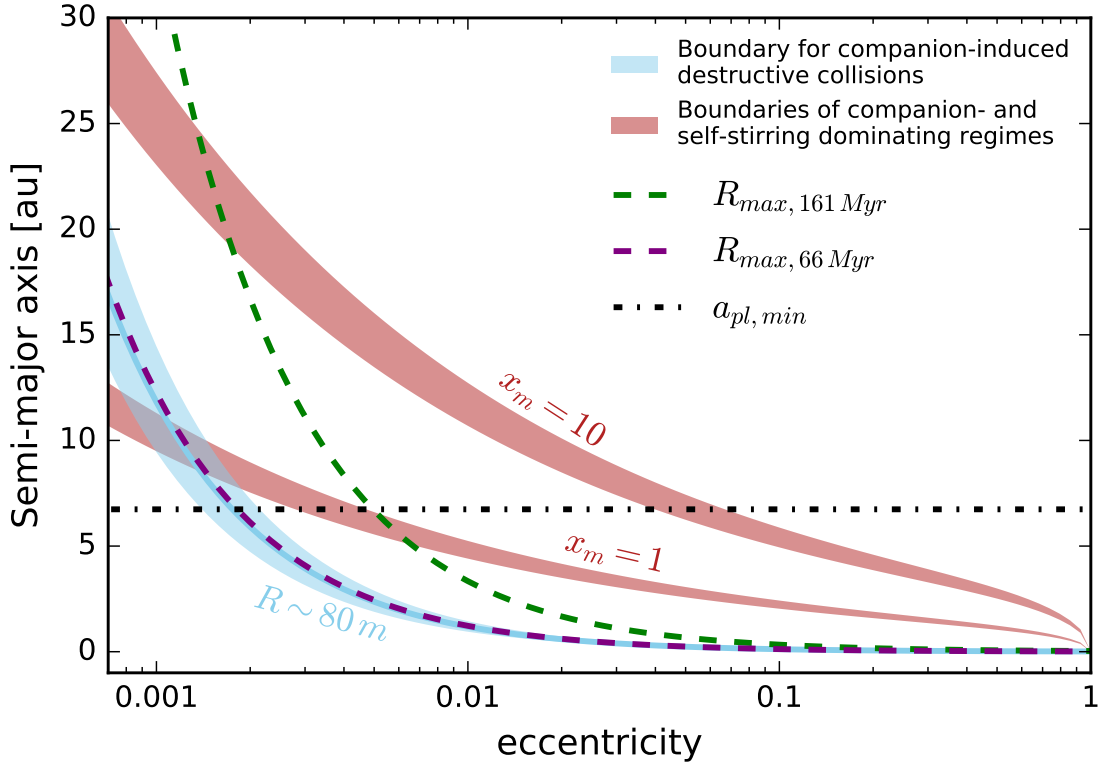


Figure 2.6: Boundaries between a self-stirring and companion-stirring dominated disc. The light blue lines mark the (a_{pl}, e_{pl}) parameter space in which the companion would be able to stir planetesimals of size R to destruction velocities at a distance of 120 au. The shaded area around the solid light blue ($R = 80$ m) line takes into account the errors on the disc size and the stellar mass. The dashed purple line shows the R_{max} for 66 Myr (close to the solid light blue line) and the dashed green line shows the R_{max} value for the 161 Myr case. The shaded red areas indicate the boundaries between the self-stirring and companion-stirring dominated cases, for a fixed distance and companion mass, and for two representative x_m values; accounting for errors on disc size, stellar mass, and companion mass (the areas encompass both age estimates). The horizontal dotted black line is the lowermost boundary of the minimum possible companion semi-major axis calculated in Section 2.4.3. The companion dominates the stirring process only for combinations of a_{pl} and e_{pl} lying above the light blue curve (the companion can stir planetesimals at the disc distance) and the red curve (the companion stirs the disc faster than the disc stirs itself).

As can be seen in Figure 2.6, when we plot this for the 66 Myr case, R_{max} is relatively small (~ 132 m along the curve) and almost overlaps with the $R = 80$ m case. The R_{max} in the 161 Myr case is plotted with a dashed grey curve. The companion can stir the disc over most of the shown parameter space.

The second condition requires that, at a given time and distance, the companion-stirring timescale is shorter than the self-stirring timescale. [Mustill & Wyatt \(2009\)](#) made such a study and defined the parameter Φ as the distance at which self and companion-stirring times are equal (see Appendix A.2). It is a function of the companion's properties (mass m_{pl} , semi-major axis a_{pl} ,

and eccentricity e_{pl}), the central star’s mass, and the disc’s mass in solids (expressed by the dimensionless parameter x_{m} , see Appendix A.2). Since we are interested in which stirring process is dominant at the location of the debris belt, we set $\Phi = 120$ au and obtain the equilibrium relationship between self- and planetary-stirring. Tracing this line in the $(a_{\text{pl}}, e_{\text{pl}})$ parameter space marks the boundary between the domination of the two stirring processes, thus allowing us to investigate the combination of a_{pl} and e_{pl} for which the disc is dominated by self-stirring. Since there is a dependence on the x_{m} value as well, in In Figure 2.6 we plotted two representative values for x_{m} of 1 and 10 (solid red lines). The curve for $x_{\text{m}} = 10$ lies above the $x_{\text{m}} = 1$ case because a more massive disc forms large planetesimals more quickly, and can thus self-stir earlier. As discussed in [Mustill & Wyatt \(2009\)](#), $x_{\text{m}} \gtrsim 10$ discs may be problematic as their high masses imply gravitationally unstable discs at earlier times when the gas was present. Thus, it is likely that the $x_{\text{m}} = 10$ line in Figure 2.6 represents an upper limit to where the disc could be self-stirred. Given an x_{m} value and fixing the companion mass to $0.25 M_{\odot}$, any combination of eccentricity and semi-major axis above the curve would imply that companion-stirring is quicker than self-stirring at the distance of the disc, hence the companion-stirring would dominate the stirring process. An additional constraint can be placed on the minimum semi-major axis, as discussed in Section 2.4.3, which is shown by the dashed black line in Figure 2.6.

It is important to note that both conditions must be satisfied for the companion to dominate the stirring process, and this is true only for certain combinations of eccentricity and semi-major axis. In the plot it is clear how, given an eccentricity $\gtrsim 0.1$, any semi-major axis places the companion above both curves, and thus the companion would dominate. For eccentricities $\gtrsim 0.002$, any a_{pl} would lie above the light blue curves (both for the $R \sim 80$ m and for the R_{max} case), but only certain a_{pl} would satisfy the criterion for companion-induced stirring dominating over self-stirring (depending on the x_{m} value), so low-eccentricity companions must be closer to the disc to dominate the stirring. Finally, for extremely low eccentricities ($\lesssim 0.002$) and small semi-major axes, the companion would not be able to stir planetesimals at the distance of the disc (below the light blue curve), and in any case the self-stirring would be dominant at that distance (below the red curve).

As shown in Figure 2.6, it is most likely that the companion is dominating the stirring process, and self-stirring is relevant only when the companion has a very low eccentricity (in combination with a small semi-major axis).

2.6 Conclusions

We presented the first detection of a close low-mass stellar companion around the A0 star HD 193571. The three epochs obtained with VLT/NaCo and GPI confirm that the companion is co-moving with the host star, showing the potential of multi-band/multi-instrument follow-up to

confirm direct imaging candidates. Comparing M_H and $M_{L'}$ band photometry to evolutionary tracks suggests a mass of $\sim 0.305 \pm 0.025 M_\odot$ for an age of 66 Myr ($\sim 0.395 \pm 0.007 M_\odot$ for the 161 Myr case), which would make it an M2-2.5 dwarf. Comparison to observed spectra seems to suggest a surface gravity of ~ 4.9 and a temperature of ~ 3500 K. The orbital motion detected in the three epochs is not enough to place solid constraints on the orbital parameters, but allows us to confirm the co-motion with the host star and to exclude an edge-on orbit.

Given the projected separation of ~ 11 au and a maximum periastron of ~ 15 au, the companion appears to orbit interior to the circumstellar debris belt (inferred via SED IR-excess to be at ~ 120 au). We investigated the plausibility that both self- and companion-stirring mechanisms are responsible for the currently observed debris belt radius. Since no constraints can be put on the eccentricity, we cannot exclude a fully self-stirring scenario for the disc. However, a small deviation from a circular orbit would result in the disc being dominated by companion-stirring (as shown in Figure 2.6) and if the orbit is sufficiently eccentric the disc will appear eccentric as well. The companion is likely responsible for the stirring of a disc that appears to be an order of magnitude further away, showing how a massive companion can influence a debris disc at large distances.

At the moment, only a handful of systems are suited for a study of stirring mechanisms, and the HD 193571 system represents an important addition, containing the third known M-dwarf companion to a young star discovered to be orbiting within the primary's circumstellar disc, and the first one found around an A0-type star. In the future, radial velocity observations as well as a resolved image of the disc could be useful in deepening our understanding of this system.

3

Detection of H α emission from PZ Tel B using SPHERE/ZIMPOL

This chapter was published as a refereed article (Musso Barcucci et al. 2019a) in Astronomy & Astrophysics, for which I am the lead author and which has been adapted for this Thesis.

3.1 Introduction

In this Chapter, we present SPHERE/ZIMPOL angular differential imaging observations in H α of the known companion orbiting around the star PZ Tel. In Section 3.2 we present the target and in Section 3.3 we detail the observations and data reduction; we present the analysis and the results in Section 3.4 and we summarise our conclusions in Section 3.5.

3.2 PZ Tel B

PZ Tel (HD 174429, HIP 92680) is a G6.5 type star with an age of 24 ± 3 Myr (Jenkins et al. 2012, Bell et al. 2015), belonging to the β Pic moving group (Zuckerman et al. 2001) at a distance of ~ 47 pc (Gaia Collaboration et al. 2018). In 2010, two independent studies discovered a sub-stellar companion at a separation of ~ 0.3 arcsec: Mugrauer et al. (2010) with the NaCo instrument at the VLT, and Biller et al. (2010) with the Near-Infrared Coronagraphic Imager (NICI) at Gemini South. Both authors interpolated low-mass objects evolutionary tracks

Table 3.1: Fundamental parameters and properties of the PZ Tel system.

Parameter	value	
RA [hh:mm:ss]	+18:53:05.87	
DEC [dd:mm:ss]	-50:10:49.90	
Parallax [mas]	21.2186 ± 0.0602^a	
Distance [pc]	47.13 ± 0.13	
Age [Myr]	24 ± 3^b	
A_V [mag]	$0.53^{+0.84c}_{-0.53}$	
	PZ Tel A	PZ Tel B
Sp. Type	G6.5V ^c	M7±1
T_{eff} [K]	$\sim 5338 \pm 200^b$	2500-2700 ^{c d e}
Mass	$1.13 \pm 0.03 M_{\odot}^b$	38-72 M_J^e
[Fe/H] [dex]	0.05 ± 0.20^b	$0.30_{-0.30}^c$
$v \sin i$ [km/s]	73 ± 5^b	—
L [L_{\odot}]	1.16 ± 0.1^e	$0.002^{+0.0004c}_{-0.0003}$ 0.003 ± 0.0008^e

References. ^(a) Gaia Collaboration et al. (2018). ^(b) Jenkins et al. (2012). ^(c) Schmidt et al. (2014); due to the model grid used, it is not possible to place an upper limit on the companion’s metallicity. ^(d) Mugrauer et al. (2010). ^(e) Maire et al. (2016).

(Baraffe et al. 2002) and inferred a mass of $28_{-4}^{+12} M_J$ and $36 \pm 6 M_J$, which corresponds to a spectral type of M5-9. Following its discovery, the PZ Tel system has been the subject of several studies. Jenkins et al. (2012) use spectra obtained with the Fiber-fed Extended Range Optical Spectrograph (FEROS) to derive a rotational velocity of the host star of $v \sin i = 73 \pm 5 \text{ km s}^{-1}$, a metallicity of $[\text{Fe}/\text{H}] = 0.05 \pm 0.20$ dex, and an age of 5-27 Myr which led to a revised mass for PZ Tel B of $62 \pm 9 M_J$ via comparison with evolutionary models. Additional spectroscopic information was obtained with the Spectrograph for INtegral Field Observations in the Near Infrared (SINFONI) at the VLT (Schmidt et al. 2014), leading to a mass estimate for the companion of $M = 7.5_{-4.3}^{+16.9} M_J$, and a bolometric luminosity of $\log(L_{\text{bol}}/L_{\odot}) = -2.66_{-0.08}^{+0.06}$, which are independent of both age and evolutionary model used. More recently, Maire et al. (2016) obtained multi-band photometric observations of the companion using the InfraRed Dual-band Imager and Spectrograph (IRDIS), the Integral Field Spectrograph (IFS), and ZIMPOL at VLT/SPHERE, and derived a mass of 38-72 M_J (spectral type M7±1), which we use in this work. The observed mean activity strength value for this spectral type are -4.31 according to West et al. (2004), and -4.37 according to Kruse et al. (2010). Maire et al. (2016) also derived a bolometric luminosity for the companion of $\log(L_{\text{bol}}/L_{\odot}) = -2.51 \pm 0.10$. Riviere-Marichalar et al. (2014) obtained Herschel-PACS far-IR photometric observations at 70, 100, and 160 μm of 19 β Pic moving group members. They were able to exclude the presence of a substantial debris disc around PZ Tel, due to the non-detection of excess in the aforementioned bands, placing an upper limit on the infrared excess of $L_{\text{IR}}/L_{\star} < 2.3 \times 10^{-5}$. Table 3.1 summarises the host star and companion properties.

Table 3.2: Summary of observations and detector characteristics.

Parameter	Value	
Observational setup		
Observation date	30/05/2018	
Run ID	0101.C-0672(A)	
# Science frames	20	
# Flux frames	8	
# Centre frames	4	
DIT Science [s] ^a	220	
DIT Flux [s] ^b	52	
Tot. time [min] ^c	73.3	
Flux time [min] ^d	6.9	
Seeing [arcsec] ^e	0.9	
Tot. field rotation [deg] ^f	50.05	
Platescale [mas/pix]	3.6×3.6	
Coronagraph	V_CLC_M_WF	
ZIMPOL detector characteristics		
	Cnt_H α	N_H α
λ_0 [nm] ^g	644.9	656.34
$\Delta\lambda$ [nm] ^h	3.83	0.75
Cnt. Zp. [erg/cm ² /ADU/A] ⁱ	$1.59^{+0.05}_{-0.05} \times 10^{-17}$	$10^{+0.05}_{-0.05} \times 10^{-17}$
Line Zp. [erg/cm ² /ADU] ^j	—	$9.2^{+4}_{-0.5} \times 10^{-16}$

References. ^(a) Detector Integration Time for the science observations. ^(b) Detector Integration Time for the flux observations. ^(c) Total on source integration time for the science frames. ^(d) Total on source integration time for the flux frames. ^(e) Median seeing throughout the observations. ^(f) Total field rotation. ^(g) Filter central wavelength. ^(h) Filter equivalent width. ⁽ⁱ⁾ Continuum zeropoints from Schmid et al. (2017). ^(j) Line zeropoints from Schmid et al. (2017).

3.3 Observations and data reduction

We observed the PZ Tel system with the ZIMPOL instrument at VLT/SPHERE (Schmid et al. 2018), obtaining simultaneous coronagraphic ADI observations in the Cnt_H α and N_H α filter. The data were taken on UT 2018-05-30 in two observation blocks before and after the meridian passage, to maximise the total field rotation while allowing flexibility in the observing schedule. Each observing block consists of a set of science exposures with an integration time of 220 seconds, which were bracketed with non-saturated observations of the star with DIT=52 seconds, that we denote as flux frames. We also recorded a centre frame at the beginning and end of each observing block, in which a pattern is applied to the deformable mirror creating 4 bright copies of the central PSF outside of the coronagraph (in a symmetric pattern around the central star) which are used to compute the stellar position behind the coronagraph. The conditions were clear throughout the entire observations, with a median DIMM seeing of 0.9 arcsec. Standard bias, dark and flat calibrations were observed on the same night. Details of the observations, as well as main ZIMPOL detector characteristics, are summarised in Table 3.2.

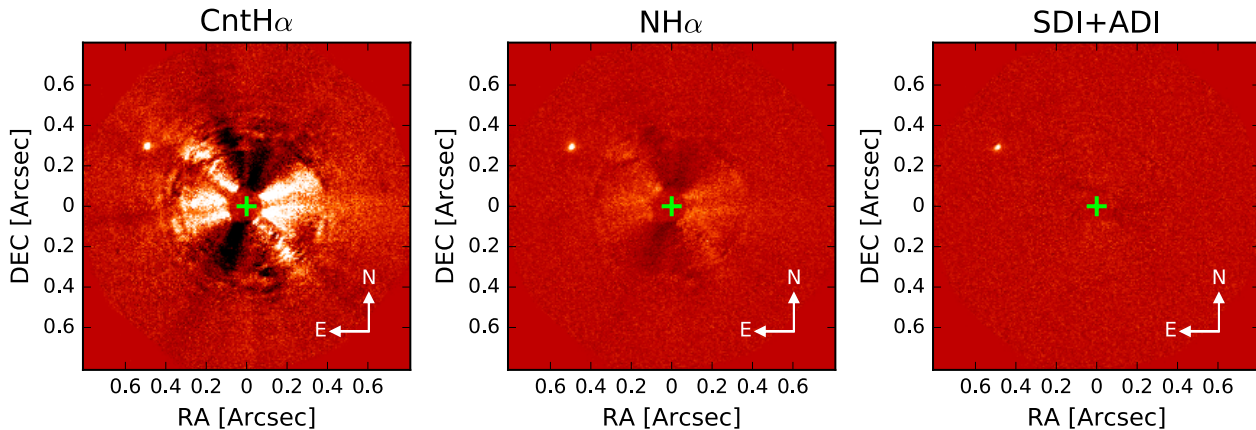


Figure 3.1: Reduced images showing PZ Tel B. In all three images the green cross marks the position of the central star, the data is oriented with North up, and the companion is clearly visible NE of the star. The images are normalised and the colour map was chosen for a better visualisation of the data. *Left panel:* classical ADI reduced image of the continuum H α filter frames. *Central panel:* classical ADI reduced image of the narrow band H α filter frames. *Right panel:* ASDI analysis.

The data was reduced using the ZIMPOL reduction pipeline developed and maintained at ETH Zürich which consists of: flat fielding, bias correction and dark subtraction, remapping the initial 7.2×3.6 mas/pix platescale into the squared grid of 3.6×3.6 mas/pix, and separating the frames in the two filters. The pipeline was applied to the flux, centre, and science frames. To account for possible shifting of the stellar position on the detector during the observations, we fitted a two dimensional gaussian to each spot in the 4 cosmetically reduced centring frames (and in both filters), computing the centre as intersection of the connecting lines. The final centre and relative error are the mean and standard deviation of these 4 centres (for each filter). We then re-centre the science frames using the `scipy.ndimage.interpolation.shift` package with spline interpolation of order 3, and cut them to stamps of 1.62×1.62 arcsec ending up with 20 cosmetically reduced and centred science frames for each filter. Since the unsaturated star is offset from the coronagraph and therefore visible, we fitted a two dimensional gaussian to re-centre the flux frames, ending up with eight cosmetically reduced and centred flux frames for each filter. The parallactic angle for each frame is automatically computed by the ZIMPOL pipeline, and takes care of a constant known offset of $134 \pm 0.5^\circ$ (Cugno et al. 2019; Maire et al. 2016) for which the frames must be rotated in the counterclockwise direction.

3.4 Analysis and results

The goal of this Chapter is to detect and quantify H α emission from the companion around PZ Tel, to expand the sample of known brown dwarfs and planetary companions with H α detection and better understand the formation and evolution of these objects. We also provide an additional

Table 3.3: Astrometry and flux contrast evaluated with *ANDROMEDA*, for both continuum and narrow band filter.

Parameter	Cnt_H α	N_H α
Sep. [arcsec]	0.5666 \pm 0.0036	0.5669 \pm 0.0036
P.A. [deg]	58.93 \pm 0.5	59.40 \pm 0.5
Flux contrast	(7.4 \pm 0.9) $\times 10^{-5}$	(29.0 \pm 3.5) $\times 10^{-5}$

astrometric measurement of the PZ Tel B, extending the time baseline by four more years. We clearly detected the companion in both Cnt_H α and N_H α filter, as shown in Figure 3.1. Even though the detection is clear in both filters, we also analysed the data with angular spectral differential imaging (ASDI) technique, shown in the rightmost panel of Figure 3.1. We refer to Appendix B.1, as well as [Cugno et al. \(2019\)](#), for a detailed explanation of the ASDI analysis.

3.4.1 Astrometry and flux contrast

We quantified the astrometry and flux contrast of the companion, for both filters, using the *ANDROMEDA* package ([Cantalloube et al. 2015](#)). This algorithm needs as input the cosmetically reduced frames, the corresponding parallactic angles, and an unsaturated PSF of the central star to create a model of the planetary signal signature, whose flux and position is fitted via a maximum likelihood estimation. We created this unsaturated image of the host star (for both filters) as median combination of all the flux frames, scaled to the DIT of the science frames. We set the inner working angle parameter to 1.0 λ/D (we refer to the *ANDROMEDA* paper for a detailed explanation of how the package works). The astrometry and flux contrast evaluated with *ANDROMEDA* are presented in Table 3.3.

3.4.2 Photometry

We followed the prescriptions from [Cugno et al. \(2019\)](#) to convert the flux contrasts into physical fluxes for both filters. The only difference was that, due to the presence of the coronagraph, we evaluated the flux of the host star using the flux frames instead of the science frames. Given the vicinity of the bands, we assumed that the continuum flux density is the same in both filters and we evaluated the flux in both. We then used the continuum flux density to evaluate the contamination of the narrow band filter due to continuum emission, and we corrected for it, obtaining the H α line flux. We refer to Appendix B.2 for a detailed step-by-step description of the analysis (we also performed an alternative photometric analysis described in Appendix B.3).

After correcting for extinction (see Appendix B.2 and Table 3.1), the total flux in the continuum filter, the total flux in the narrow band filter and the line flux, are:

$$F_{\text{Cnt.H}\alpha}^* = (5.68 \pm 0.18) \times 10^{-11} \text{ erg/cm}^2/\text{s}$$

$$F_{\text{N.H}\alpha}^* = (1.47 \pm 0.09) \times 10^{-11} \text{ erg/cm}^2/\text{s}$$

$$F_{\text{N.H}\alpha,\text{line}}^* = (3.53 \pm 0.8) \times 10^{-12} \text{ erg/cm}^2/\text{s}.$$

We now have the flux of the primary in the two filters and, together with the companion flux contrast (see Table 3.3), we can calculate the companion flux in both bands. The companion line flux is then the difference between the fluxes in the two filters (normalising the continuum flux to the width of the H α filter). The final values for the companion are:

$$F_{\text{Cnt.H}\alpha}^B = (1.92 \pm 0.9) \times 10^{-15} \text{ erg/cm}^2/\text{s}$$

$$F_{\text{N.H}\alpha}^B = (2.54 \pm 0.8) \times 10^{-15} \text{ erg/cm}^2/\text{s}$$

$$F_{\text{H}\alpha,\text{line}}^B = (2.17 \pm 0.9) \times 10^{-15} \text{ erg/cm}^2/\text{s}.$$

The companion H α line flux can be converted into a luminosity, multiplying by the squared distance, obtaining:

$$L_{\text{H}\alpha} = (1.51 \pm 0.05) \times 10^{-7} L_{\odot}.$$

Finally, we can evaluate the H α activity as the ratio between the H α luminosity and the bolometric luminosity of the object. For a bolometric luminosity of PZ Tel B of $\log_{10}(L_{\text{bol}}/L_{\odot}) = -2.66^{+0.06}_{-0.08}$ (Schmidt et al. 2014), we obtain an H α activity of $\log_{10}(L_{\text{H}\alpha}/L_{\text{bol}}) = -4.16 \pm 0.08$. Similarly, we obtain $\log_{10}(L_{\text{H}\alpha}/L_{\text{bol}}) = -4.31 \pm 0.1$ in the case of $\log_{10}(L_{\text{bol}}/L_{\odot}) = -2.51 \pm 0.10$ (Maire et al. 2016). The H α activity values agree within the errorbars.

3.4.3 Orbital constraints

Following its discovery in 2010, PZ Tel B has been observed several times in the last years, providing various astrometric measurements on an increasingly large time baseline. We compiled all the available astrometric datapoints from the literature in Table 3.4 and we show the position angle and separation of the companion through time in Figure 3.2. With our newly added observations, the available baseline is now ~ 12 years. Mugrauer et al. (2012) were the first to report a deceleration of the variation of the the angular separation of the companion, to be expected for an object moving on a Keplerian orbit towards apastron, which would support a bound orbit solution. Deceleration was also detected by Ginski et al. (2014) and Maire et al. (2016). We revisited the literature data and, together with our newly added astrometry, we further confirm this trend. The angular separation increases with a rate of $d_{\text{sep}}/t = 35.3 \pm 1.2 \text{ mas/yr}$ between June 2007 and September 2009, and then of $32.9 \pm 1.6 \text{ mas/yr}$ between September 2009 and September 2010.

The rate keeps decreasing all the way down to $27.7 \pm 0.6 \text{ mas/yr}$ between June 2012 and July 2014 and, finally, of just $23.0 \pm 0.3 \text{ mas/yr}$ between July 2014 and May 2018. Given the deceleration of the companion, we decided to restrict the following orbital analysis to bound orbits only ($e \leq 1$).

Table 3.4: Astrometric measurements for PZ Tel B available in the literature

Epoch	Separation	P.A.	Instrument	Filter	ref.
2007/06/13	255.6 ± 2.5	61.68 ± 0.6	NaCo	Ks	Mugrauer et al. (2012)
2009/04/11	330.0 ± 10	59.0 ± 1.0	NICI	CH ₄ 4% Long+Short	Biller et al. (2010)
2009/09/28	336.6 ± 1.2	60.52 ± 0.22	NaCo	Ks	Mugrauer et al. (2012)
2010/05/05-07 ^a	355.7 ± 0.8	60.33 ± 0.14	NaCo	J/H/Ks	Mugrauer et al. (2012)
2010/05/09	360.0 ± 3.0	59.4 ± 0.5	NICI	CH ₄ 1% Short	Biller et al. (2010)
2010/09/26	365.0 ± 8.0	59.2 ± 0.8	NaCo	L'	Beust et al. (2016)
2010/10/28	369.3 ± 1.1	59.91 ± 0.18	NaCo	Ks	Mugrauer et al. (2012)
2011/03/25	382.2 ± 1.0	59.84 ± 0.19	NaCo	Ks	Mugrauer et al. (2012)
2011/04/24	373.0 ± 9.0	58.7 ± 0.2	NICI	CH ₄ 4% Long+Short	Biller et al. (2013)
2011/05/03	394.0 ± 2.0	60.4 ± 0.2	NaCo	Ks	Beust et al. (2016)
2011/06/03-06 ^a	388.3 ± 0.5	59.69 ± 0.10	NaCo	Ks	Mugrauer et al. (2012)
2011/06/07	390.0 ± 5.0	60.0 ± 0.6	NaCo	L'	Beust et al. (2016)
2012/04/05	397.0 ± 9.0	60.4 ± 0.2	NICI	CH ₄ 4% Long+Short	Biller et al. (2013)
2012/06/08 ^a	419.4 ± 0.6	59.58 ± 0.03	NaCo	Ks	Ginski et al. (2014)
2014/07/13 ^a	477.46 ± 1.02	59.82 ± 0.24	SPHERE/IRDIS	H2&H3	Maire et al. (2016)
2014/08/07 ^a	479.65 ± 0.034	59.94 ± 0.23	SPHERE/IRDIS	K1&K2	Maire et al. (2016)

^(a)The quoted values are weighted means of several values presented in the cited papers.

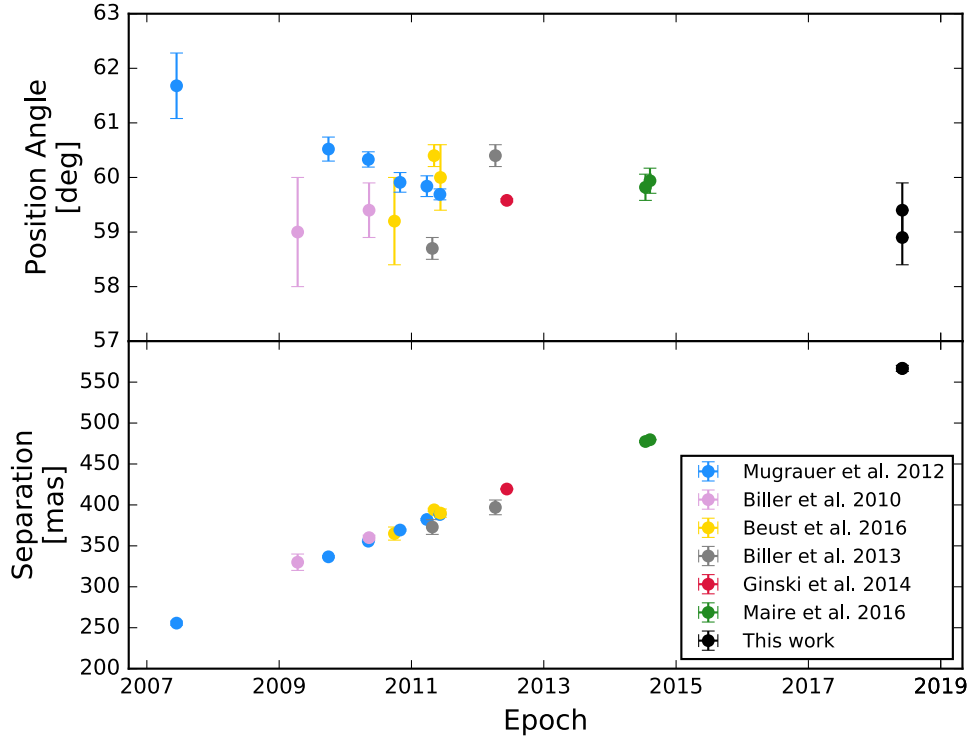


Figure 3.2: Separation and position angles of PZ Tel B, at various epochs. We show the astrometric values found in the literature (see Table 3.4) in various colours, together with the astrometry presented in this Chapter, for both filters (black points).

Given the newly extended astrometric baseline, we explored the possible orbital solutions using the Python package PyAstrOFit¹ (Wertz et al. 2017) which provides a series of tools to fit orbits using the emcee package (Foreman-Mackey et al. 2013) with the modified Markov chain Monte Carlo (MCMC) approach described in Goodman & Weare (2010). We assumed uniform prior

¹<https://github.com/vortex-exoplanet/PyAstrOFit>

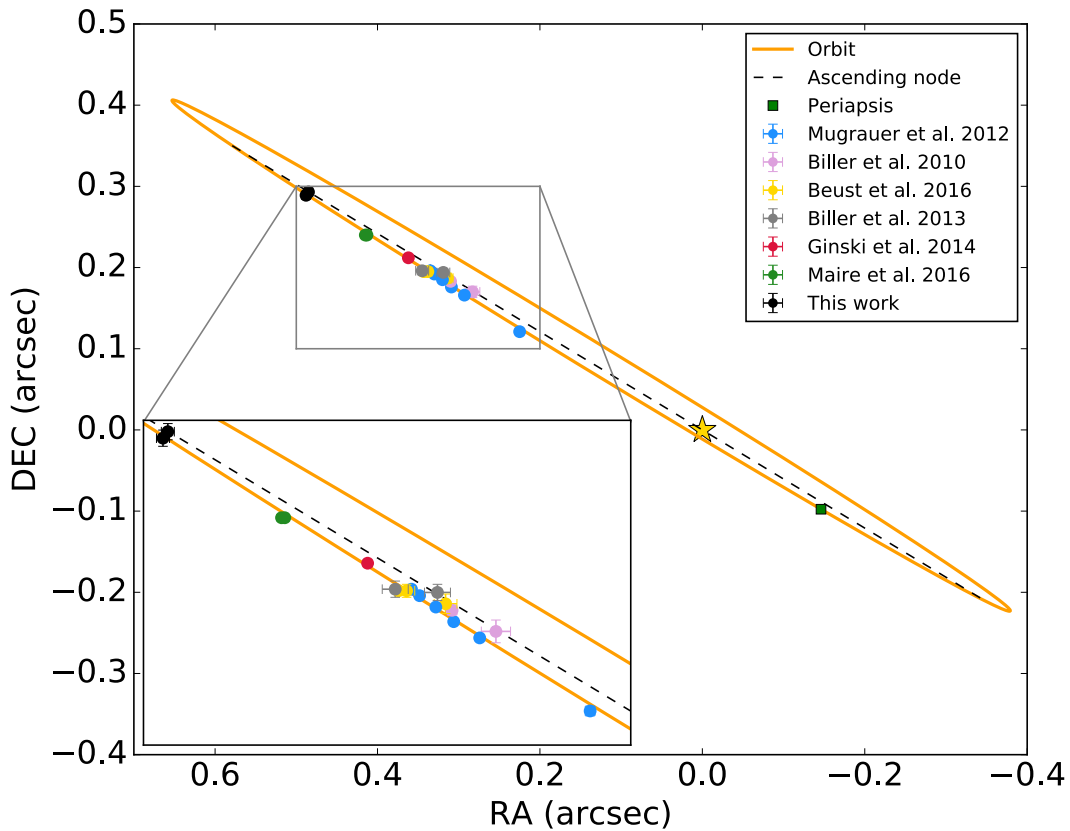


Figure 3.3: Best orbital solution found with PyAstrOFit. The orange line shows the orbit, the yellow star marks the position of the primary and the various astrometric measurements are shown with the same colour coding of Figure 3.2. The green square marks the position of the periapsis, and the dashed black line shows the position of the ascending node.

distribution for the semi-major axis (a), the eccentricity (e), the inclination (i), the longitude of ascending node (Ω) and argument of periastron (ω), and the time of periastron passage (t_p). Assuming a system mass of $1.2 M_\odot$ (see Table 3.1), we explored all possible bound solutions ($e \leq 1$), allowing a range of semi-major axis between 10 and 1200 au, an inclination between 10 and 180 degrees, and Ω and ω within natural boundaries. The only other hyperparameters are the number of walkers (which we set to 1200), and the scale parameter a , which directly impacts the acceptance rate AR (Mackay 2003) of the walkers. We manually tuned a to ensure an AR between 0.2 and 0.5. PyAstrOFit relies on the Gelman Rubin \hat{R} statistical test to check for convergence (Ford 2006; Gelman & Rubin 1992), which is considered reached when all the parameters pass the test three times in a row (with a threshold of $\hat{R} < 1.05$, where the closer the \hat{R} value is to 1 the closer the Markov chain is to convergence).

The posterior distributions of the orbital elements, as well as the correlation between them, is shown in the corner plot of Figure 3.4. The eccentricity distribution shows two peaks at ~ 0.55 and at 1, which is a lower boundary smaller than what found by previous studies ($0.62 < e < 0.99$ in Ginski et al. 2014 and $e \gtrsim 0.66$ in Maire et al. 2016) and significantly

Table 3.5: Best solutions in terms of reduced χ^2 and $1 - \sigma$ confidence intervals for all the orbital elements. These orbital elements have an associated χ^2_{red} of 2.15.

Parameter	Value
a [AU]	[21.4,39.9]
a_{χ^2}	31.3
e	[0.48,0.99]
e_{χ^2}	0.48
i [deg]	[90.7,92.1]
i_{χ^2}	91.6
Ω [deg]	[58.3,59.3]
Ω_{χ^2}	58.8
ω [deg]	[155.2,265.6]
ω_{χ^2}	239.2
t_p [MJD]	[49655.2, 53206.3]
t_{p,χ^2}	50346.6

smaller than the lower boundary of 0.91 found in the most recent orbital study of PZ Tel B, by [Beust et al. \(2016\)](#). A possible explanation for this difference lies in the different boundaries applied: [Beust et al. \(2016\)](#) allowed not-bound orbits while in this work we only considered orbits with $e < 1$. Our best solution for the semi-major axis of 31.3 au agrees with previous works ($17.86 < a < 1098$ au in [Ginski et al. 2014](#) and $a \gtrsim 24.5$ au in [Maire et al. 2016](#)). We found a best inclination of 91.6 degrees, which is in agreement with previous ranges of $91.3^\circ < i < 168.1^\circ$ for [Ginski et al. \(2014\)](#) and $91^\circ < i < 96.1^\circ$ for [Maire et al. \(2016\)](#). Previous confidence intervals for the longitude of ascending node were $50^\circ < \Omega < 70^\circ$ for [Ginski et al. \(2014\)](#) and $55.1^\circ < \Omega < 59.1^\circ$ for [Maire et al. \(2016\)](#), and [Ginski et al. \(2014\)](#) cited an interval of $122.2^\circ < \omega < 306^\circ$ for the argument of periastron. All of these agree with our best solutions of $\Omega = 58.8^\circ$ and $\omega = 239.2^\circ$. The best solution for the time of periastron passage corresponds to 1996.3, which agrees within the confidence intervals of previous works, but it is systematically lower than their best solutions (2002.9 for [Mugrauer et al. 2012](#), 2003.5 for [Ginski et al. 2014](#) and 2002.5 for [Beust et al. 2016](#)).

The best solutions in terms of reduced χ^2 and the $1 - \sigma$ confidence intervals are reported in Table 3.5. The orbit corresponding to these best parameters is shown in Figure 3.3, where we overplot the astrometric points (both from literature and from this work) as well as the position of the host star, the direction of the ascending node and the position of periastron. Our new astrometric datapoints are in agreement with previous measurements in terms of orbital elements, and help to tighten the uncertainties.

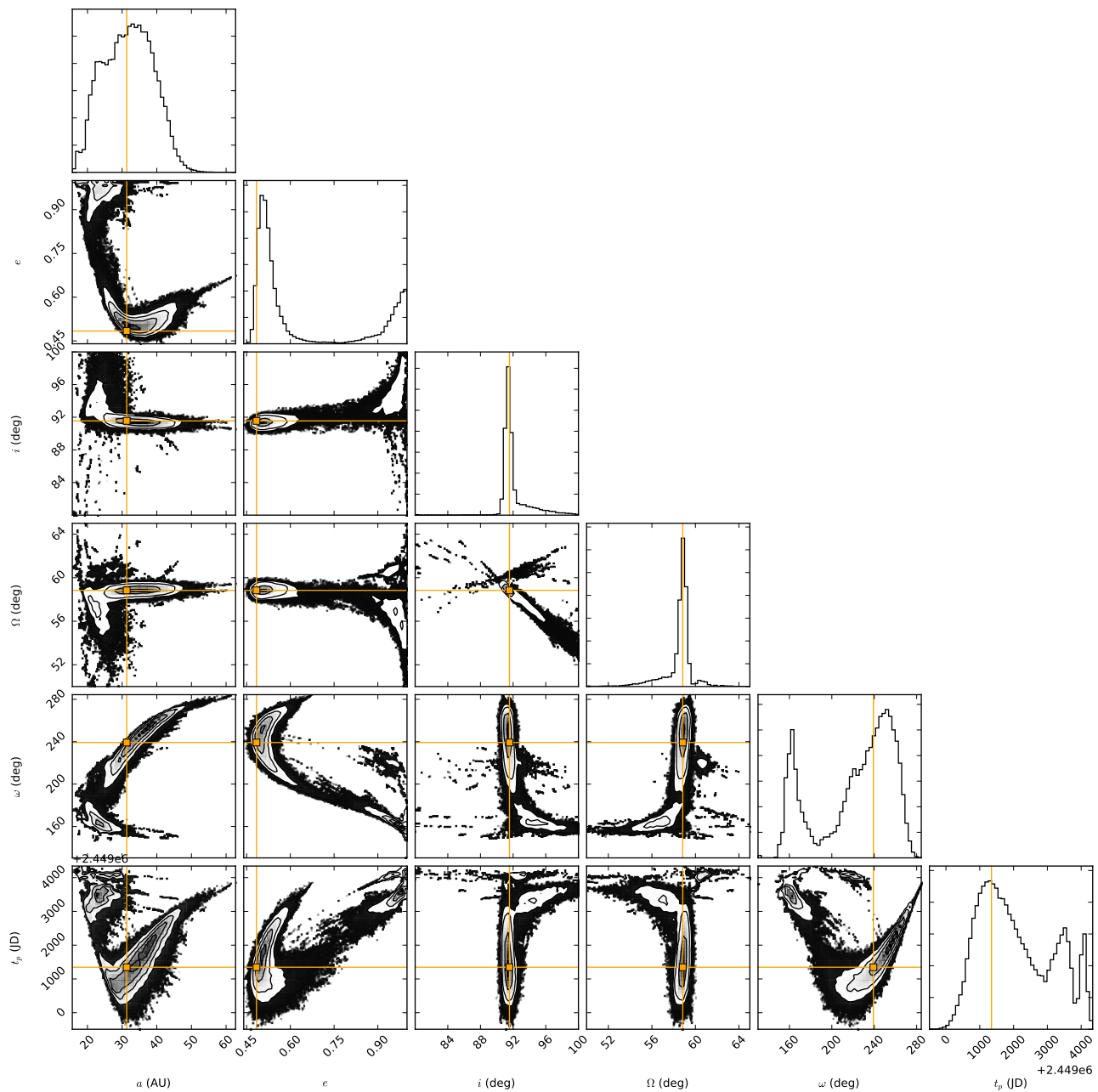


Figure 3.4: Posterior distributions of the orbital elements (*diagonal panels*) and correlation between the parameters (*off-axis panels*). The orange lines and squares mark the position of the best solution found in terms of reduced χ^2 , as reported in Table 3.5.

3.5 Discussion and conclusions

We presented SPHERE/ZIMPOL observations of the known sub-stellar M dwarf companion around PZ Tel, taken in both $H\alpha$ continuum and narrow band filter. We detected the companion in both datasets obtaining new astrometric and photometric measurements. This currently represents

the second only $H\alpha$ detection of a companion using the SPHERE instrument, and it further proves the capability of this instrument to detect $H\alpha$ signatures in binary systems.

We used our newly added astrometric data, together with values from the literature, to explore the allowed orbital solutions for PZ Tel B, finding orbital elements in agreement with what done in previous works (with the only exception being our lower boundary on the eccentricity). Our added data extends the available baseline for orbital studies of PZ Tel B up to ~ 12 years. We find that the companion is clearly decelerating over time, which is to be expected for a Keplerian bounded object moving towards apastron. We evaluated the $H\alpha$ luminosity and activity of PZ Tel B, finding values for $\log_{10}(L_{H\alpha}/L_{bol})$ of -4.16 ± 0.08 and -4.31 ± 0.10 , for bolometric luminosities of -2.66 and -2.51 , respectively.

Several studies investigated the $H\alpha$ activity in M dwarf, both as a function of spectral type and mass. [West et al. \(2004\)](#) evaluated the average $H\alpha$ activity as a function of spectral type, finding an average activity of -4.0 , -4.31 and -4.10 for spectral types of M6, M7 and M8, respectively. A later study from [Kruse et al. \(2010\)](#) found similar average activity levels of -3.89 , -4.35 and -4.17 for the same spectral types. Based on its spectral type, PZ Tel B thus appears to be slightly less active than the average, while still be consistent with the average values within the uncertainties.

Given the age of the system, and the absence of a known gaseous disc, it is unlikely that the observed $H\alpha$ luminosity is due to accretion processes. The fact that the activity level is consistent with what is expected for an object of spectral type M6-8, leads us to conclude that the most likely explanation for the $H\alpha$ luminosity observed in PZ Tel B is chromospheric activity.

Finally, we suggest that a possible explanation for the below average $H\alpha$ value of PZ Tel B is that the object has a variable emission and we happened to observe it during a moment of low activity. This reasoning is supported primarily by the late spectral type of the object, which is known to correlate with a higher variability level (see, e.g. [Kruse et al. 2010](#)); in addition, the companion has a high metallicity, which [Robertson et al. \(2013\)](#) correlated with a higher activity. However, follow-up $H\alpha$ observations would be needed to establish whether PZ Tel B displays a variable chromospheric activity.

4

LISStEN - the L' band Imaging Survey to find Exoplanets in the North

4.1 Introduction

In this Chapter we present LISStEN, the L' band Imaging Survey to find Exoplanets in the North, which main goal is to detect and characterise the population of giant planets in wide orbits around young nearby stars with circumstellar discs, and it has been designed to be North-hemisphere extension of the NaCo-ISPY survey, carried out at the ESO-VLT.

Specifically, the LISStEN survey aims at investigating the relation between a possible companion and the circumstellar disc surrounding its host star, and for this reason our target selection prioritises stars with known circumstellar discs, either inferred via SED fitting or with resolved images. The survey was carried out at the Large Binocular Telescope on Mount Graham in Arizona between Autumn 2017 and Spring 2019, using the L/M-band mid-InfraRed Camera (LMIRCam, [Skrutskie et al. 2010](#)) which is optimised to work in the mid-infrared ($3 - 5 \mu\text{m}$).

In Section 4.2 we detailed the target selection criteria, and in Section 4.3 we explain the observational strategy; the data reduction is presented in Section 4.4, together with the data analysis and the creation of contrast curves and mass detection limits. In Section 4.5 we explore the companion-disc interaction and which constraints this can place on the presence of a companion around a given target. Finally, we summarise our results in Section 4.6.

4.2 Target Selection

4.2.1 Target master list

Our initial source for targets was the Debris Disc Catalogue from the Spitzer Infrared Spectrograph (IRS) observations (Chen et al. 2014), to which we added targets from various sources in the literature, focusing on nearby stars with known and well characterised discs, both protoplanetary discs and older, more evolved, debris discs. We excluded targets for which deep ADI L' band imaging observations with substantial rotation field (i.e: $\geq 60^\circ$) were already present in the literature, in order to minimise the target overlap with other similar surveys, and we imposed a cut of 200 parsec on the distance. Telescope-specific selection criteria include: a cut at $\text{DEC} \leq -15$ degrees in order for the targets to be observable from the LBT, an R magnitude cut at 13 mag (the minimum brightness compatible with the AO system), and the exclusion of close separation ($< 1.0''$) same-magnitude binaries which could create issues for the AO during observations.

We ended up with a final master target list, from which we had the flexibility of selecting suitable targets depending on the given allocated observing nights every semester. During observations, if multiple targets were available, we prioritised nearby targets (in order to probe the $\sim 2 - 10$ au region close to the star) and those targets with a resolved disc (see Section 4.2.2). A total of 29 targets were observed as part of the LStEN survey during several observing nights between the Autumn semester 2017 and the Spring semester 2019, and they are presented in Table 4.1. Of these, five are PPD hosting targets, 22 are surrounded by significant and confirmed DDs, while 2 have a less significant IR excess and an uncertain DD status. For the rest of this Chapter, we will be focusing on the DD targets only (both the confirmed and the uncertain ones), while the analysis of the PPD targets will be presented in an incoming paper (Musso Barcucci+2020, in prep).

The target distances come from the GAIA Data Release 2 Catalogue (Bailer-Jones et al. 2018; Gaia Collaboration et al. 2018) and the Spectral types are from the Simbad database; the ages come from various sources in the literature (see Table 4.1) which explains the scatter in the age uncertainties for the various targets. The stellar masses come from Kervella et al. (2019), except when stated otherwise in the Table. Regarding the L' band magnitudes, starting from the WISE W1 and W2 magnitudes we first computed the colour-corrected fluxes in the two bands (using zeropoints from Jarrett et al. 2011 and colour-correction factors from Wright et al. 2010); we then obtained the L' flux as an interpolation at the L' wavelength (and integrating it over the L' band filter curve¹), and we finally converted this into an L' band magnitude using the zeropoint provided in Tokunaga (2014).

¹Obtained via private communication.

Table 4.1: LStEN survey: summary of targets parameters

Target	RA [hh:mm:ss]	DEC [dd:mm:ss]	Distance [parsec]	Age [Myr]	Age ref.	L' [mag]	Sp. Type	M_{\star} [M_{\odot}]
HD 206860	21 44 31.2	+14 46 19.97	18.1	100-500	a	4.44 ± 0.14	G0 V	1.081 ± 0.054
V* DE Tau	04 21 55.6	+27 55 06.0	126.9	1^{+1}_{-4}	b	6.88 ± 0.03	M1	0.41 ^(b)
HD 183324	19 29 01.0	+01 57 01.6	60.6	527^{+103}_{-62}	c	5.50 ± 0.10	A0 V	1.95 ± 0.097
HD 220825	23 26 55.9	+01 15 20.19	48.9	195^{+111}_{-55}	c	4.85 ± 0.19	F0	2.2 ± 0.11
HD 35187	05 24 01.2	+24 57 37.58	162.3	9 ± 2	d	5.00 ± 0.10	A2	$1.767, \pm 0.088$
EM* LkHA 330	03 45 48.3	+32 24 11.8	$308.4^{(1)}$	2.5 ± 0.7	j	5.76 ± 0.07	G3	$2.8 \pm 0.2^{(i)}$
HD 184930	19 36 43.3	-01 17 11.8	$216.9^{(1)}$	99.9 ± 7.5	e	4.45 ± 0.13	B5 III	6.188 ± 0.309
HD 221853	23 35 36.2	+08 22 57.4	65.3	100	f	6.38 ± 0.05	F0	1.4 ± 0.07
JH 112	04 32 49.1	+22 53 02.0	163.8	2.99	h	7.27 ± 0.03	K6	0.69 ^(h)
HD 127821	14 30 46.1	+63 11 08.8	31.7	1756^{+2199}_{-817}	c	5.37 ± 0.12	F4 IV	1.3 ± 0.065
HD 191174	20 04 44.5	+63 53 24.7	83.7	355	f	6.13 ± 0.10	A2	2.0 ± 0.1
HD 110897	12 44 59.4	+39 16 44.1	17.5	9700	g	4.27 ± 0.18	G0 V	1.081 ± 0.054
HD 128311	14 36 00.6	+09 44 47.5	16.3	390	g	5.14 ± 0.11	K3 V	0.826 ± 0.041
HD 152598	16 52 58.1	+31 42 06.0	29.6	1313^{+379}_{-224}	c	4.49 ± 0.13	F0 V	$1.5, \pm 0.075$
HD 182919	19 26 13.3	+20 05 51.8	71.8	198	f	5.63 ± 0.08	A0 V	2.5 ± 0.125
HD 116956	13 25 45.5	+56 58 13.8	21.6	260	i	5.35 ± 0.11	G9 V	0.961 ± 0.048
HD 161868	17 47 53.6	+02 42 26.20	30.0	260^{+166}_{-78}	c	3.57 ± 0.26	A0 V	2.415 ± 0.121
HD 192425	20 14 16.6	+15 11 51.4	47.9	413^{+94}_{-56}	c	4.68 ± 0.14	A2 V	2.2 ± 0.11
HD 36112	05 30 27.5	+25 19 57.08	160.2	3.7 ± 2.0	d	4.37 ± 0.14	A8	1.911 ± 0.096
HD 50554	06 54 42.8	+24 14 44.01	31.2	4680	g	5.44 ± 0.10	F8 V	1.158 ± 0.058
HD 219498	23 16 05.0	+22 10 34.82	56.9	320	g	7.36 ± 0.03	G5	0.92 ^(g)
HD 205811	21 37 43.6	+06 37 06.20	88.1	396^{+63}_{-44}	c	6.09 ± 0.06	A2 V	1.6 ± 0.08
HD 8907	01 28 34.4	+42 16 03.69	33.2	320	g	5.39 ± 0.10	F8	1.2 ± 0.06
HD 32977	05 07 48.4	+20 25 06.16	61.9	299^{+321}_{-127}	c	5.02 ± 0.13	A5 V	2.326 ± 0.116
HD 48682	06 46 44.3	+43 34 38.74	16.6	3310	g	3.72 ± 0.19	F9 V	1.2 ± 0.06
HD 212695	22 26 14.4	-02 47 20.32	48.1	1846^{+2371}_{-846}	c	5.83 ± 0.07	F5	1.372 ± 0.069
HD 113337	13 01 46.9	+63 36 36.79	36.2	1631^{+2208}_{-841}	c	4.92 ± 0.14	F6 V	1.4 ± 0.07
HD 143894	16 02 17.7	+22 48 16.02	51.3	465^{+142}_{-84}	c	4.59 ± 0.12	A3 V	2.5 ± 0.125
HIP 83043	16 58 08.9	+25 44 38.97	10.4	4500	k	5.50 ± 0.09	M2 V	0.532 ± 0.01

(1) Current GAIA DR2 distance estimation. These targets were selected and observed prior to the release of the GAIA DR2, and they were thought to have a distance <200 pc, which is why they were observed.

References. ^(a) Luhman et al. 2007; Zhou et al. 2018. ^(b) Grankin 2016. ^(c) David & Hillenbrand 2015. ^(d) Meeus et al. 2012. ^(e) Lyubimkov et al. 2002. ^(f) Kennedy & Wyatt 2014. ^(g) Kains et al. (2011). ^(h) Küçük & Akkaya 2010. ⁽ⁱ⁾ Lehtinen et al. 2016. ^(j) Uyama et al. 2018. ^(k) Veyette & Muirhead 2018.

We show the age, distance and spectral type distributions for all of our 29 LStEN targets in Figure 4.1. The median distance for our survey is ~ 49 pc (the closest target being at ~ 10 pc and the furthest away at ~ 308 pc), and given an Inner Working Angle (IWA) of $\sim 0''.150$ (see Section 4.3) and the LMIRCam detector plate scale of 10.707 ± 0.012 mas/pix, we are theoretically sensitive to regions within 10 au from the star for 20 out of our 29 targets. The ages span from 1 to 9700 Myr (with a median age of 320 Myr), while the median spectral type for our survey is A, with most stars being either A or F type.

4.2.2 Notes on individual targets

Out of the 24 targets observed during our survey (we will not consider the 5 PPD ones in the present work), 14 have a resolved debris disc (at the moment of writing), and 5 have known planetary mass companions. Even though in some cases these systems are well known, we did

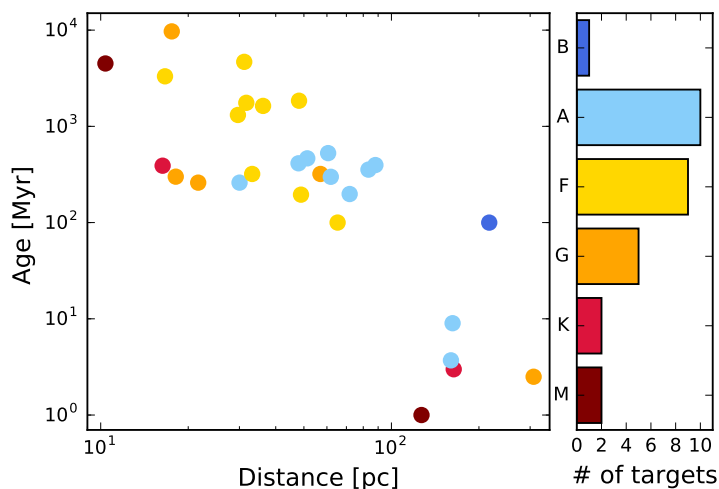


Figure 4.1: Age, distance and spectral type distributions for all the L^IStEN targets. We did not show the age or distance uncertainty. The stars are colour-coded according to their spectral type.

not find any available deep L' band imaging ADI data (with field rotation $\geq 60^\circ$) in the literature, thus making them perfect candidates for our survey. We decided to priorities these targets, both those with a resolved disc and those with known planetary companion(s). We discuss individual cases in the following sections, and summarise the disc and companion information for all of them in Table 4.2.

4.2.2.1 HD 206860

HD 206860 (V* HN Peg, HIP 107350) is a solar-type star at a distance of ~ 18 parsec. In 2006, [Luhman et al. \(2007\)](#) discovered a substellar companion orbiting the host star at an angular distance of $> 43''$, using the Spitzer Space Telescope. Comparing the luminosity of the object to theoretical evolutionary models, they estimated a mass of $\sim 16 M_J^2$. Given the large separation of the companion (~ 790 au), and since our survey focuses on characterising the close-in (≤ 10 au) GP population, we decided to keep this target as part of the L^IStEN survey.

4.2.2.2 HD 183324, HD 191174 and HD 192425

HD 183324, HD 191174 and HD 192425 are early type stars for which [Morales et al. \(2016\)](#) obtained Herschel/PACS imaging data at 70, 100 and 160 μm , with the aim of spatially resolving the outer belt around these double-belt systems. The dust emission is fit with a thin ring model with three main parameters: radius, inclination and position angle.

²See also http://exoplanet.eu/catalog/hn_peg_b/.

They resolved the colder belt around HD 183324 in all three bands, obtaining a disc radius (at $100\ \mu\text{m}$) of $2''.9 \pm 0''.6$, with an inclination of $21^\circ \pm 42^\circ$. The outer belt around HD 192425 is resolved only at 100 and $160\ \mu\text{m}$, with a disc size of $4''.8 \pm 0''.3$ and an inclination of $63^\circ \pm 5^\circ$. The outer disc around HD 191174 is only partially resolved at $100\ \mu\text{m}$, yielding a disc size of $3''. \pm 0''.7$ but no constraints on the inclination.

4.2.2.3 HD 48682, HD 143894, HD 161868, HD 212695 and HD 127821

Five of our targets were imaged with the James Clerk Maxwell telescope (JCMT) as part of the SONS survey of debris discs (Holland et al. 2017). They obtained sub-millimetre images at 850 and $450\ \mu\text{m}$ and, via radial profile fitting, derived radial extent, inclination and position angle for all the sources with a resolved emission, while providing disc size upper limits for the unresolved ones.

The discs around HD 48682, HD 143894 and HD 161868 were all resolved at $850\ \mu\text{m}$, with an estimated disc size of $11''. \pm 3''.9$, $10''.2 \pm 2''.5$ and $7''.8 \pm 2''.2$ respectively. They derive a disc inclination of $67^\circ \pm 24^\circ$ for HD 143894, and provide a lower limit of 47° on the disc inclination for HD 48682, and 16° for the disc around HD 161868.

The discs around HD 212695 and HD 127821 were unresolved, yielding to a disc upper limit of $7''.5$ and $7''.4$, respectively.

4.2.2.4 HD 110897

HD 110897 is a solar type star at a distance of ~ 17.5 parsec. Herschel/PACS observations were obtained as part of the DUNES and DEBRIS surveys, with the aim of resolving and characterising its circumstellar disc (Marshall et al. 2014). Extended emission from the disc is resolved in the 70, 100 and $160\ \mu\text{m}$ bands, and the best fit model is a cool, broad dust ring with a peak in the surface brightness at $\sim 3''.1$ (~ 50 au) and an inclination of $56^\circ \pm 10^\circ$. Our survey will therefore be able to explore the region within the disc, making this target a perfect candidate for LISTEN.

4.2.2.5 HD 50554

HD 50554 is an F8 type star at a distance of ~ 31 parsec, with a known planetary mass companion discovered with the RV technique by the ELODIE survey (Perrier et al. 2003). The companion has an estimated mass of $m_p \sin i = 5.16 M_J$ and a semi-major axis of 2.41 au.

Herschel/PACS observations at 70, 100 and $160\ \mu\text{m}$ revealed an extended emission around the host star (Dodson-Robinson et al. 2016), which best fit yields a disc size of $1''.45 \pm 0''.13$ (45 ± 4

au). The L^IStEN survey is designed to explore regions up to ~ 10 au around its targets, and this star is therefore a very interesting candidate which would allow us to explore the gap between the known planetary companion at a few au and the further away disc at few tens of au.

4.2.2.6 HD 8907

HD 8907 was observed with the Submillimeter Array (SMA) and Combined Array for Research in Millimeter-wave Astronomy by [Steele et al. \(2016\)](#), resolving its debris disc for the first time. The best fit of the SED and resolved images yields a disc size of $1''.59 \pm 0''.76$ with an inclination of 65° . HD 8907 was also observed by [Holland et al. \(2017\)](#) during the SONS survey, obtaining an upper limit on the disc of $5''.1$, in agreement with the results of [Steele et al. \(2016\)](#).

4.2.2.7 HIP 83043

HIP 83043 (GJ 649, BD+25 3173) is a nearby (~ 10 parsec) M type star, which was observed with Herschel/PACS at 100 and 160 μm by [Kennedy et al. \(2018\)](#). They partially resolve the disc at 100 μm , and conclude that the emission is consistent with an edge-on disc with an extent between $\sim 1''$ and $\sim 2''.9$ (10 to 30 au).

The host star is also known to harbour a companion discovered with the RV technique by [Johnson et al. \(2010\)](#), with an estimated mass of $m_p \sin i = 0.328 M_J$. At a distance of ~ 1.1 au, the companion resides well within the disc.

This target is an excellent candidate for the L^IStEN survey, since its distance and our IWA of $\sim 0''.150$ (see Section 4.3) mean that we would be able to probe the gap between the known RV planet and the resolved circumstellar disc.

4.2.2.8 HD 128311

HD 128311 (HIP 71395, GJ 3860) is a K type star at a distance of ~ 16 parsec, hosting two close-in planetary mass companions discovered with the RV method: HD 128311 b, with an estimated mass of $m_p \sin i = 2.18 M_J$ and a semi-major axis of ~ 1 au, and HD 128311 c with a mass of $4.19 M_J$ and semi-major axis of 1.76 au ([Butler et al. 2003](#); [Vogt et al. 2005](#)). The star is also known to harbour a circumstellar disc with a radius of 58 au^3 . The L^IStEN survey is therefore perfectly designed to probe the region between the two known RV planets and the debris discs, allowing us to gain more information on this interesting system.

³From the Catalog of resolved debris discs, compiled and maintained at <https://www.astro.uni-jena.de/index.php/theory/catalog-of-resolved-debris-disks.html>.

Table 4.2: LStEN survey: summary of resolved discs and hosted planets

Target	R_{res} [au]	i°	PA $^\circ$	Ref.	$m_p \sin i$ [M_J]	a_p [au]	Instrument used
HD 206860	—	—	—	—	16 ± 9.4^1	795	—
HD 183324	176 ± 36	21 ± 42	—	a	—	—	Herschel
HD 127821	< 235	—	—	b	—	—	JCMT
HD 191174	250 ± 58	—	—	a	—	—	Herschel
HD 110897	53.7	56 ± 10	111 ± 2	d	—	—	Herschel
HD 128311	58	—	—	h	2.18 4.19^1	1.099 1.76	N/A ³
HD 161868	234 ± 66	≥ 16	75 ± 17	b	—	—	JCMT
HD 192425	230 ± 15	63 ± 5	98 ± 5	a	—	—	Herschel
HD 50554	45 ± 4	—	—	e	5.16	2.41	Herschel
HD 8907	53 ± 26	~ 65	~ 55	f	—	—	SMA
HD 48682	183 ± 65	≥ 47	94 ± 19	b	—	—	JCMT
HD 212695	≤ 361	—	—	b	—	—	JCMT
HD 113337	85 ± 20	25^{+5}_{-15}	128 ± 5	c	7^{+4}_{-2} 16^{+10}_{-3}	1.03 4.8	Herschel
HD 143894	524 ± 129	67 ± 24	70 ± 15	b	—	—	JCMT
HIP 83043	10 – 30	~ 90	—	g	0.328	1.1	Herschel

(1) These masses are physical masses and not $m_p \sin i$ ones.

References. ^(a) Morales et al. 2016. ^(b) Holland et al. 2017. ^(c) Borgniet et al. 2019b. ^(d) Marshall et al. 2014. ^(e) Dodson-Robinson et al. 2016 ^(f) Steele et al. 2016. ^(g) Kennedy et al. 2018. ^(h) See footnote 3.

4.2.2.9 HD 113337

HD 113337 is a main-sequence star at a distance of ~ 36 parsec, known to harbour a debris disc due to its infrared excess, and at least one confirmed giant planet with a mass of $3.1 M_J$ at ~ 1 au and one companion candidate with a mass of $7.2 M_J$ at ~ 5 au (Borgniet et al. 2014, 2019a).

Borgniet et al. (2019b) carried out an extensive study of this system, partially resolving its debris disc for the first time at 70 and 160 μm with Herschel/PACS, and obtaining ADI L' -band data using the LMIRCam at LBT. They derived a disc size of 85 ± 20 au with an extension of 30 ± 20 au, and an inclination of $10 - 30^\circ$. Combining RV data, imaging contrast limits, age and inclination solutions, they derive an estimate for the true masses of the two companions of $7^{+4}_{-2} M_J$ for the confirmed companion HD 113337 b, and $16^{+10}_{-3} M_J$ for the candidate companion HD 113337 c.

We observed HD 113337 in the context of the LStEN survey prior to the publication of the study from Borgniet et al. (2019b); furthermore, the L' band ADI observations presented in Borgniet et al. (2019b) were obtained in January 2015 and thus our additional imaging data would allow us to span a baseline of more than 4 years. For these reasons we decided to keep HD 113337 in our target list and to analyse it independently of the results of Borgniet et al. (2019b), while keeping them in mind as a useful benchmark.

Table 4.3: LStEN survey: summary of observations

Target	Obs. date [dd/mm/yy]	Setup	median seeing [arcsec]	DIT [sec]	DIT - Flux [sec]	Tot. rotation [deg]
HD 206860	06/10/17	Dual	0.89	0.7	0.7 + ND filter	66.1
HD 183324	07/10/17	Dual	0.94	0.7	0.7 + ND filter	27.6
HD 220825	07/10/17	Dual	1.14	0.7	0.7 + ND filter	74.7
HD 184930	08/10/17	Dual	0.81	0.7	0.3 + ND filter	24-30 ^b
HD 221853	08/10/17	Dual	1.09	0.7	1.4 + ND filter	63-87 ^c
HD 127821	27/05/18	SX	1.50	0.7	0.3 + ND filter	62.3
HD 191174	27/05/18	Dual	1.40	0.7	1.4 + ND filter	55
HD 110897	28/05/18	SX	0.95 ^a	0.7	0.3 + ND filter	259.5
HD 128311	28/05/18	Dual	0.95	0.7	0.3 + ND filter	59.2
HD 152598	28/05/18	Dual	1.19	0.7	0.3 + ND filter	162.8
HD 182919	28/05/18	Dual	1.15	0.7	0.3 + ND filter	103.2
HD 116956	29/05/18	Dual	1.10	0.7	0.3 + ND filter	61.9
HD 161868	29/05/18	Dual	1.07	0.3	0.3 + ND filter	48.6
HD 192425	29/05/18	Dual	0.9	0.7	0.3 + ND filter	75.0
HD 50554	25/10/18	DX	0.96	1.112	0.109	105.2
HD 219498	25/10/18	DX	1.22	1.112	0.302	83.1
HD 205811	26/10/18	Dual	1.42	0.700	0.109	69.1
HD 8907	27/10/18	SX	1.43 ^a	0.810	0.027	113.5
HD 48682	27/10/18	DX	1.43 ^a	0.508	0.027	48.1
HD 212695	27/10/18	SX	1.43	1.208	0.109	63.0
HD 32977	27/10/18	SX	1.43 ^a	1.002	0.109	79.6
HD 113337	25/02/19	Dual	1.46	1.00265	0.05494	59
HD 143894	25/02/19	Dual	0.88	0.810365	0.013735	88.3
HIP 83043	18/04/19	Dual	1.14	1.00265	0.05494	87.4

The single decimal digit DIT's cited in the table are approximations of the actual available DIT for the LMIRCam: 0.364088 sec, 0.728176 sec, 1.456352 sec, 1.8204401 sec. The 'ND filter' refers to the 10% neutral density filter 'ND1.0-T10'.

References. ^(a) The seeing was not recorded due to a detector issue, we will use the last seeing recorded for this night as representative of the weather condition for the rest of the night. ^(b) Due to AO issues, we had to carry part of the observations in single-sided mode, resulting in a total field rotation of 30.3 degrees for the SX mirror and 24.6 degrees for the DX one. ^(c) similarly to HD 184930, we obtained unequal observations with the two mirrors, for a total rotation of 87.1 degrees for SX and 63.1 degrees for DX.

4.3 Observations

Observations were carried out using the LMIRCam (Skrutskie et al. 2010) at the Large Binocular Telescope in Arizona using the L' band filter at $3,8\ \mu\text{m}$, during 11 nights between October 2017 and April 2019. All the observations were carried out in visitor mode, with the only exception of the Spring 2019 run.

Our observational strategy makes use of the two 8.4 meters mirrors of the LBT simultaneously, and consists of L' band Angular Differential Imaging observations in non-overlapping dual mode, bracketed with unsaturated flux measurements in order to create an unsaturated PSF reference for each mirror. The dual mode allows to keep the light coming from the two mirrors separated on the detector, and thus creating two images of the same star, allowing for two simultaneous and semi-independent observations of a given target.

During observations we positioned the star images on the left side of the detector at a distance of $\sim 5''$ from each other (to avoid cross-contamination between the two PSF's) and collected data with a left-right nodding pattern with a typical frequency of 150 frames per side (10 frames per side for the unsaturated flux measurements). The exposure time for the science frames was chosen in order to maximise the sensitivity per each target, while avoiding the PSF core to saturate beyond $\sim 0''.100 - 0''.150$, and it was typically around ~ 1 second. Given the average distance between the star images (from the two mirrors), and to avoid cross-contamination between the two PSF's, our observational setup allows us to probe the region around a given target between $\sim 0''.150$ and $\sim 2''$. The exposure time for the flux measurements was chosen so to avoid saturation of the PSF, and for certain targets we had to use a 10% neutral density filter. We aimed at observing each target for a minimum of 2 hours around its meridian passage, to achieve a total field rotation of ≥ 60 degrees.

We adopted this same observational strategy for all the LStEN targets as much as possible, however we had to carry single-sided observations for some of our targets due to technical issues with either of the AO systems. The observing dates for all of our DD targets, together with flux and science DIT's, information on single or dual mode observations, and total field rotation, are reported in Table 4.3.

4.4 Data Reduction & Analysis

4.4.1 Data processing

All data are reduced with our own reduction pipeline, which has been tailored to the specific observational strategy we adopted. The creation of the master flats and the bad pixel maps

is detailed in Appendix C.1. The pipeline is fully automatised, except for a few initial target-dependent parameters that need to be input manually. The type and purpose of these parameters, as well as a full description of the data reduction pipeline, is detailed as follows:

- *Data organisations*

The frames are separated in unsaturated flux frames and saturated science frames depending on their DIT's, and all the frames with the 'bad frame' tag in the header are removed. This tag is automatically created during the observations for those frames that exhibit a clearly bad behaviour, i.e: in the case in which a wrong offset is applied to the target, the entire frame is almost completely saturated, and similar extreme cases. The following analysis was performed on both the flux and the science frames, separately.

- *Locating the star(s) position*

According to the target-dependent bad pixel map (see Section C.1), the bad pixels are masked and then the image is smoothed out using the *ndimage.gaussian_filter* of the *scipy* Python package, with $\sigma = 2$ pixels. The rough position of the star(s) is finally found as the position of the absolute maximum(a) (above a manually set threshold) in this masked, smoothed frame. Only frames in which the correct target-dependent number of stars is found are then used (either one or two stars, whether it is a single or double dish observation).

- *Nod separation*

The frames are divided into the two nod positions (nodA and nodB), according to the position of the star(s) in each frame and the target-dependent pixel separation between the nods.

- *Sky subtraction*

A master sky is created from each nod with a pca-based approach. Each frame in a given nod is sky-subtracted using the master sky created with the other nod, and flat fielded using the target-dependent master flat (depending on the observing run). During this step the bad pixels are masked out according to the target-dependent bad pixel map. The frame is then cut into two, separating the DX and SX mirror (only for dual-mirror observations), and each sub-frame is saved separately. From now on, the frames for different mirrors are reduced separately and independently from each other.

- *Bad pixel correction*

The bad pixels are now corrected for by interpolating from the neighbouring pixels with a gaussian kernel with standard deviation of 2 pixels.

- *Bad stripes correction*

The pixel-corrected frames are padded with zero to regain the initial target-dependent window size. In each frame, the median of all the pixel values throughout the entire datacube (for a given pixel) is subtracted from that pixel to correct for bad stripes and similar effects. To avoid contamination from the star and possible contamination from the other mirror's star at the edge of the frame, the median evaluation is done on a datacube in which a square of size 100x100 pixels around the position of the star is blanked out, as well as a frame of 120 pixels in width all around the edges of the frame. These final padded and median-subtracted frames are saved.

- *De-warping*

Every frame is now corrected for the distortion introduced by the secondary mirror and by the fact that the pixels on the CCD detector are not in a perfect cartesian grid. The distortion correction coefficient for a given semester are available on the LBTO webpage⁴. Since these corrections have been evaluated for the entire detector array of 2048x2048 pixel, the frames are accordingly padded with zeros before being de-warped. The de-warped frames are then cut down again to their target-dependent window size before being saved.

- *Centring*

The position of the star on these de-warped frames is re-evaluated as the position of the maximum pixel value, and the frame is cut in a square shape around this position with a fixed stamp size of 400×400 pixels. A finer sub-pixel centring is then performed finding the 2-dimensional gaussian centroid of each frame. the final centred frames are then saved in their respective mirror folder.

- *Stacking*

This step was performed only for the science frames. The frames with less than 0.1 deg change in the parallactic angles are stacked together (i.e: mean combined) to reduce the total amount of frames. This is helpful in the subsequent data analysis to maintain manageable computational times for each target. This stacking does not influence significantly the achievable detection limits and it seems, for certain targets, to even improve them (see Appendix C.2).

For the rest of the analysis we use these reduced stacked science frames, keeping the analysis of the two mirrors separated and independent from each other.

The reduced flux frames are median-combined (for each mirror) to create one single reduced flux frame per mirror (for each target). These flux frames are then scaled according to the DIT's

⁴<https://sites.google.com/a/lbto.org/lbti/data-retrieval-reduction/distortion-correction-and-astrometric-solution>

of the science frames and used to create and inject fake negative planets during the creation of contrast curves (see Section 4.4.3).

4.4.2 PynPoint analysis

The reduced data was analysed using the PynPoint package (Amara & Quanz 2012; Stolker et al. 2019) which uses a principal components analysis (PCA) based approach to model and subtract the central PSF, where the main parameter is the number of principal components (PC) used. We refer to the aforementioned papers for a detailed explanation on the functionality of the package and its various modules.

We resized the frames to stamps of size $4''.2 \times 4''.2$, and we used a central mask of $0''.1$ to block the light from the central star (this corresponds to the area within which the pixels were saturated during observations). We then analysed the data with a range of PC values: PC ranging from 1 to 100 plus PC as a fixed fraction of the total number of frames: 1, 2, 5, 10, 20, 30 and 50%. The images are corrected for the true North offset for LMIRCam of $-0.430^\circ \pm 0.076^\circ$ (Maire et al. 2015).

All the reduced images were inspected by eye, making use of the simultaneous and semi-independent observations with the two mirrors to distinguish between real companion candidates and persistent speckles. An example of the final pca-reduced image for one of the targets is shown in Figure 4.2 for a representative PC number of 20, for both mirrors. A close-in companion-like feature is visible North of the star in the DX mirror image and its position is indicated with a black arrow in both mirrors; however, comparison with the SX mirror image of the same target reveals no such feature at the same location, thus suggesting that it is a non-physical object, likely a bright speckle.

The final pca-reduced images for all targets and both mirrors (where applicable) are shown in Appendix C, in Figures C.3, C.4 and C.5, for a representative PC number of 20. All the images were inspected by eye and no new companion candidates were detected. Four of our targets have confirmed planetary companions detected with the RV method, with masses between ~ 0.3 to $\sim 16 M_J$. These objects are however too close to their host star to be detected in our DI survey, with most of them having an angular separations of $\leq 0''.10$. The most DI-favourable companion would be the candidate around HD 113337, at an angular separation of $\sim 0''.13$, but its mass of $\sim 16 M_J$ is below our achieved detection limits for this target (see Table C.1). One of our targets, HD 206860, has a companion detected via direct imaging but its large angular separation of $\sim 44''$ falls outside the field of view for our observations.

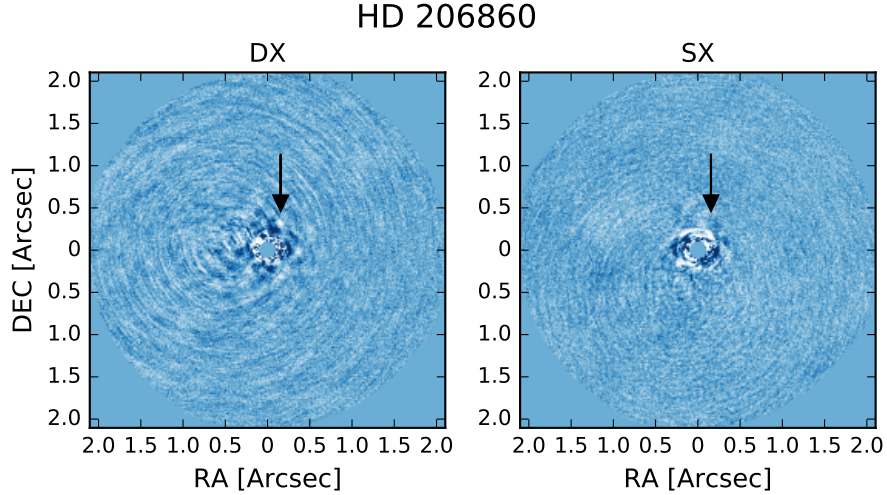


Figure 4.2: ADI reduced images of HD 206860 for both mirrors, for a representative PC number of 20. The images are oriented with North up, and the colormap has been chosen to better visualise the data. The black arrow marks the position of a suspicious feature in the DX image, ruled out as a speckle thanks to the comparison with the SX image.

4.4.3 Contrast curves & Mass limits

We evaluated the contrast limits at various separations for each target and for each mirror using the dedicated contrast curve module in PynPoint. This package uses the unsaturated PSF of the central star to create and inject fake negative planets with varying magnitude contrast at the desired separations and azimuthal angles, and creates contrast curves given the desired σ level and/or false positive fraction (FPF), corrected for small sample statistic according to [Mawet et al. \(2014\)](#). The package allows to account for the possible presence of a neutral density filter, which is the case for some of our targets (see Table 4.3). The other main free parameters is the aperture radius, which we fixed at 1 FWHM ($\sim 0''.116$).

The contrast curves are sampled between $0''.2$ and $1''.9$ in steps of $0''.1$, and between 0° and 360° in steps of 45° , with thresholds of 1, 2, 3 and 5σ .

The resulting 5σ contrast curves for all the targets (and for both mirrors, if applicable) are shown in Figure 4.3, where the grey shaded area represents the uncertainty on the magnitude contrast derived as variance of the all the contrasts at various azimuthal angles for a given separation. We achieve a median contrast of ~ 4.5 mag at an angular separation of $0''.2$ from the host star, while far away we are limited by the median background limit and we reach ~ 10.7 mag at $\sim 2''$.

We convert the contrast curves into mass detection limits using the L' -band magnitude, distance, and age for each target (see Table 4.1), together with the BT-Settle evolutionary models ([Allard et al. \(2012\)](#), see also footnote 7 in Section 2). Uncertainties of both the stellar magnitude and the contrast values are taken into account and converted into mass limit uncertainties. The

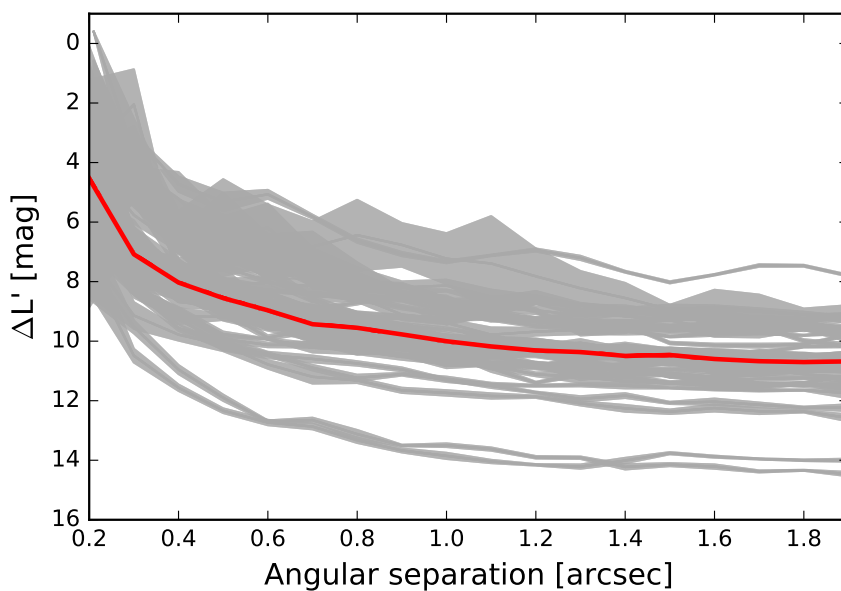


Figure 4.3: Contrast curves (5σ) for all targets and both mirrors, where applicable (grey lines). The grey shaded area around each curve represents the 1σ uncertainty range. The thick red line shows the median of all contrast curves.

achieved contrast and mass limits for all the targets are reported in Table C.1. If a target was observed with both mirrors, we report only the values derived from the better performing mirror.

We then used these mass detection limits to evaluate the detection space for our survey with an approach similar to what done in [Launhardt et al. \(2020\)](#): we run Monte-Carlo (MC) simulations in which we assign a companion to each target, randomising its mass, semi-major axis, orbit inclination and orbital phase. The semi-major axis and mass are drawn from log uniform probability distributions with boundaries of $[10^{0.05}, 10^{3.25}]$ au and $[10^{-1.05}, 10^{2.05}] M_J$. The eccentricity is set to zero, and the inclination is drawn so that all disc orientations in a 3D space are equally probable. For those planets for which we have information about the inclination of the disc (see Table 4.2), we assume co-planarity for the simulated companions and we draw the inclination given the known constraints.

For each simulated planet we then verify if it would have been detected by our survey, given our achieved mass limits. We generated 10^7 simulated planets per star, and estimated the error as the standard error on the weighted mean of 100 sets of 10^5 companions. The resulting detection probability map is shown in Figure 4.4. We achieved a detection probability of $> 50\%$ for companions more massive than $\sim 30 M_J$ between ~ 30 and ~ 100 au.

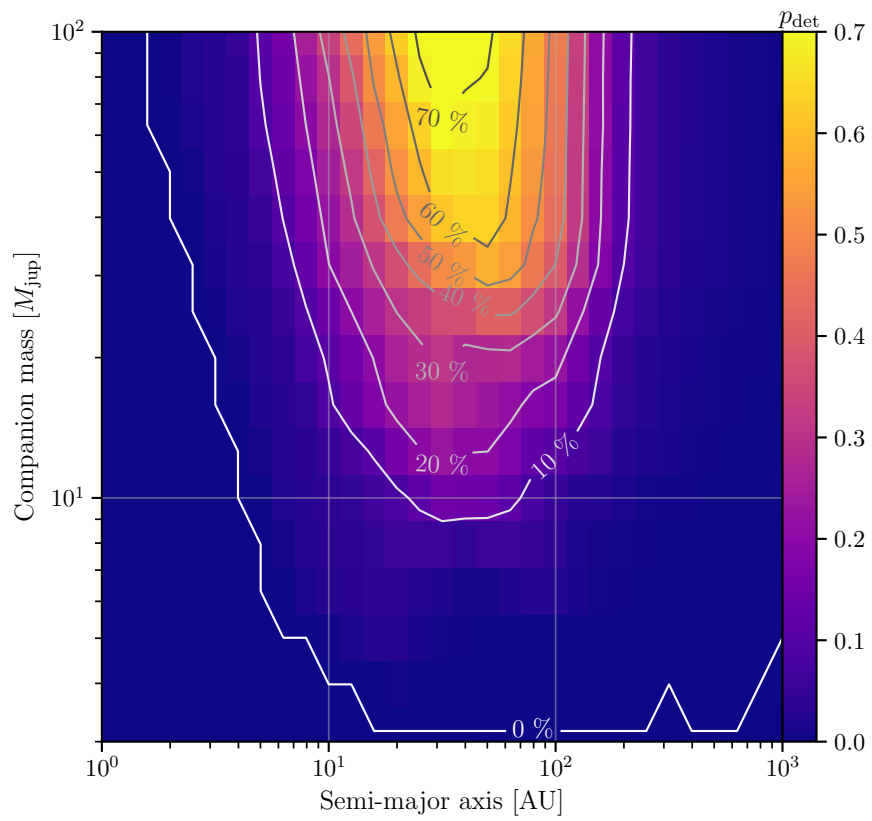


Figure 4.4: Survey detection probability as a function of companion mass and true (not projected) semi-major axis.

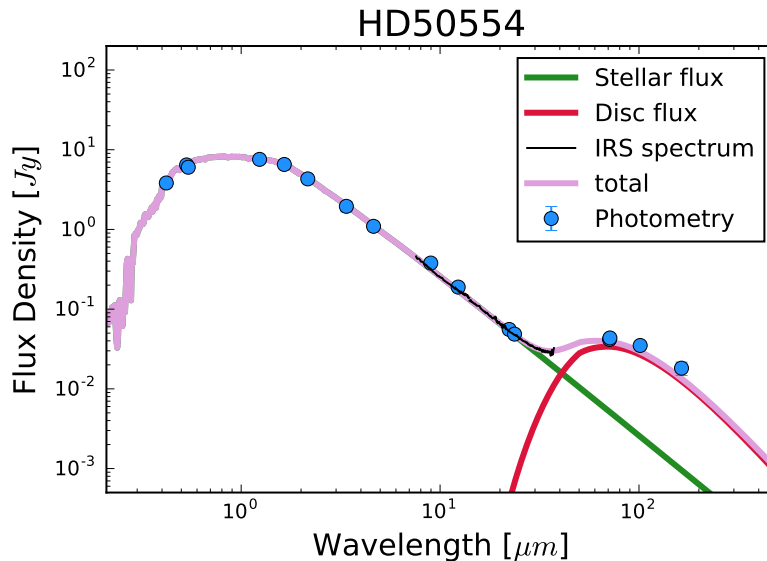


Figure 4.5: Flux density distribution of HD 50554. The blue points are the photometric datapoints found in the literature, the black line is the IRS spectrum, while the green and red lines are the fitted stellar and disc fluxes, respectively.

4.4.4 Infrared excess characterisation

All of our targets were pre-selected due to their infrared excess $L_{\text{disc}}/L_{\star}$, which hints at the presence of a debris disc. To better constraint the target parameters such as stellar luminosity and effective temperature, as well as debris disc dust temperature, fractional luminosity and blackbody radius, we fit the spectral energy distribution (SED) for each target.

The fit is the same as in Section 2.2: we simultaneously fit a stellar atmosphere (PHOENIX; [Husser et al. 2013](#)) plus a single or double black-body model to the observed photometry and the Spitzer IRS spectrum. The photometry is compiled from various archives and covers a wide range of filters and wavelengths, including: "Heritage" Stromgren and UVB ([Paunzen 2015](#)), 2MASS ([Skrutskie et al. 2006](#)), Hipparcos/Tycho-2 (ESA, 1997, The Hipparcos and Tycho Catalogues, ESA SP-1200, [Esa 1997](#)), AKARI ([Ishihara et al. 2010](#)), WISE ([Wright et al. 2010](#)), and Spitzer ([Chen et al. 2014](#)). The fitting method finds the best-fitting model with the MultiNest code ([Feroz et al. 2009](#)), using synthetic photometry of grids of models. An example of such a fit is shown in Figure 4.5.

For 18 of our targets, the best fit is obtained with a stellar model plus a one-temperature BB model. Four targets are better fit with two BB components, one for the outer cold belts, and one for an additional inner warm belt. For two targets, the infrared excess turned out to be not significant and their SEDs are better fit with only the stellar model. The SED fits for all 24 LStEN targets is shown in Figure C.2. We point out that a single-belt fit does not exclude the

Table 4.4: Disc parameters from SED fitting

Target	L_{\star} [L_{\odot}]	T_{\star} [K]	R_{\star} [R_{\odot}]	SED fit					
				$L_{\text{disc},1}/L_{\star}$ ($\times 10^{-5}$)	$T_{\text{dust},1}$ K	$R_{\text{BB},1}$ [au]	$L_{\text{disc},2}/L_{\star}$ ($\times 10^{-5}$)	$T_{\text{dust},2}$ K	$R_{\text{BB},2}$ [au]
HD 206860	1.147 ± 0.006	6000 ± 20	0.991 ± 0.006	0.82 ± 0.07	84.0 ± 5.0	40 ± 2.1	—	—	—
HD 183324	14.9 ± 0.3	8530 ± 50	1.76 ± 0.02	1.2 ± 0.1	69.0 ± 3.0	154 ± 16	1.00 ± 0.08	154.0 ± 12.0	13.0 ± 2.0
HD 220825	23.0 ± 1.0	9600 ± 100	1.74 ± 0.03	2 ± 0.2	167.0 ± 4.0	27.6 ± 3.3	—	—	—
HD 184930	1400 ± 300	11700 ± 200	9.0 ± 0.9	—	—	—	—	—	—
HD 221853	3.93 ± 0.03	6730 ± 30	1.46 ± 0.01	80 ± 1	89.2 ± 0.4	77.2 ± 3.3	—	—	—
HD 127821	2.95 ± 0.02	6590 ± 20	1.321 ± 0.01	19.3 ± 0.6	42.0 ± 3.0	280 ± 21	—	—	—
HD 191174	18.9 ± 1.0	8800 ± 100	1.88 ± 0.03	2.1 ± 0.2	71.0 ± 3.0	151 ± 18	4.5 ± 0.5	300.0 ± 20.0	3.8 ± 0.5
HD 110897	1.114 ± 0.006	5890 ± 20	1.013 ± 0.007	2.2 ± 0.1	50.0 ± 4.0	128 ± 9.4	—	—	—
HD 128311	0.288 ± 0.002	4843 ± 9	0.762 ± 0.003	2.5 ± 0.2	33.0 ± 8.0	160 ± 24	—	—	—
HD 152598	5.05 ± 0.04	7070 ± 20	1.5 ± 0.01	2.9 ± 0.1	129.0 ± 4.0	39.1 ± 2.3	—	—	—
HD 182919	32.0 ± 0.8	9900 ± 70	1.90 ± 0.02	2.3 ± 0.1	183.0 ± 6.0	23.9 ± 3.1	—	—	—
HD 116956	0.524 ± 0.003	5350 ± 10	0.842 ± 0.005	—	—	—	—	—	—
HD 161868	27.0 ± 1.0	9190 ± 90	2.05 ± 0.04	5.3 ± 0.5	46.0 ± 2.0	368 ± 55	3.4 ± 0.4	118.0 ± 7.0	29.0 ± 3.0
HD 192425	22.4 ± 0.5	8970 ± 50	1.96 ± 0.03	3.6 ± 0.1	58.0 ± 2.0	231 ± 25	2.6 ± 0.1	210.0 ± 6.0	8.3 ± 0.5
HD 50554	1.5 ± 0.01	6000 ± 20	1.133 ± 0.009	4 ± 0.1	53.0 ± 6.0	132 ± 12.1	—	—	—
HD 219498	0.7 ± 0.01	5500 ± 20	0.91 ± 0.01	19 ± 3	76.0 ± 3.0	44 ± 2.1	—	—	—
HD 205811	25.6 ± 0.7	9330 ± 70	1.93 ± 0.02	1.5 ± 0.1	148.0 ± 10.0	35.6 ± 5.2	—	—	—
HD 32977	23.0 ± 0.5	8400 ± 40	2.25 ± 0.03	2.75 ± 0.1	146.0 ± 4.0	35.9 ± 4.1	—	—	—
HD 8907	1.97 ± 0.01	6250 ± 20	1.198 ± 0.008	24.8 ± 0.8	43.0 ± 3.0	236 ± 16	—	—	—
HD 48682	1.86 ± 0.02	6015 ± 16	1.26 ± 0.01	5.9 ± 0.1	56.5 ± 0.6	132 ± 4.1	—	—	—
HD 212695	3.13 ± 0.02	6510 ± 20	1.395 ± 0.009	6.2 ± 0.7	40.0 ± 5.0	320 ± 33	—	—	—
HD 113337	4.12 ± 0.03	6690 ± 20	1.509 ± 0.008	9.2 ± 0.3	54.3 ± 0.7	212 ± 9.6	—	—	—
HD 143894	26.2 ± 0.7	8670 ± 50	2.27 ± 0.02	2.9 ± 0.3	56.0 ± 2.0	247 ± 30	—	—	—
HIP 83043	0.0452 ± 0.0003	3600 ± 10	0.547 ± 0.004	6 ± 2	44.0 ± 14.0	32 ± 5.8	—	—	—

Stellar and disc parameters derived via SED fitting. The outer and colder belt’s radius $R_{\text{BB},1}$ has been corrected for the blowout grain size according to Pawellek (2016), while the inner and warmer belt size $R_{\text{BB},2}$ is simply the black body radius from SED fitting, without correction.

presence of a second belt: it is simply a reflection on the amount of datapoints available for the fit.

Correcting for the blowout grain size (see Section 2.2), we estimate the ‘true’ disc sizes for the cold belt of all of our targets. This cannot be applied to the warm belt, since the underlying grain physics for those temperatures is not yet fully understood. The stellar and disc parameters (corrected for blowout grain size in the case of the outer belt) for all of our DD targets are summarised in Table 4.4.

4.5 Planetary constraints and disc analysis

In this Section, we derive constraints on the presence of companions around our targets, using the mass detection limits derived in Section 4.4.3, the disc information, and the constraints from the proper motion of the host stars (where applicable).

4.5.1 Self-stirring analysis

Of the 22 debris disc-hosting targets in our survey, 18 are better explained with a single-belt model and 4 can be explained with a double-belt model; moreover, all the double-belt systems and 10 out of the 18 single belt ones also have a resolved disc size.

We can test the hypothesis that these systems are completely self-stirred (see Section 2.5), and thus they do not require the presence of a planet to explain the presence of collisionally generated dust at the observed radii. Following the work from [Krivov & Booth \(2018\)](#), the self-stirring timescale can be expressed as a function of the disc's and host star's parameters, as:

$$T_{\text{stir}} = \frac{129 \text{ Myr}}{x_m} \times \left(\frac{1}{\gamma} \right) \left(\frac{\rho}{1 \text{ g cm}^{-3}} \right)^{-1} \left(\frac{v_{\text{frag}}}{30 \text{ m s}^{-1}} \right)^4 \left(\frac{S_{\text{max}}}{200 \text{ km}} \right)^{-3} \times \left(\frac{M_{\star}}{M_{\odot}} \right)^{-3/2} \left(\frac{a}{100 \text{ AU}} \right) \quad (4.1)$$

Where x_m is a dimensionless parameter proportional to the disc's mass, γ has a value between 1 and 2 and encapsulate the eccentricity behaviour of the planetesimals, ρ is the bulk density of the planetesimals and S_{max} their maximum size. v_{frag} is the relative fragmentation velocity above which planetesimals would undergo destructive collisions and thus ignite a collisional cascade through the disc.

We can now compare T_{stir} with the age of the observed systems as a function of disc radius (a), for a given stellar mass M_{\star} . We fixed the following parameters to the standard values used in [Krivov & Booth 2018](#): $\gamma = 1.5$, $\rho = 1 \text{ g cm}^{-3}$, $v_{\text{frag}} = 30 \text{ ms}^{-1}$ and $S_{\text{max}} = 200 \text{ km}$. The results for all the single-belt systems in our survey are shown in Figure 4.6, where the shaded blue area encompasses two representative values for x_m of 1 (dashed line) and 10 (full line). Regarding the double-belt systems, we test the self-stirring assumption on the outer belt only, and the results are shown in Figure 4.7.

[Kenyon & Bromley \(2008\)](#) originally found consistently longer stirring timescales for a slightly different self-stirring scenario, deriving an analytical formula for the stirring timescale of:

$$T_{\text{stir}} = \frac{801 \text{ Myr}}{x_m^{1.15}} \left(\frac{M_{\star}}{M_{\odot}} \right)^{-3/2} \left(\frac{a}{100 \text{ au}} \right)^3 \quad (4.2)$$

For comparison, we show the analysis from [Kenyon & Bromley \(2008\)](#) as a red shaded area in Figures 4.6 and 4.7, again for representative x_m values of 1 (dashed line) and 10 (full line).

The main difference between the two studies resides in the initial size of planetesimal after the dispersal of protoplanetary discs. [Kenyon & Bromley \(2008\)](#) assumes that planetesimals are born with sizes below 1 km, and finds that only by the time these planetesimals grow to Pluto-sized bodies (i.e: $\sim 1000 \text{ km}$), they are able to quickly self-stir the disc. [Krivov & Booth \(2018\)](#) instead argues that bodies as small as $\sim 200 \text{ km}$ can already excite planetesimals to the point of destructive collisions.

In Figures 4.6 and 4.7 we also plot the ages and disc sizes for all of our targets, both SED-derived (in black), and resolved disc sizes (in red). As can be seen for all of our targets, the disc size

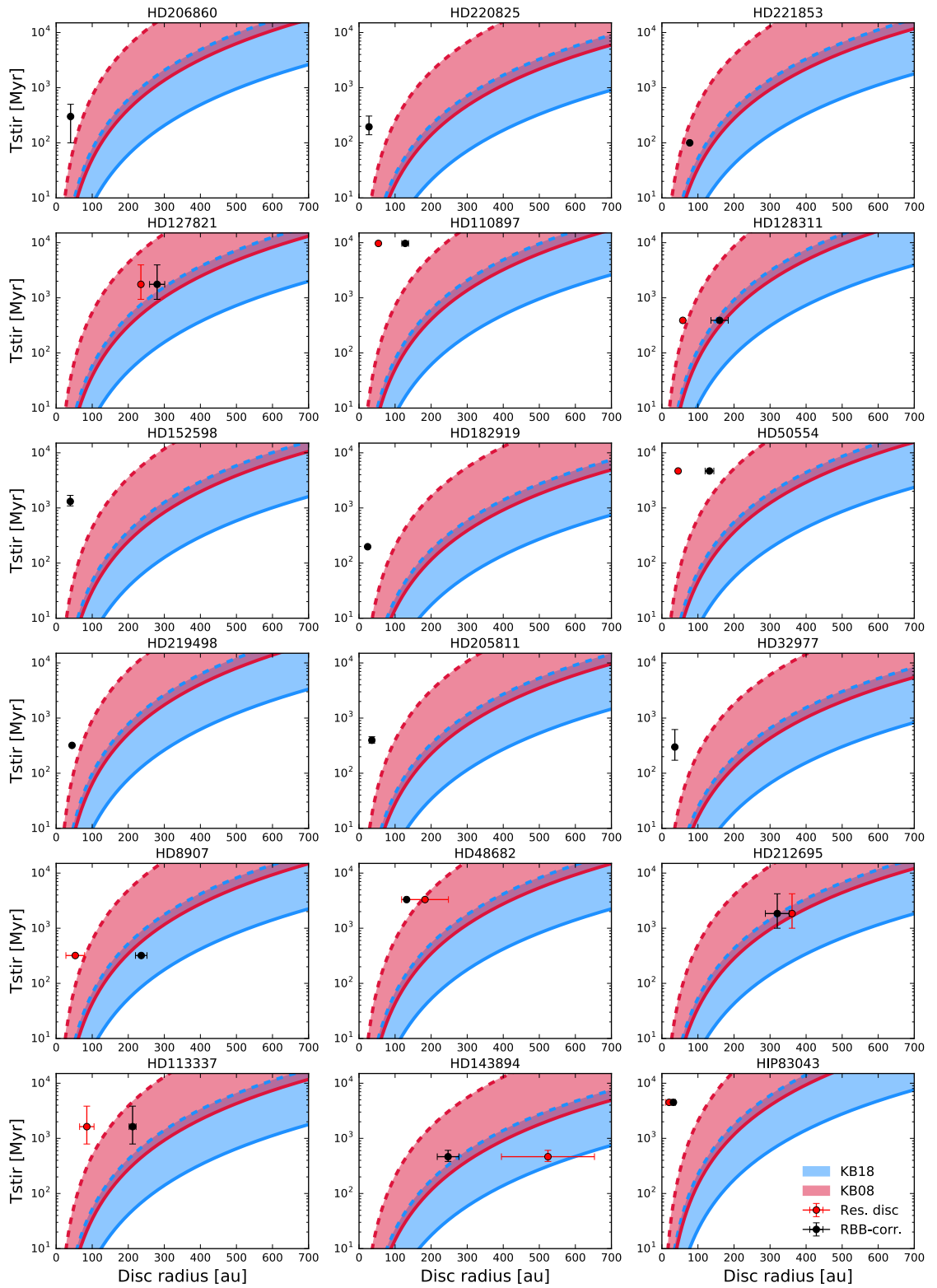


Figure 4.6: Self-stirring analysis for the single belt debris discs systems. The blue shaded area is the stirring timescale as a function of semi-major axis, according to [Krivov & Booth \(2018\)](#) (KB18), while the red shaded area is derived according to [Kenyon & Bromley \(2008\)](#) (KB08). In both cases, the analysis encompasses two representative x_m values of 1 (dashed lines) and 10 (full lines). The red and black point represents the resolved and SED-inferred disc sizes, respectively.

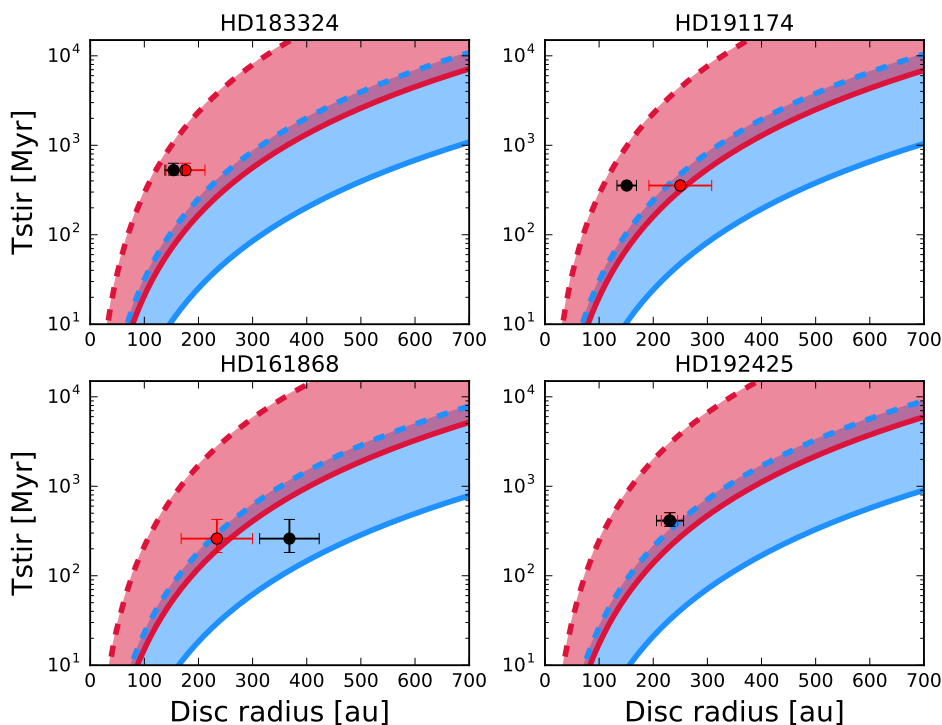


Figure 4.7: Self-stirring analysis for the double belts debris discs systems. The analysis is done on the outer belt only, and the legend is the same as in Figure 4.6.

is smaller than the maximum disc size explainable with self-stirring only, thus confirming that all of these systems can be explained via self-stirring. We point out that this does not exclude that planetary-stirring is in action, nor it excludes the presence of unseen planets, but it merely implies that a companion is not necessary to explain the observed disc sizes. We also point out that these results rely on accurate ages and disc sizes measurements, and any future improvement in this regard might help to confirm (or deny) the self-stirring hypothesis.

4.5.2 Double-belt analysis

Four of our targets are double-belt systems, for which the colder and outer belt has been resolved through imaging (see Table 4.2). The presence of a wide gap between the two belts can be explained as the carving action of one (or in most cases, more) planet(s) clearing its orbit, and the radius and width of this gap can therefore be related to the minimum planetary mass and minimum number of planets of that given mass required to carve such a gap (see Figure 4.8).

[Shannon et al. \(2016\)](#) carried out such an analysis employing N-body simulations to study the clearing times for various planetary systems, assuming assuming orbital separations of 20 mutual Hill radii between the planets (according to similar results obtained by [Fang & Margot 2013](#)) and a density for all planets of $\rho = 4 \text{ g cm}^{-3}$. They assigned randomly and linearly distributed

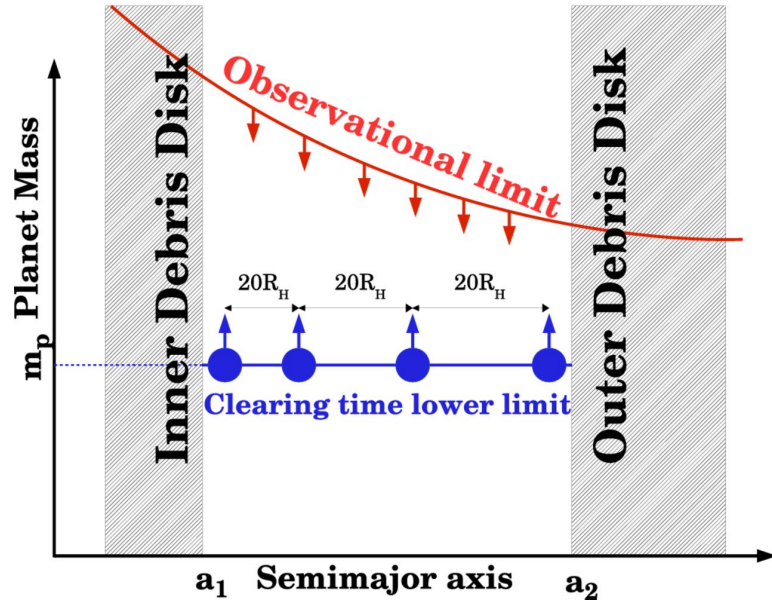


Figure 4.8: Visualisation of the minimal planetary system that can carve a gap between a_1 and a_2 , assuming that all the planets have the same mass m_p and have a typical separation of $20 R_H$. Figure originally published in [Shannon et al. \(2016\)](#).

eccentricities and inclinations between $e = 0$ and $e = 0.02$, and $i = 0^\circ$ and $i = 2^\circ$, respectively. They fit the simulation results and inverted the relation to derive analytical expressions for the minimum planetary mass m_p and minimum number of planets N as a function of the inner belt's outer edge a_1 and the outer belt's inner edge a_2 :

$$m_p = \left(\frac{4 \text{ Myr}}{\tau} \right) \times \left(\frac{a_2}{\text{au}} \right)^{3/2} \times \left(\frac{M_\star}{M_\odot} \right)^{1/2} m_\oplus \quad (4.3)$$

$$N = 1 + \frac{\log \left(\frac{a_2}{a_1} \right)}{\log \left(\frac{1 + 0.13 \left(\frac{m_p}{m_\oplus} \right)^{1/3} \left(\frac{M_\odot}{M_\star} \right)^{1/3}}{1 - 0.13 \left(\frac{m_p}{m_\oplus} \right)^{1/3} \left(\frac{M_\odot}{M_\star} \right)^{1/3}} \right)} \quad (4.4)$$

With M_\star being the stellar mass and τ being the system's age.

We applied these equations to our four double-belt targets and for each of them derived a minimal planetary system required to explain the size and radial extent of the gap. The inner belt was derived via SED fitting and its uncertainty represents the precision with which the fit was carried out, rather than being a measurement of the physical extent of the belt; for this reason, we approximate the outer edge of the inner belt a_1 as the SED-fit black body radius derived in

Table 4.5: Minimal planetary system parameters

Target	a_1 [au]	a_2 [au]	m_p [M_\oplus]	N
HD 183324	13.0	176.0	24.7	5.2
HD 191174	3.8	250.0	63.0	5.8
HD 161868	29.0	234.0	85.6	3.3
HD 192425	8.3	230.0	50.1	5.3

Minimum mass and number of planets required to explain the disc's gap position and extent.

Section 4.4.4. Similarly, we approximate the inner edge of the outer belt with the position of the inner belt derived from resolved images.

The results for the four double-belt targets are summarised in Table 4.5. The gap around HD 183324 can be explained with a minimal planetary system of 6 planets (to allow for a non-fractional number of planets), each with a mass of $\sim 20 M_\oplus$. For HD 191174 and HD 192425, the minimum mass required is higher, with a minimum number of 6 planets with masses of $\sim 60 M_\oplus$ for HD 191174, and 4 planets with masses of $\sim 80 M_\oplus$ for HD 192425. Finally, the minimal planetary system required to explain the gap in the disc around HD161868 consists of 4 planets, each with a mass of $\sim 50 M_\oplus$.

These masses are several orders of magnitudes lower than the minimum mass limits achieved with our contrast curves (see Section 4.4.3), and therefore the allowed parameter space for each planetary system, given the disc and host star's constraints, is still fairly large.

4.5.3 Planetary constraints from proper motion anomaly

A binary system composed of a low mass companion and a primary star will have a displacement between the photocentre of the system and the barycentre. This is due to the fact that the secondary companion will shift the centre of mass away from the primary, while the photocentre will remain close to the geometrical centre of the primary (since the luminosity of a low-mass companion is negligible with respect to the luminosity of the primary). As a result, in an unresolved binary system for which $m_2 \ll m_1$, the photocentre will appear to revolve around the centre of mass. Depending on where the photocentre appears to be on this virtual orbit, its observed proper motion will vary in time.

[Kervella et al. \(2019\)](#) defined the proper motion anomaly (PMA) vector $\Delta\mu_{G2}$ as the difference between the proper motion vector in the Gaia DR2 catalogue μ_{G2} minus the long-term mean proper motion vector μ_{HG} , derived as difference in the astrometric position of the star between the Hipparcos ([Esa 1997](#)) and the GAIA DR2 catalog ([Gaia Collaboration et al. 2018](#)). A visualisation of the PMA vector is shown in Figure 4.9.

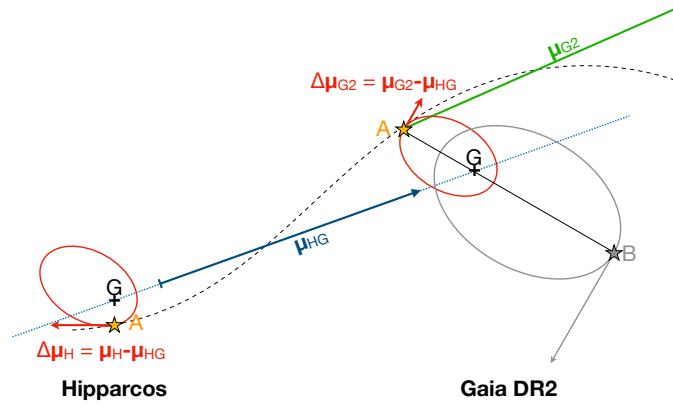


Figure 4.9: Figure originally published in [Kervella et al. \(2019\)](#), showing the virtual orbit that the system photocentre follows around the centre of mass, due to the presence of a companion B around the star A.

We refer to the work in [Kervella et al. \(2019\)](#) for a detailed derivation of the following relations, and we simply summarise that, for a target with parallax ϖ and assuming $m_2 \ll m_1$, the mass of the secondary can be expressed as:

$$m_2(r) = \frac{\sqrt{r}}{\gamma [P(r)/\delta t]} \sqrt{\frac{m_1}{G}} \frac{\Delta v_{T,G2}}{\eta \zeta}$$

Where r is the secondary's orbital radius, m_1 is the mass of the primary, G is the gravitational constant and $\Delta v_{T,G2}$ is the norm of the linear tangential velocity of the PMA vector, expressed as:

$$\Delta v_{T,G2} = \frac{\sqrt{\Delta \mu_{G2,RA}^2 + \Delta \mu_{G2,DEC}^2}}{\varpi} \times 4740.470$$

The proper motion measurement in the GDR2 catalog is not an instantaneous measurement, but it is derived from a series of observations over a period of time δt of 668 days ([Gaia Collaboration et al. 2018](#)). The measured PMA is then a time average over this time window, and the norm of the PMA is affected by observing window smearing depending on the ratio between the orbital period of the system $P(r)$ and the observing time δt . This is accounted for using the γ factor, defined as:

$$\gamma(P(r)/\delta t) = \frac{P(r)/\delta t}{\sqrt{2}\pi} \sqrt{1 - \cos \frac{2\pi}{P(r)/\delta t}}$$

The possible inclination and position angle of the orbit can be approximated with the disc's information (see Table 4.2) assuming a co-planar orbit. Thus, it is possible to deproject the PMa vector and evaluate the ratio η between the measured 2D PM vector projected onto the sky plane and the 'real' 3D orbital PM vector. Normalising the observed PMa by η allows to estimate the deprojected distribution of the companion mass.

If the orbital period of the system is longer than the baseline time δt_{HG} used for the determination of the long-term PM vector μ_{HG} (i.e: the time difference between the Hipparcos and GAIA DR2 epochs), then the PMa is biased. This bias is taken into account with the ζ function, defined as:

$$\zeta\left(\frac{P}{\delta t_{\text{HG}}}\right) = \left| \frac{\mu_{\text{G2}} - \mu_{\text{HG}}}{\mu_{\text{orb}}} \right|$$

with P being the orbital period, and with $\delta t_{\text{HG}} \simeq 24.25$ years. Since no information on the orbital period is available, this is computed for every radial separation. [Kervella et al. \(2019\)](#) computed the proper motion anomaly for all the stars common to both the Hipparcos and the GAIA DR2 catalogue, and suggested that a PMa SNR value > 3 is an indicator of the presence of a companion.

There are three targets in our survey that fit in this category: HD 161868, HD 8907 and HD 113337. Using the mass information from Table 4.1, the disc's inclination and position angles from Table 4.2, together with the parallaxes from GAIA DR2 and the PMa RA and DEC values from [Kervella et al. \(2019\)](#) (see Table 4.6), we computed the combinations of secondary mass and orbital radius that would explain the observed PMa. In Figures 4.10, 4.11 and 4.12, we show these (m_2, r) combinations (red line), with the respective 1, 2 and 3σ uncertainties (progressively darker red shaded areas). We compared these possible companions with our achieved contrast curves, shown with a solid black line for the 5σ curve, together with the 3σ (dashed black line) and 1σ (dotted black line) curves. We also plot the position and extension of the resolved disc (blue dotted line and shaded area). The double-belt system HD 161868 is the only target for which only the inner belt is visible in the field of view, and for this reason the dashed blue line in Figure 4.10 represents the position of the inner belt, and not the resolved one (marked with a blue arrow), while the blue shaded area represents the uncertainties on the inner belt's position and not its physical extent.

Table 4.6: Proper Motion anomaly values

Target	$\Delta\mu_{G2,RA}$	$\Delta\mu_{G2,DEC}$	Δ_{G2}
HD161868	1.241 ± 1.113	4.377 ± 1.030	3.0
HD8907	-0.427 ± 0.091	-0.034 ± 0.106	3.06
HD113337	-0.673 ± 0.080	0.454 ± 0.076	7.36

Proper Motion anomalies values and PMA SNR Δ_{G2} are from [Kervella et al. \(2019\)](#)

As visible in Figure 4.10, the mass limits achieved for HD 161868 allow to exclude the presence of planets more massive than few tens of M_J beyond ~ 20 au, as well as reasonably excluding objects more massive than $100 M_J$ between 10 and 20 au. Together with the presence of a disc at ~ 30 au, we can exclude the presence of planets massive enough to be responsible for the observed PMA at those radial separation. Moreover, there are no known massive companions further away that could explain the PMA (two candidate companions were detected at $\sim 6''1$ and $\sim 7''2$ by [Janson et al. \(2013\)](#), but they were ruled out as background stars). The minimal planetary system that could explain the disc's gap (see Section 4.5.2) would also not be massive enough to explain the PMA. We then suggest that the observed anomaly can be explained by either a very close-in (< 2 au) unknown stellar companion, or by a currently undetected low-mass stellar companion with an orbital radius between 2 and 10 au, and a mass of $\geq 100 M_J$.

Regarding HD 8907 (Figure 4.11), our imaging observations can reasonably exclude the presence of companions more massive than $\sim 10 M_J$ beyond ~ 15 au, while the resolved disc's information can exclude the presence of companions between ~ 30 and ~ 80 au. We did not find any known further away companion in the literature, and we therefore suggest that the observed anomaly could be caused by a currently undetected planetary companions with an orbital radius < 15 au and a mass of $\sim 10 M_J$. The observed PMA could also be explained by a currently unknown stellar companion at certain given separations (for example at ~ 0.8 , ~ 1 and ~ 1.5 au, see Figure 4.11).

Finally, we discuss the case of HD 113337, shown in Figure 4.12. The presence of a resolved disc combined with our achieved mass detection limits allow to exclude companions more massive than $\sim 30 M_J$ beyond 20 au. HD 113337 has a known far away M3.5 dwarf companion at $\sim 200''$ (according to the Washington Double Star catalog, see [Mason et al. 2014](#)), but this, nor the close-in companion at ~ 1 au, are massive enough to explain the observed anomaly. The companion candidate at ~ 5 au (detected via RV, see [Borgniet et al. 2019b](#)) would have a mass compatible with the observed proper motion anomaly; we suggest that this finding points towards the confirmation of the RV signal and the presence of an additional planet in this system.

Additional RV observations for all of these three targets might help to shed light on these systems, particularly in the framework of excluding (or detecting) very close-in stellar mass companions, thus helping to shrink the parameter space.

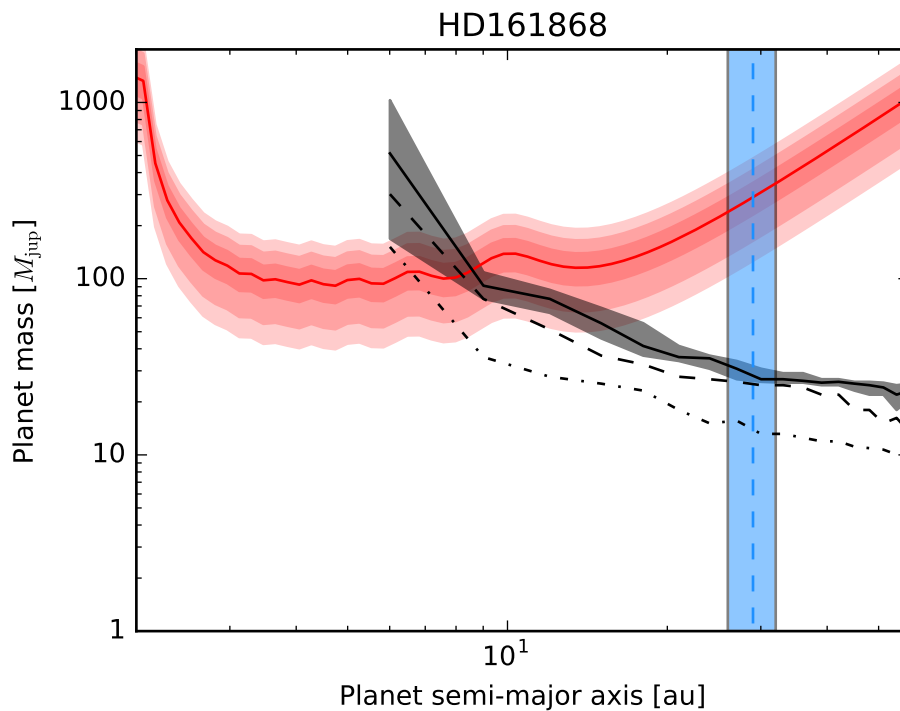


Figure 4.10: Proper Motion anomaly analysis from [Kervella et al. \(2019\)](#) for HD 161868. The red line is the relation between companion's mass (in Jupiter masses) and orbital radius (in au) that can explain the observed PMA, and the red shaded areas (progressively darker) are the 1σ , 2σ and 3σ uncertainties. The black solid line and black shaded area is the achieved 5σ mass detection limits from the LStEN observations, together with the 3σ (dashed line) and 1σ (dotted line). The blue dashed line and shaded area represents the position and uncertainty of the inner belt derived via SED fitting. The position of the resolved, outer belt of HD 161868 is not visible in the field of view, and it is marked with a blue arrow.

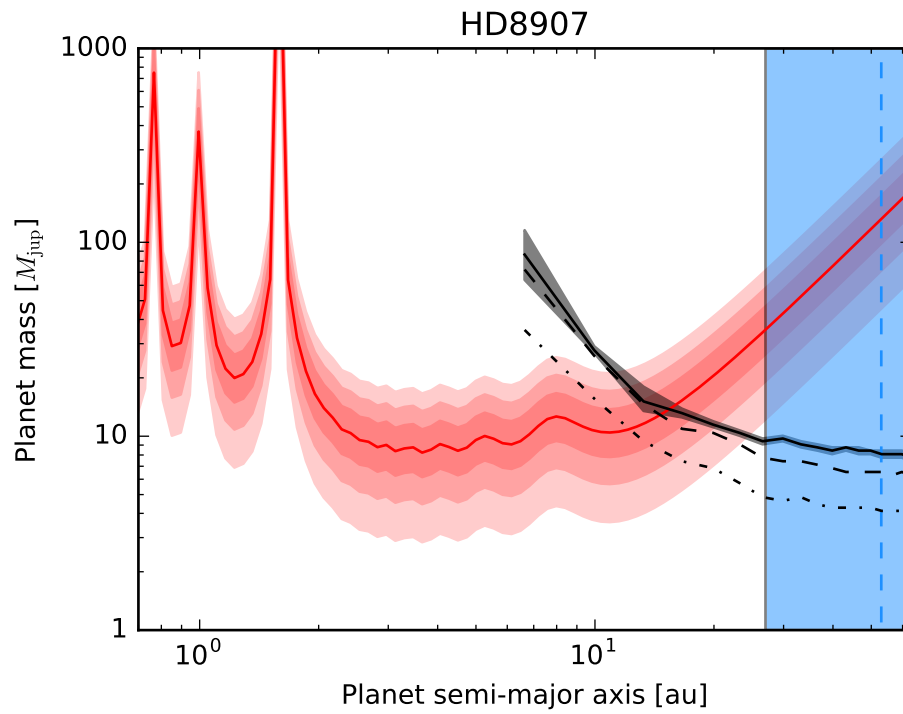


Figure 4.11: As in Figure 4.10. The blue dashed line and shaded area represents the resolved disc position and extent for HD 8907.

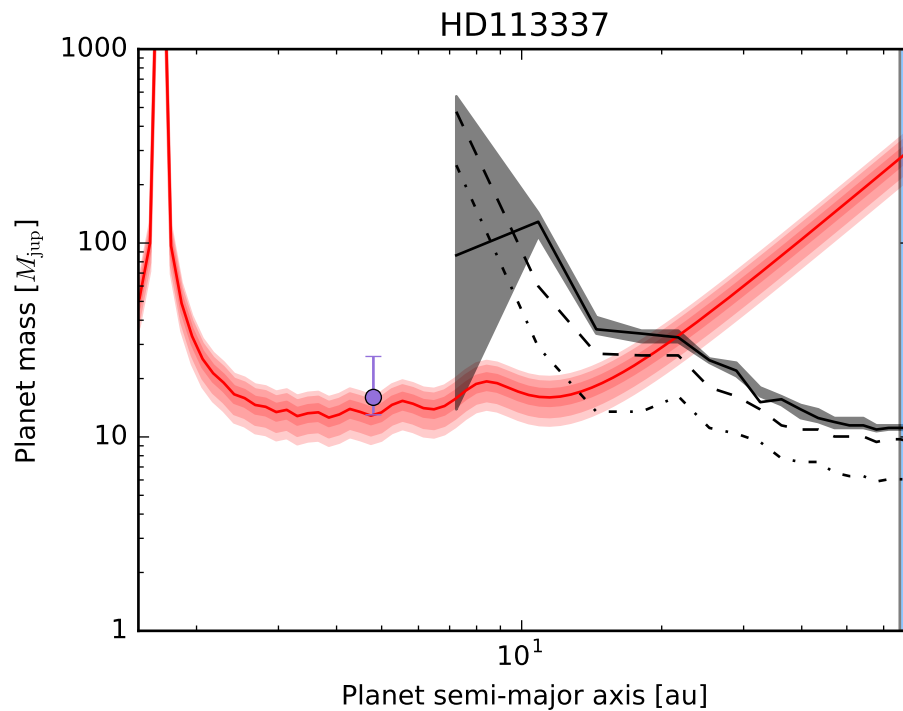


Figure 4.12: As in Figure 4.10. The blue dashed line and shaded area represents the resolved disc position and extent for HD 113337. The purple point and errorbars mark the position and mass of the outermost, confirmed, RV planet orbiting the star (see Table 4.2)

4.6 Conclusions

In this Chapter we presented the L^IStEN survey in terms of its scientific goals, target selection, observations, data reduction and data analysis. The goal of the survey is to detect and characterise the population of giant planets around circumstellar disc hosting targets, with a focus on investigating companion-disc interactions. The survey is designed to be the extension of the ISPY survey in the northern hemisphere. To this end, we selected nearby stars with signs of a circumstellar disc (either inferred via SED fitting or with a resolved disc image), and we prioritised those for which the disc has been imaged, and those with known planetary companions. We ended up with a flexible master list from which we drew our targets depending on the allocated observing nights.

We observed 29 targets between Autumn 2017 and Spring 2019: 18 single-belt DD targets, 4 double-belt systems, 5 PPD ones and 2 for which the IR excess is non-significant. In this Chapter we focused on the 22 DD's only, and we refer to the incoming L^IStEN paper for the analysis of the 5 PPD ones ([Musso Barucci in prep.](#)). Out of these 22 DD targets, 14 have a resolved disc image and 5 have known companions (4 targets have companions discovered via RV observations, and 1 target has a known imaged companion).

All the targets were observed in ADI dual mirror mode with the LMIRCam instrument at LBT, observing each star through meridian passage with the goal of obtaining a minimum rotation field of 60° . During the data reduction and analysis we kept the data from the two mirrors separated, taking advantage of these semi-independent simultaneous observations to distinguish between speckles and physical candidates during the data inspection phase. All the data were reduced with our own semi-automated pipeline, and analysed with the PynPoint package. No new companion candidate was detected.

We produced 5σ contrast curves for all the targets, reaching a median contrast of ~ 5 mag at $0''.2$ and ~ 10 mag at separations $> 1''.5$. We evaluated the detection space for the survey converting the contrast curves into mass limits using known evolutionary models, and then we ran MC simulations of 10^7 planets per star, with randomised masses and orbital parameters, assessing which planet would have been discovered given the achieved mass limits. We have a detection probability greater than 50% for companions with masses $\geq 30 M_J$ between 30 and 100 au.

We used our achieved mass limits and the discs information to place constraints on the presence of undetected planets around each target. Following the work from [Krivov & Booth \(2018\)](#), we tested the hypothesis that self-stirring alone can explain the size of the discs, and we found out that this is true for all the targets (for the 4 double-belt systems we tested this hypothesis on the outer belt). However, we point out that self-stirring models are very dependent on the age of the system, which is often a non-straightforward parameter to derive and can have significant uncertainties. Moreover, for 8 targets the only information on the disc come from SED fitting.

Obtaining resolved images of these discs, as well as better and more coherent constraints on the systems age, will help confirming (or denying) the self-stirring hypothesis.

We then focused on the four double-belt systems, and we used the work from [Shannon et al. \(2016\)](#) to derive the minimal planetary system needed to explain the position and radial extent of the disc around each target. We discovered that the gap in these systems can be explained by the presence of multi-planetary systems (between 4 and 7 planets each) with masses ranging from 18 to $\sim 50 M_{\oplus}$. These masses are several order of magnitudes smaller than what achieved with our mass limits, and given the radial separations and planetary masses involved, current detection methods such as Imaging and radial Velocity cannot at the present time probe this parameter space.

Finally, three targets in our survey show an anomaly in the proper motion between the GAIA DR2 data and the Hipparcos data. Following the work in [Kervella et al. \(2019\)](#), we explored the parameter space of companion mass and semi-major axis that could explain the observed anomaly. Using disc information and our achieved mass limits we were able to constraint the $m_{pl} - a_{pl}$ parameter space, and we made prediction regarding the mass and semi-major axis of currently undetected companions around these systems. Future RV observations and direct imaging follow-ups will be able to test our predictions and shed more light on these interesting systems.

5

Summary and future perspective

5.1 Summary

The direct imaging technique is a powerful technique to detect and observe planetary and low-mass stellar companions in a parameter space complementary to that of other, indirect detection methods. DI can detect giant planets at large separations and in a variety of orbital configurations, and has the advantage of being able to simultaneously image a companion and the circumstellar disc it resides in. Direct imaging surveys like NaCo-ISPY and LStEN, targeting in total hundreds of stars with known and well-characterised circumstellar discs, can help answering specific scientific questions on the occurrence rate and architecture of the giant planet population, and on the complexities of companion-disc interaction. Direct imaging observations at different wavelengths can shed light on various aspects of planet formation and evolution, an example of which is studying the gas accretion phase using $H\alpha$ observations.

In this Thesis I gave an overview of the direct imaging technique, with its main advantages and challenges, and I presented different studies that made use of this technique to address specific scientific questions.

In Chapter 2 I presented the discovery of an M-dwarf companion around the debris disc hosting star HD 193571. The target was observed in the L' band as part of the NaCo-ISPY survey in two different epochs, and additional dedicated observations were carried out in the H band with the

GPI instrument at Gemini South. The companion was detected in all three epochs at a projected separation of ~ 11 au from its host star, and co-motion was confirmed through proper motion analysis. The debris disc around the host star has been inferred through its infrared excess, and SED modelling suggests a size of ~ 120 au. The companion thus appears to reside well within the gap between the disc and the host star, making this only the third low-mass stellar companion discovered within a debris disc. We compared self-stirring and companion-stirring models and concluded that the companion is likely to be the main responsible for the stirring of the disc.

In Chapter 3 I presented $H\alpha$ observations of the known substellar companion orbiting PZ Tel, obtained in angular differential imaging mode with the SPHERE/ZIMPOL instrument at the Very Large Telescope. We detected $H\alpha$ emission from the companion and obtained astrometry and photometry information. Our newly obtained astrometric information extends the available baseline for orbital studies of PZ Tel B up to ~ 12 years, and helps to tighten the uncertainties of the orbital parameters. Using our photometric data we evaluated the $H\alpha$ line flux, and obtained an $H\alpha$ activity $\log_{10}(L_{H\alpha}/L_{bol})$ of -4.16 ± 0.08 and -4.31 ± 0.10 , depending on the estimated bolometric luminosity. This activity is consistent with known average activity levels for M dwarf of the same spectral type. Given the absence of a known gaseous disc and the relatively old age of the system (24 Myr), we concluded that the $H\alpha$ emission around PZ Tel B is likely due to chromospheric activity, rather than gas accretion.

In Chapter 4 I presented the LStEN survey, which is designed to be the extension of the NaCo-ISPY survey in the Northern hemisphere. LStEN is a high-contrast imaging survey that targeted 29 nearby stars with known circumstellar discs (22 debris disc, 5 protoplanetary disc and 2 targets with non-significant IR excess), with the aim of detecting and characterising planetary and low-mass stellar companions. The survey was carried out in the L' filter at the Large Binocular Telescope, using the LMIRCam instrument. In this Chapter I presented the main scientific goals of the survey, as well as its target selection, observational strategy and data reduction. I presented only the data analysis for the 22 DD-hosting targets (plus the two targets with no disc), while the PPD-hosting targets will be presented in an upcoming publication. No new companions were detected, and contrast curves and detection limits were created for all of DD targets, reaching a median contrast of ~ 5 mag at $0''.2$ and ~ 10 mag at separations $> 1''.5$.

We combined the achieved mass detection limits and the information on the discs to place constraints on the presence of undetected companions around our targets. We found that the size of the discs (or of the outer belt, in the case of the 4 double-belt targets) can in principle be explained via self-stirring for all of our stars. However, the extent of the gap in the double-belt systems requires the presence of multiple low-mass planets (around a few tens of Earth masses). Finally, three targets in our survey show a proper motion anomaly between the GAIA and the Hipparcos data: HD 161868, HD 8907 and HD 113337. This anomaly can be explained with the presence of a companion with specific mass and semi-major axis. Using our achieved mass limits and information on the disc, we constrained this $m_{pl} - a_{pl}$ parameter space and made predictions

on the mass and radial separation of currently undetected companions around HD 161868 and HD 8907. We did a similar study for HD 113337 and we found out that the previously reported companion candidate around this star (found with RV observations) would have the right mass and radial separation to explain the observed anomaly; this suggests that the RV signal is real and that the candidate is a physical, bounded companion.

5.2 Future perspective

5.2.1 Follow-up observations

In Chapter 2 we concluded that the newly discovered companion around HD 193571 is likely the main responsible for the stirring of the disc. However, this relies on a number of assumptions about the disc size and the eccentricity of the companion. Follow-up direct imaging observations of the systems are needed to constrain its orbital parameters and thus being able to better understand the relative importance between self-stirring and companion-stirring. Given the companion projected separation of ~ 11 au, a baseline of several years would be needed between observations to be able to detect a substantial fraction of its orbit, and it is thus not feasible in the immediate future.

An equally important goal, and achievable in the short-term, would be imaging the debris disc. The disc has never been spatially resolved and the basic available SED is lacking (sub-)mm datapoints, resulting in an estimation of the disc size that is poorly constrained. A resolved image of the disc would provide a disc size more reliable than what obtained via SED fitting. Furthermore, resolving the disc would allow us to place constraints on its currently unknown inclination and, assuming a coplanar orbit for the companion, this will result in a better estimation of its real orbital radius.

At least three targets from the L^IStEN survey would benefit from additional follow-up observations: HD 161868, HD 8907 and HD 113337. For HD 161868 and HD 8907, radial velocity observations would allow to constrain the presence of an unseen massive companion within few au, which could explain the observed proper motion anomaly (however, the early spectral type of HD 161868 might prove challenging for RV observations). For HD 113337, additional RV observations might confirm the second planetary candidate at ~ 5 au, and corroborating the hypothesis that such companion is real and responsible for the proper motion anomaly.

5.2.2 A large and coherent H α survey

We successfully detected H α emission from the companion around PZ Tel (see Chapter 3) and even though this emission is likely due to chromospheric activity, rather than gas accretion, the

detection is important for a number of reasons. Firstly, we expanded the number of known companions detected in $H\alpha$ and secondly, we further proved the feasibility of using high-contrast imaging to detect $H\alpha$ emission in binary systems and the use of $H\alpha$ as a companion tracer. This is an important step towards conducting a larger study of $H\alpha$ emission, with the goal of constraining the accretion phase of planetary and low-mass stellar companions.

Extended knowledge of this accretion phase is of crucial importance when it comes to estimate the mass of these objects. The current planetary evolution models (Allard et al. 2013; Baraffe et al. 2003; Fortney et al. 2008; Spiegel & Burrows 2012), which are used to estimate the mass of a companion given its magnitude, assume that all the luminosity comes from the companion photosphere without considering contribution by the circumplanetary disc. In cases in which the companion is still in the accreting phase, the infalling gas from the circumstellar disc shocks at the circumplanetary's disc surface, resulting in dissociation of H_2 molecules and hydrogen ionisation, with consequent $H\alpha$ emission. If this is not taken into account, the resulting accretion luminosity will be mistakenly translated into a mass while using evolutionary models, thus leading to incorrect mass estimations. Recent works show that even a low mass accreting circumplanetary disc ($\dot{M} = 10^{-8} M_{\odot} \text{yr}^{-1}$) around a $1 M_J$ planet could be in the near-IR (J, H, K bands) as bright as a $10 M_J$ object (Zhu 2015). This suggests that accretion processes related to the circumplanetary disc can easily be the main source of luminosity for newly forming companions. Establishing the presence (or the absence) of gas accretion in these systems and correlating it with the system's parameters (such as age, information on the disc mass and structure, and estimated companion's mass), is therefore crucial.

Cugno et al. (2019) obtained $H\alpha$ observations of 6 targets which are either hosting a companion candidate, or with resolved disc sub-structures hinting at the presence of an unseen companion. While this is a very valuable work, I argue that the next step should be a large and coherent $H\alpha$ survey focusing primarily on systems with previously known and independently confirmed companions, in order to be able to correlate the $H\alpha$ emission to the accretion process. Moreover, Szulágyi & Mordasini (2017) also concluded that the higher the companion's mass, the more the gas entropy is reduced passing through the circumplanetary's shock surface, thus producing higher accretion luminosities. This supports the need for a wide range of estimated companion's masses, from giant planets all the way up to brown dwarf companions, in order to evaluate the robustness of such a correlation, leading to a better understanding of the first phases of the formation of planets and low mass stellar companions.

5.2.3 Deepening our understanding of companion-disc interaction

In Chapter 4 I presented the analysis of the DD-hosting targets of the L^IStEN survey, for a total of 22 targets, for which I studied the planet-disc interaction combining DI information with

information on the disc and on known companions. While the survey is considered completed and delivered interesting conclusions for single systems, the size of its target sample is rather too small to draw statistically meaningful conclusions on the matter of companion-disc interaction as a whole. Increasing this sample is therefore a primary goal, and efforts are needed toward increasing the number of resolved circumstellar discs (using such facilities as ALMA), as well as obtaining additional constraints on the presence of companions around stars with an already resolved disc, using both direct imaging and indirect detection techniques.

At the moment of writing there are still a few tens of systems in the northern hemisphere for which the disc has been fully or partially resolved, but that still lack deep high-contrast imaging observations (and for which such observations would be feasible). Obtaining DI data for these objects should be a primary goal, and efforts toward this end are currently undergoing. An example is the recently accepted proposal to use the LBT to obtain M band ADI observations of 4 protoplanetary discs, which have been recently resolved by ALMA as part of the Disk Substructures at High Angular Resolution Project (DSHARP, [Andrews et al. 2018](#)). The proposal, of which I am a co-investigator, has the twofold goal of resolving these 4 discs in scattered light, and placing constraints on the presence of possible unseen companion candidates that might be responsible for the discs structure and morphology.

The NaCo-IPY survey obtained deep DI data in L' band for more than 50 targets with a resolved debris disc. A companion-disc analysis for these targets, similar to what presented in Section 4.5, will be published in an upcoming NaCo-IPY paper. In addition, occurrence rates for companions around disc-hosting stars (whether resolved or not) constitute another important piece of the puzzle, and to this end the LISTEN and NaCo-IPY contrast curves and detection limits are planned to be combined for a joint statistical analysis of the occurrence rate of planetary and low-mass stellar companions around young, nearby stars with debris discs.

Finally, even though the focus of this Thesis is on the direct imaging technique, it is important to stress out that a complete picture of the exoplanet field can be obtained only combining all the methods and techniques at our disposals. Radial velocity observations, as well as transits and astrometry data, can place further and complementary constraints on the presence of unseen companions, and joint efforts are needed to unveil the intricacies of companion-disc interactions, and of planet formation and evolution as a whole.

Supplementary material for Chapter 2

A.1 IRDIS disc non-detection

We observed HD 193571 with SPHERE/IRDIS at the VLT in coronagraphic Differential Polarisation Imaging (DPI) mode on 26 September 2018, using the H broad-band filter.

We took eight polarimetric cycles, each consisting of four data cubes, one per half wave plate (HWP) position. Each data cube consisted of four individual exposures with exposure times of 32 s. The science observations were bracketed with 2-second exposures, to create an unsaturated PSF reference for the central star.

The data were reduced following the prescription in [Ginski et al. \(2016\)](#), obtaining the radial Stokes components Q_Φ and U_Φ (see [Schmid et al. 2006](#)), where Q_Φ would contain any polarisation signal coming from dust scattered light, and it is shown in Figure A.1. No emission is visible at the expected location of the disc ($\sim 1''.75$) or anywhere else. The faint emission from the centre is due to the stellar halo, and the telescope spider holding the coronagraph in place is vaguely visible extending approximately in the North-South direction.

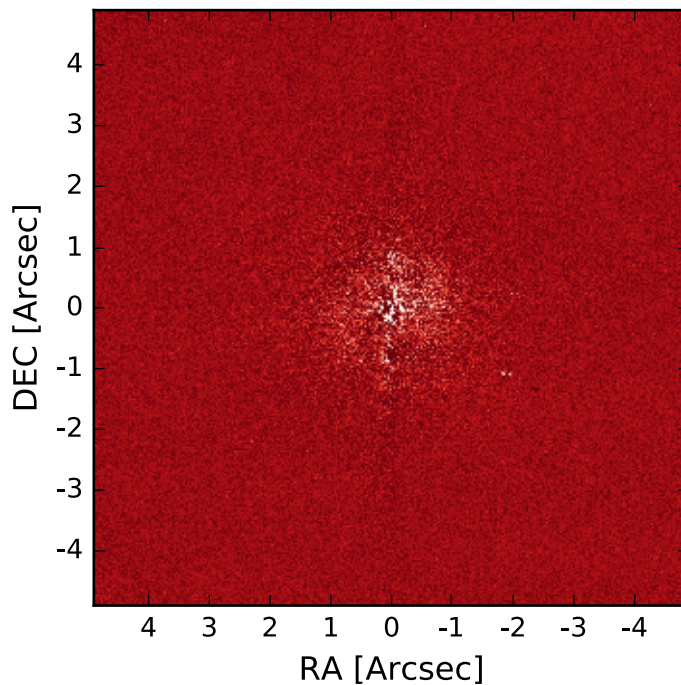


Figure A.1: DPI data taken with SPHERE/IRDIS, with a total field of view of $\sim 10'' \times 10''$, given a pixel scale for IRDIS of 12.25 mas/pix. No polarised signal from the disc scattered light is visible. The image is oriented with North up and East left.

A.2 Stirring mechanisms

In the following we present the analytical expressions that describe companion-disc interaction (see Section 1.3.1), and that are used in the data analysis of Section 2.5.

Self-stirring

From Wyatt (2008) the maximum fractional luminosity f_{\max} of a planetesimal belt at distance r around a star of mass m_{\star} , luminosity L_{\star} , and age t_{age} is

$$f_{\max} = 0.58 \times 10^{-9} r^{7/3} (dr/r) R_{\max}^{0.5} Q_{\text{D}}^{\star 5/6} e^{-5/3} m_{\star}^{-5/6} L_{\star}^{-0.5} t_{\text{age}}^{-1}, \quad (\text{A.1})$$

where R_{\max} is the maximum size of the planetesimals that are participating in the cascade at that given time (called D_{c} in Wyatt 2008), Q_{D}^{\star} is the planetesimal strength in Jkg^{-1} , e is the mean planetesimal eccentricity, and dr/r is the relative width of the planetesimal belt. It was found (see Wyatt 2008) that the population of debris discs around A stars can be fitted assuming $Q_{\text{D}}^{\star} = 150 \text{Jkg}^{-1}$, $e = 0.05$, and $dr/r = 0.5$. All of this assumes that the disc has been stirred for its whole lifetime (i.e. $t_{\text{stir}} = t_{\text{age}}$). The disc evolution model developed in Wyatt 2008 is

SED-based, and therefore the planetesimal belt distance r refers to the black-body radius R_{BB} , which for HD 193571 is inferred via SED fitting and it is 62 au.

Companion-stirring

From [Mustill & Wyatt \(2009\)](#), the threshold velocity above which collisions between planetesimal of size R become destructive is

$$v_{\text{rel}}^*(R) = \left[0.8 \left(\frac{R}{80 \text{ m}} \right)^{-0.33} + 0.2 \left(\frac{R}{80 \text{ m}} \right)^{1.2} \right]^{0.83} \text{ ms}^{-1} \quad (\text{A.2})$$

A companion of mass m_{pl} internal to the disc on an orbit of semi-major axis a_{pl} and eccentricity e_{pl} , around a primary of mass m_{\star} , would be able to stir planetesimals to catastrophic collisions only up to a maximum distance a^* :

$$a^*(R) = 3.8 \text{ au} \left(\frac{e_{\text{pl}}}{0.1} \right)^{2/3} \left(\frac{m_{\star}}{1 M_{\odot}} \right)^{1/3} \left(\frac{a_{\text{pl}}}{1 \text{ au}} \right)^{2/3} \left(\frac{v_{\text{rel}}^*(R)}{1 \text{ kms}^{-1}} \right)^{-2/3} \quad (\text{A.3})$$

In addition, it is possible to calculate the timescale for orbit crossing of planetesimals at a distance a as

$$t_{\text{cross}} \sim 1.53 \times 10^3 \frac{(1 - e_{\text{pl}}^2)^{3/2}}{e_{\text{pl}}} \left(\frac{a}{10 \text{ au}} \right)^{9/2} \times \left(\frac{m_{\star}}{M_{\odot}} \right)^{1/2} \left(\frac{m_{\text{pl}}}{M_{\odot}} \right)^{-1} \left(\frac{a_{\text{pl}}}{1 \text{ au}} \right)^{-3} \text{ yr} \quad (\text{A.4})$$

Companion-stirring versus self-stirring

[Mustill & Wyatt \(2009\)](#) also defined the parameter Φ as the distance boundary between self-stirring and companion-stirring at a fixed age, as:

$$\Phi = 630 \text{ au} (1 - e_{\text{pl}}^2)^{-1} e_{\text{pl}}^{2/3} \left(\frac{m_{\text{pl}}}{M_{\odot}} \right)^{2/3} \times \left(\frac{a_{\text{pl}}}{1 \text{ au}} \right)^2 \left(\frac{m_{\star}}{M_{\odot}} \right)^{-4/3} x_{\text{m}}^{-0.77}, \quad (\text{A.5})$$

where the dimensionless parameter x_{m} is a scaling factor relating the disc surface density to the minimum mass solar nebula density (see [Mustill & Wyatt 2009](#) and [Kenyon & Bromley 2008](#)). The model developed in [Mustill & Wyatt 2009](#) is a dynamic model that depends on the physical structure of the disc, and therefore on the real disc size, which is of 120 au for the HD 193571 disc (see Section 2.2).

A.3 Orbital constraints with OFTI

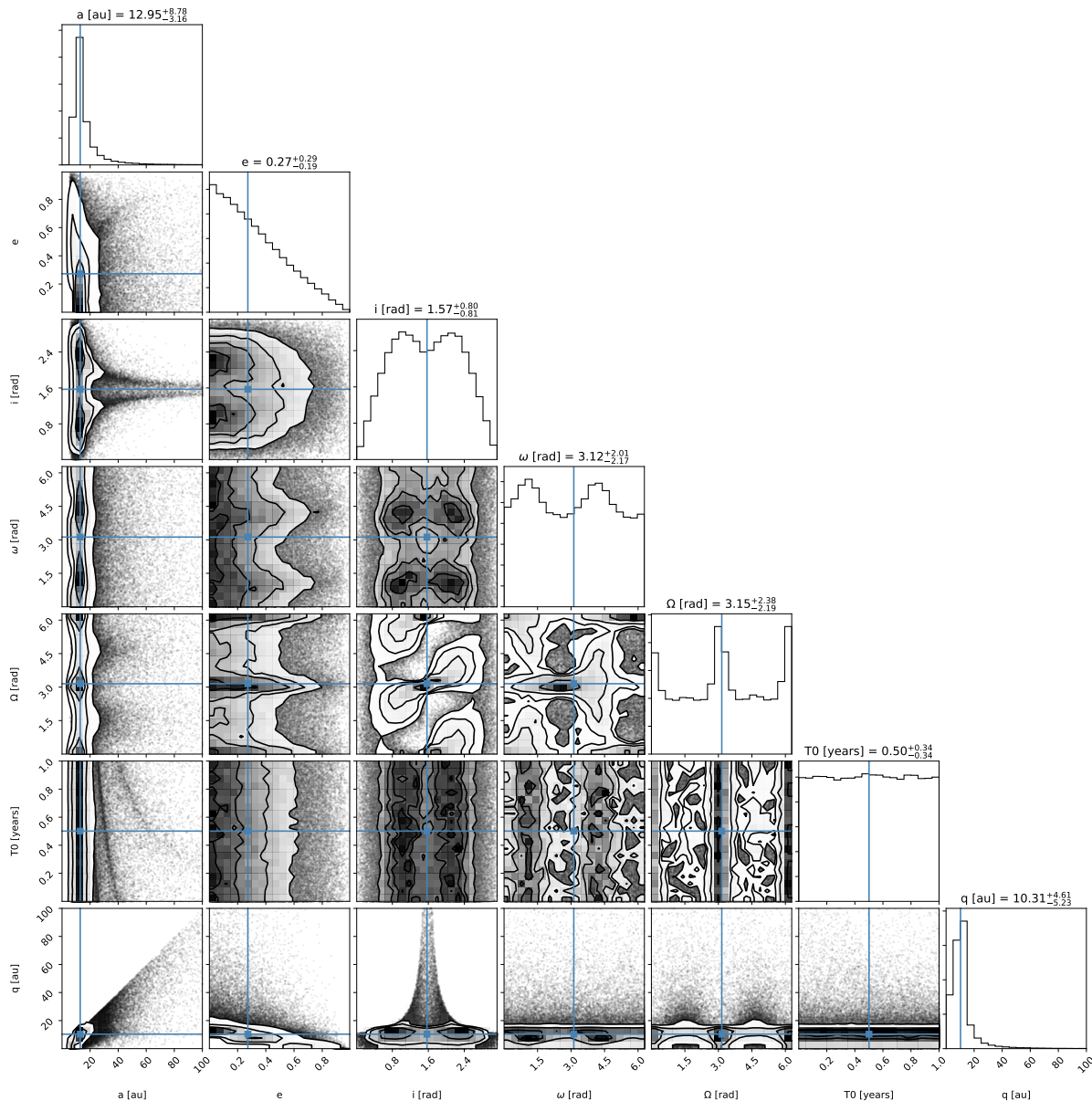


Figure C.1: Posterior distribution function for the orbital parameters derived with the *orbitize* package using the OFTI implementation.

We explored the possible orbital motion parameters for the companion around HD 193571 using the python package *orbitize* with the Orbit For The Impatient (OFTI) algorithm detailed in [Blunt et al. \(2017\)](#). We used two total mass estimates: $2.6 \pm 0.1 M_{\odot}$ (for an age of 161 Myr) and $2.5 \pm 0.1 M_{\odot}$ (for an age of 66 Myr). We used a uniform prior for the semi-major axis, and in the epoch of periastron passage and argument of periastron. We used a $\sin(i)$ prior for the inclination angle, and a linearly descending prior for the eccentricity, with a slope of -2.18 . For both age estimates, the results agree within the error bar, and in Figure C.1 we show the

posterior distribution function for the 161 Myr case. As shown in the figure, the uncertainties on the astrometry and the limited number of datapoints do not allow us to place any meaningful constraints on the orbital elements, but the periastron distance q is restricted to $\lesssim 15$ au.

B.1 Angular spectral differential imaging

The ASDI technique is a two step combination of spectral differential imaging (SDI) ([Racine et al. 1999](#)) and ADI technique, where the images are first reduced with the SDI method, and then combined with a classical ADI reduction. The SDI technique relies on comparing images taken in different wavelengths, since any physical object would maintain the same position while speckles and Airy patterns would scale and move radially as a function of wavelength. In order to compare the continuum frames to the narrow band filter frames, we modified the continuum images as follows: we multiply all the Cnt_Ha frames by the ratio of the NHa filter width to the Cnt_Ha filter width (see Table 3.2), in order to correct for the different filter throughput.

We then stretch these normalised Cnt_Ha frames radially, by the ratio of the filters central wavelengths, using spline interpolation. This step is done in order to align the speckle patterns. We subtracted these modified Cnt_Ha frames to the NHa frames, in order to correct for all the wavelength-dependent patterns.

We finally reduced these subtracted frames using classical ADI reduction (the frames are de-rotated to the same parallactic angle and median combined) producing the ASDI reduced image shown in the right panel of Figure 3.1.

B.2 Photometry

We follow the prescription in [Cugno et al. \(2019\)](#), Section 3.4.2, but applying it to the flux frames, because the science frames have a coronagraph blocking the central star.

For the extinction calculation, we use the extinction law of [Cardelli et al. \(1989\)](#):

$$A_\lambda = a(\lambda) + \frac{b(\lambda)}{R_V}$$

With $a(\lambda)$ and $b(\lambda)$ interpolated at $\lambda \sim 0.65 \mu\text{m}$ ($a(\lambda) = 0.91$ and $b(\lambda) = -0.26$), $R_V = 3.1$ and $A_V = 0.53^{+0.84}_{-0.53}$ from [Schmidt et al. \(2014\)](#); obtaining $A_{H\alpha} = 0.44^{+0.69}_{-0.44}$. We use the value of 0.44, without uncertainties.

We proceeded as follows: in the flux frames part of the pixels are obscured due to the spider and the coronagraph. We manually create a mask over these features and interpolate the flux frames using the `interpolate.griddata` package of `scipy`, with a linear interpolation.

We calculate the count rate in the single flux frames inside an aperture of radius 1.3 arcsec, using the `photutils` Python package to create the desired aperture and sum all the pixel values inside (the package allows for fraction of pixels to be taken into account). Due to the relative low integration time for the flux frames (52 seconds) the frames are read-out noise dominated, rather than background dominated. To account for this, we also evaluated the count rates in a background annulus around the central star and, scaling according to the area, we subtracted the background counts to the total counts. We do this for both continuum and narrow band frames. We then evaluate the mean count rate and relative uncertainty σ/\sqrt{n} and divide them by the integration time, obtaining the count rate per second $cts_{\text{CntHa}} = 70353.6 \pm 258.1$, and $cts_{\text{NHa}} = 14094.0 \pm 80.4$.

We convert these count rates into flux densities using eq. 1 of [Cugno et al. \(2019\)](#) or eq.4 of [Schmid et al. \(2017\)](#), as:

$$F_\lambda^* = cts \times 10^{0.4(am k_1 + m_{\text{mode}})} \times c_{zp}^{\text{cont}} \quad (\text{B.1})$$

With am being the airmass during the observations, k_1 being the atmospheric extinction correction at Paranal (0.085 ± 0.004 for Cnt_Ha and 0.081 ± 0.002 for N_Ha, from [Patat et al. 2011](#)), and c_{zp}^{cont} being the zeropoint for the desired filter (see Table 3.2).

So, the flux density in the Continuum filter Cnt_Ha, is:

$$F_\lambda^*(\text{Cnt_Ha}) = (9.9 \pm 0.3) \times 10^{-13} \text{ erg/cm}^2/\text{s}/\text{\AA}.$$

We assume that the flux density of the primary is the same in both continuum and narrow band filter. We then calculate the flux in the continuum filter $F_{\text{Cnt_Ha}}$, and the flux in the narrow filter due to the continuum emission $F_{\text{N_Ha,cont}}$, as the continuum flux density multiplied by the two filter widths. After correcting for the extinction, the two fluxes (in the continuum filter, and in the narrow filter due to the continuum emission) are:

$$F_{\text{Cnt.Ha}}^* = (5.68 \pm 0.18) \times 10^{-11} \text{ erg/cm}^2/\text{s}$$

$$F_{\text{N.Ha,cont}}^* = (1.11 \pm 0.04) \times 10^{-11} \text{ erg/cm}^2/\text{s}$$

The continuum flux density can also be used to estimate the counts in the narrow band filter that are due to the emission in the continuum, using eq.2 of [Cugno et al. \(2019\)](#). We obtain $cts_{\text{NHa}} = 11186.2 \pm 665.9$ counts.

Subtracting these counts to the total counts evaluated in the N.Ha filter (i.e: cts_{NHa}) allows us to obtain the counts in the filter due to line emission only, which are then converted into a line flux using eq.1 (with line zeropoint). After correcting for extinction, we obtain:

$$F_{\text{N.Ha,line}}^* = (3.53 \pm 0.8) \times 10^{-12} \text{ erg/cm}^2/\text{s}.$$

The final total flux in the narrow filter is then the sum of the line and continuum contribution:

$$F_{\text{N.Ha}}^* = F_{\text{N.Ha,line}}^* + F_{\text{N.Ha,cont}}^*$$

$$F_{\text{N.Ha}}^* = (1.47 \pm 0.09) \times 10^{-11} \text{ erg/cm}^2/\text{s}.$$

B.3 Alternative Photometric Analysis

We also performed the photometric analysis with an alternative method, which addresses the assumption that the flux density of the primary is the same in both filters. We selected a suitable PHOENIX model spectrum ([Husser et al. 2013](#)) with the stellar parameters reported in Table 3.1. We reduced publicly available FEROS spectrum of the primary, and used the aforementioned PHOENIX model to flux-calibrate them in units of $\text{erg/s/cm}^2/\text{\AA}$.

We integrated the calibrated FEROS spectrum over the ZIMPOL filters, obtaining a synthetic photometry; which we then corrected comparing it the observed ZIMPOL photometry (see Appendix B.2). The resulting correction factors are 0.93 for the N.Ha and 1.28 for the Cnt.Ha filters, respectively.

We calculated the Cnt.Ha to N.Ha flux ratio. Now, instead of assuming that the flux density of the primary is the same in both filters, we use this filter flux ratio to correctly evaluate the continuum flux density of the primary in the N.Ha filter.

We then use a PHOENIX model spectrum with the parameters of the PZ Tel B (see Table 3.1) to estimate its theoretical value in band fluxes. As expected, the Cnt.Ha flux matches the observed one, while the measured N.Ha flux is much brighter than the one expected from the model, due to the presence of $H\alpha$ emission.

We used the PHOENIX model of PZ Tel B to evaluate the flux ratio between the two filters, and then we used it to predict the continuum contribution to the measured N.Ha flux based on the measured Cnt.Ha flux. Subtracting the continuum contribution to the N.Ha flux leaves only the line contribution and, after accounting for the filter transmission curve, we obtain a $H\alpha$ line flux of $2.90 \times 10^{-15} \text{ erg/cm}^2/\text{s}$.

The $H\alpha$ line flux obtained with this alternative method is consistent within uncertainties with the value of $(2.17 \pm 0.9) \times 10^{-15}$ erg/cm²/s reported in Section 3.4.2. We also evaluated the impact that a different PHOENIX model spectrum for PZ Tel B can have on the final results, assuming the lower and upper end of the parameters reported in Table 3.1. For a temperature of 2500 K, a bolometric luminosity of $0.002 L_{\odot}$ and a mass of $38 M_{J}$ we obtain a $H\alpha$ line flux of 2.90×10^{-15} erg/cm²/s. While for $T=2700$ K, $L = 0.003 L_{\odot}$ and $M = 72 M_{J}$ we obtain a line flux of 2.90×10^{-15} erg/cm²/s. Both values agree with the the line flux reported in Section 3.4.2.

C.1 Master flat and bad pixel mask creation

The LMIRCam is affected by vignetting, which can be seen as pixels around the border of the detector being substantially darker than the rest of the image. In addition to other possible bad pixels, there is also a known cluster of bad pixels roughly in the middle of the detector referred to as the 'bullet hole', which we carefully tried to avoid during observations and offsets. All of these issues make the creation of master Flats and the handling of bad pixels a task that requires particular attention.

On October 8th, 2017, we took a series of flats observations with DIT's of 0.3, 0.7, 1., 1.4, 1.8, 2.1, 2.5, 2.9, and 3.2 seconds, taking 30 flats per DIT and then mean combining them, ending up with one flat per each DIT. For each pixel we fit a linear relation as a function of DIT's, saving all the resulting slopes. We then divided the highest DIT flat by the lowest DIT one, ending up with an array of ratios.

We marked as 'bad' pixels all of those that deviate more than a certain amount from the median of all ratios, thus creating a series of 'bad pixel maps'. We then inspected these maps by eye, to select the right trade off between effectively masking the vignetting part and the bullet hole, and not labelling an overwhelming amount of pixels as 'bad'. We selected a deviation from the median-normalised ratios of 1.3 as our best trade-off. We used this mask while normalising the array of slopes, ending up with our master flat.

This procedure was applied to data taken in the 2017B run, with a detector window size of 2048×1280 pixels, and therefore the resulting master flat and bad pixel map can be used for every dataset taken with the same window size (i.e.: for 2017B and 2018A run data). Due to work being done on the LMIRCam detector and the relative change of the vignetted area, we used a window size of 2048×1024 pixels for all the data taken in the 2018B and 2019A run. Due to the different window size, and to the possibly changed bad pixels, we created a new master flat and bad pixel mask for these data. The procedure is the same as explained for the 2017 master flat creation, but we used a set of 80 frames with a DIT of 0.068 seconds, 80 frames with DIT of 0.109 seconds and 40 frames with DIT of 0.302 seconds. The best trade-off for the bad pixel map was found with a deviation of 0.15.

We used a slightly less stringent bad pixel map during the bad pixel correction step in our data reduction: 1.5 deviation for the 2017B and 2018A data, and 0.25 deviation for the 2018B and 2019A data. During the star(s) location step, we sometimes used a very stringent bad pixel mask for some of our targets (usually, the 0.15 or 0.10 deviation map) in order to completely avoid random hot pixels to be confused with the stellar peak(s).

C.2 Stacked VS unstacked frames

We evaluated 5σ detection limits for all of our DD targets using both the unstacked frames, and the stacked ones (see Section 4.4). Given the computational time required to create contrast curves using the unstacked frames, we limited the analysis to a radial separation of $1''.4$. We show the comparison between stacked and unstacked contrast curves (for both mirrors, when applicable) for a representative number of PC of 20, in Figure C.1.

As visible in the figure, the detection limits are on average comparable between the stacked and unstacked frames, for both mirrors. For several targets, using stacked frames allows to achieve better detection limit at a given separation, with respect to the detection limit reached using the unstacked frames.

Given the results, we decide to use the stacked frames for the rest of the analysis, since the achieved limits are comparable and the computational time is significantly reduced.

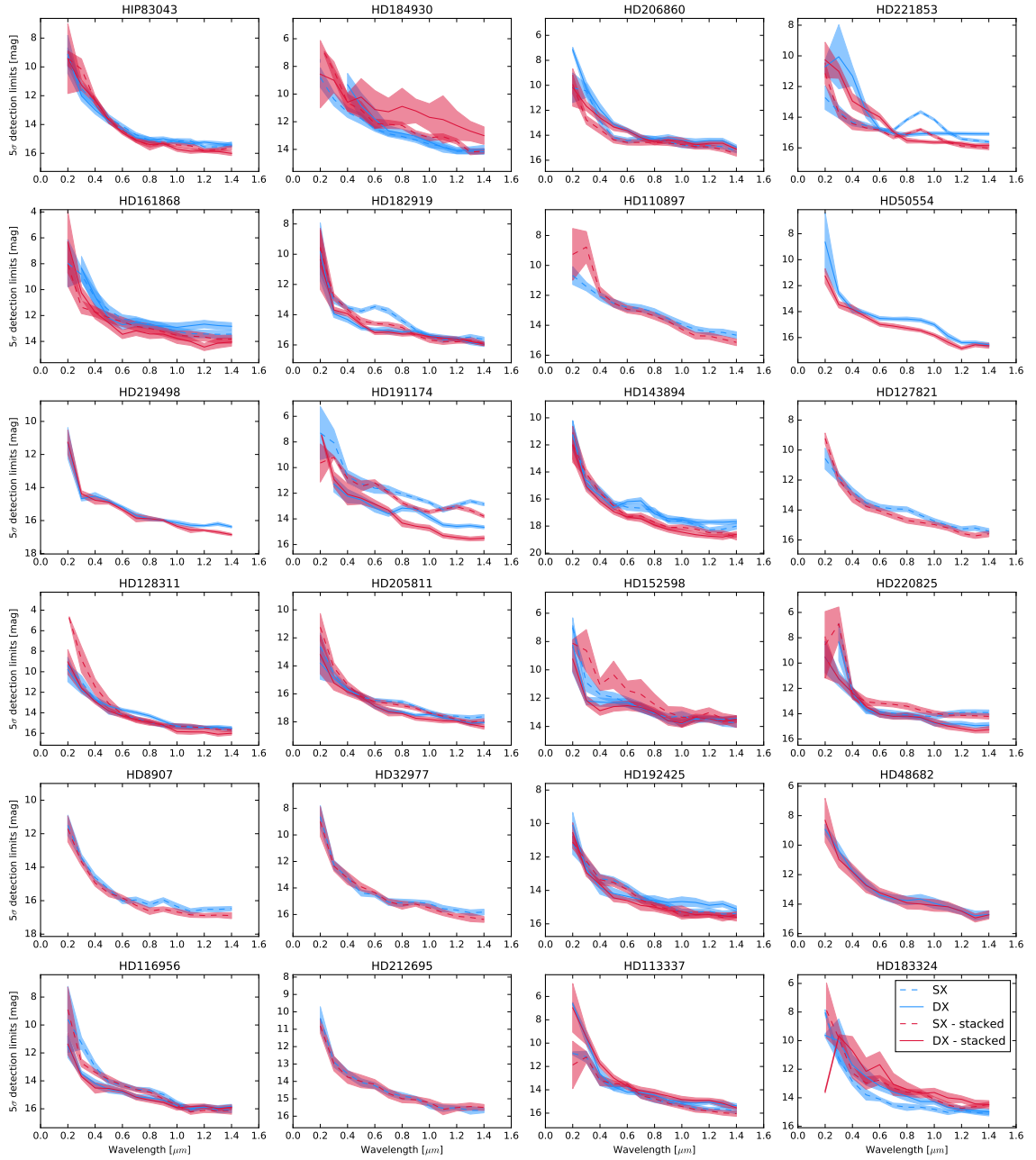


Figure C.1: Comparison between the 5σ detection limits achieved using the unstacked and stacked frames for all the DD-hosting targets. In blue we show the unstacked curves, together with their uncertainty (blue shaded area), and in red we show the limits and uncertainty achieved with the stacked frames. We do the analysis for both mirrors, showing the left ‘SX’ mirror with a dashed line, and the right ‘DX’ mirror with a solid line.

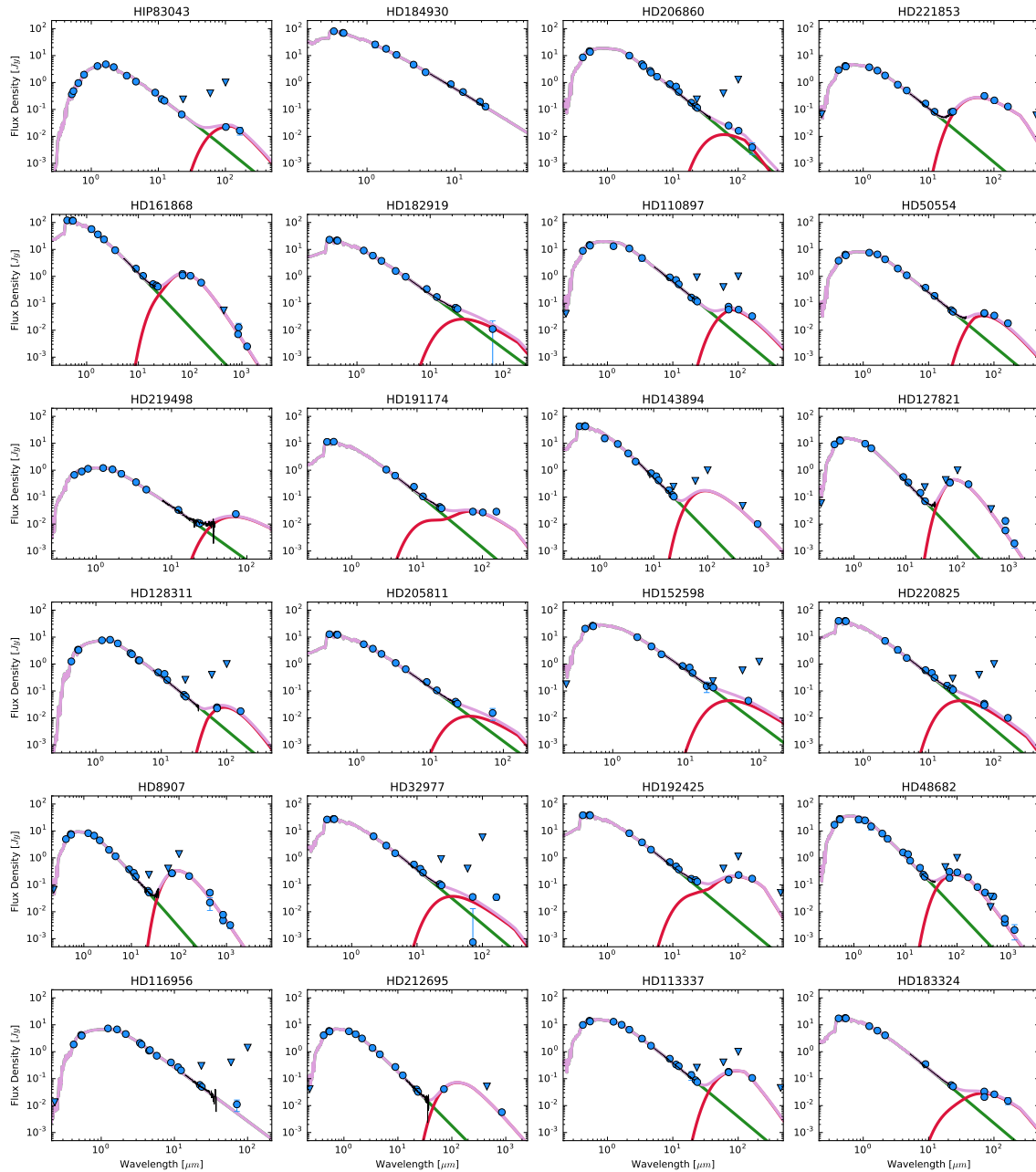


Figure C.2: Flux density distribution of the DD-hosting targets for the LISStEN survey. The blue points are the photometric datapoints found in the literature, with blue triangles indicating upper limits. The black line is the IRS spectrum, while the green and red lines are the fitted stellar and disc fluxes, respectively.

Table C.1: 5σ contrast curves and mass detection limits for all the L1StEN targets

Target	0''2		0''4		0''6		0''8		1''0		1''5	
	$\Delta L'$	M_J	$\Delta L'$	M_J	$\Delta L'$	M_J	$\Delta L'$	M_J	$\Delta L'$	M_J	$\Delta L'$	M_J
HD 206860	5.73	96.46	9.09	17.99	10.13	11.47	10.13	11.47	10.31	10.92	11.06	8.76
HD 183324	8.05	64.02	6.75	128.76	7.25	96.46	8.11	59.88	8.61	38.3	9.15	32.62
HD 220825	4.68	437.62	7.56	91.23	9.18	35.32	9.33	32.62	9.82	26.33	10.25	24.86
HD 184930	4.11	1216.97	6.17	880.37	7.68	552.17	7.82	533.18	8.69	358.79	9.06	301.68
HD 221853	4.76	252.02	8.03	36.59	8.44	32.62	9.14	25.7	9.26	25.37	10.06	15.11
HD 127821	3.86	319.54	7.77	34.12	8.69	25.37	9.33	17.99	9.61	13.5	10.45	11.47
HD 191174	3.52	631.64	5.96	199.75	6.73	135.91	8.2	59.88	8.6	41.5	9.5	29.08
HD 110897	4.99	151.47	7.49	35.32	8.66	24.86	9.11	20.59	9.99	12.51	11.21	8.43
HD 128311	3.9	159.75	7.76	24.14	9.15	11.47	9.78	9.73	10.69	7.13	10.73	6.84
HD 152598	4.75	284.59	8.39	35.32	8.04	41.5	8.5	34.12	9.26	25.98	9.3	25.98
HD 182919	4.74	437.62	8.31	64.02	9.56	30.83	9.65	29.08	10.05	25.98	10.34	24.86
HD 116956	6.02	59.88	9.16	13.87	9.38	12.51	10.02	10.4	10.57	8.76	10.7	8.08
HD 161868	4.48	513.87	8.18	72.39	9.88	27.77	9.86	27.77	10.19	25.98	10.47	24.86
HD 192425	6.44	178.5	8.96	38.3	9.93	26.88	10.32	25.37	10.83	20.59	10.94	17.99
HD 50554	5.83	102.66	8.38	25.98	9.54	16.21	9.85	13.87	10.38	11.13	11.39	8.43
HD 219498	3.9	199.75	7.41	29.08	7.98	25.37	8.53	20.59	8.98	16.21	9.66	11.47
HD 205811	7.11	121.88	9.78	26.88	10.78	20.59	11.32	15.64	11.74	12.51	12.37	10.4
HD 8907	6.32	86.42	9.55	15.11	10.44	11.47	11.23	9.42	11.28	9.08	11.57	8.43
HD 32977	3.97	631.64	8.26	76.8	9.33	36.59	10.28	25.98	10.48	25.7	11.42	16.21
HD 48682	4.6	237.47	8.1	34.12	9.52	20.59	10.2	13.87	10.37	13.16	11.13	10.05
HD 212695	4.99	211.77	7.92	36.59	8.34	32.62	9.17	25.37	9.39	24.14	9.61	21.97
HD 113337	6.96	86.42	8.29	35.89	8.79	30.83	9.85	21.97	10.51	15.64	11.12	11.47
HD 143894	7.47	121.88	11.56	15.64	12.73	10.05	13.33	8.08	13.85	6.54	14.15	6.05
HIP 83043	3.93	76.8	6.83	17.99	9.08	7.75	9.96	5.73	10.22	5.06	10.68	4.28

The 5σ contrasts are in magnitudes and the mass limits in Jupiter masses. In case of double-sided observations, we report the best achieved contrast (and mass limits) among the two. The colours allow for better visualisation and don't bear any physical meaning.

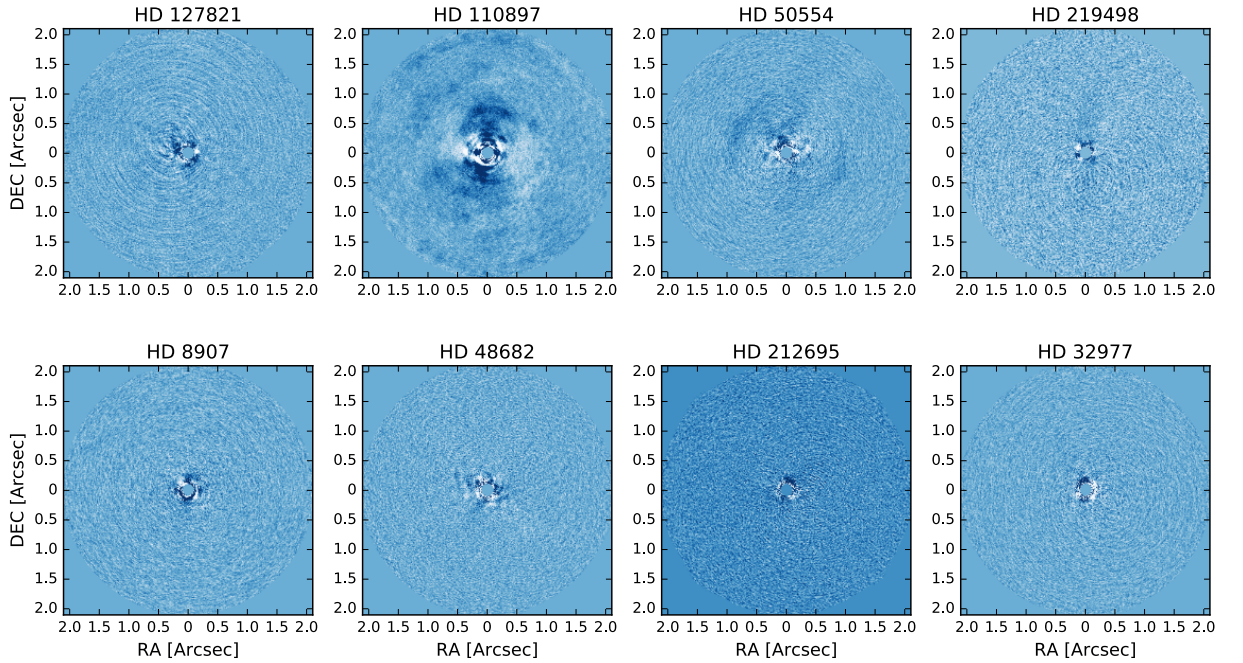


Figure C.3: ADI reduced images of the targets observed in single-sided mode, for a representative PC number of 20. The images are oriented with North up, and the colormap has been chosen to better visualise the data and bears no physical meaning.

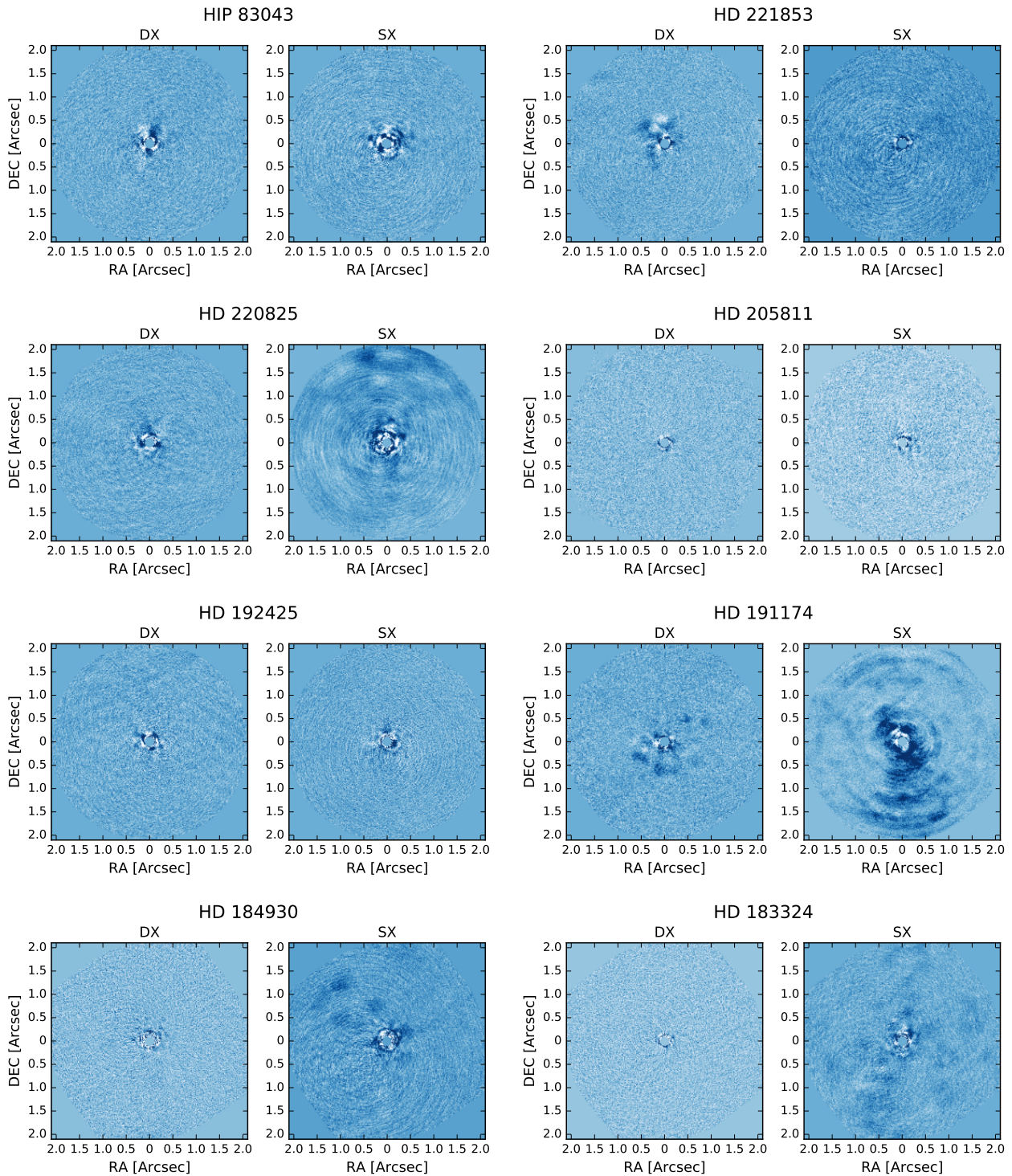


Figure C.4: ADI reduced images of the targets observed in double-sided mode, for a representative PC number of 20. The images are oriented with North up, and the colormap has been chosen to better visualise the data and bears no physical meaning.

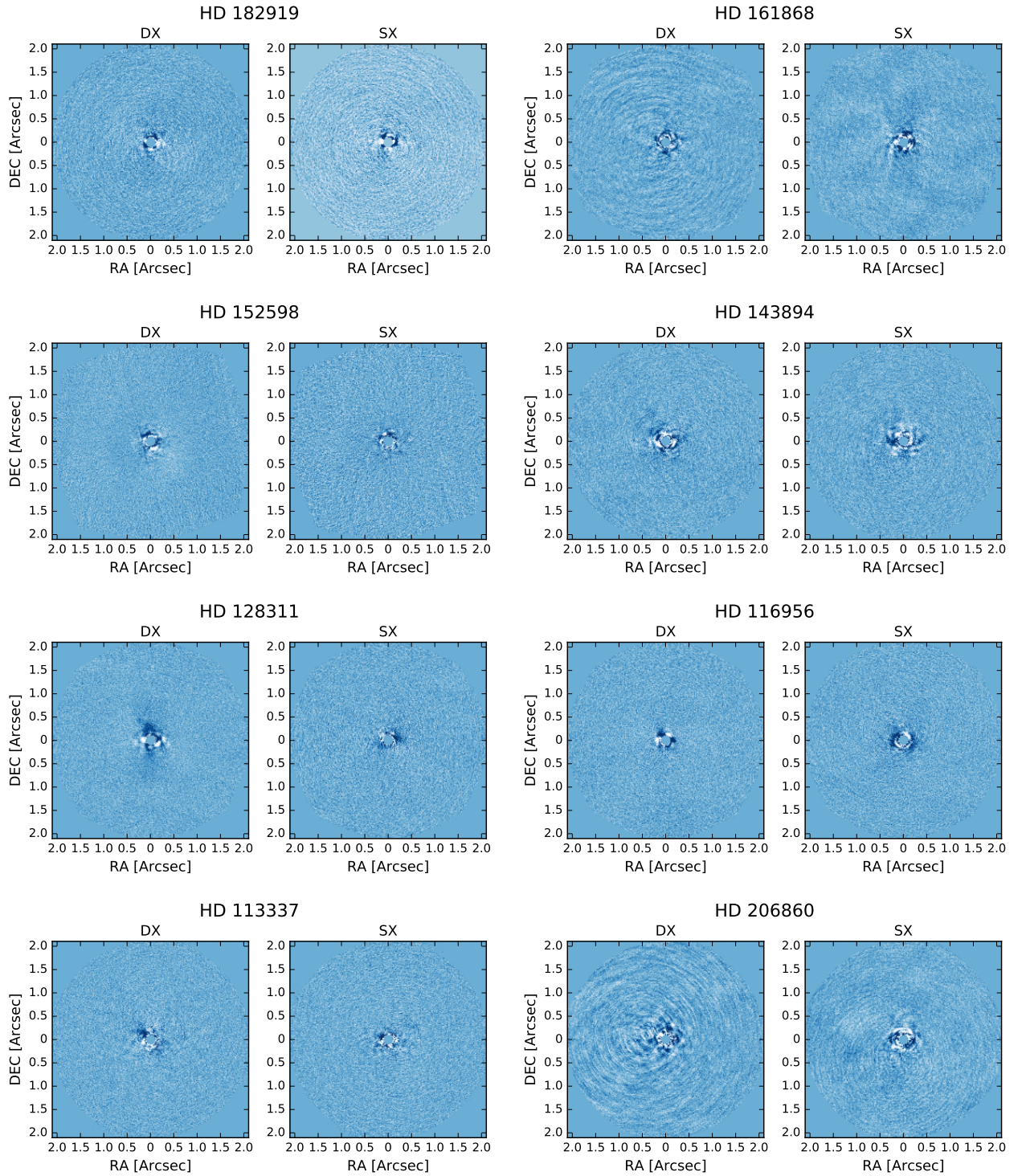


Figure C.5: As in Figure C.4

Bibliography

- Allard, F., Homeier, D., & Freytag, B. 2012, *Philosophical Transactions of the Royal Society of London Series A*, 370, 2765
- Allard, F., Homeier, D., Freytag, B., et al. 2013, *Memorie della Societa Astronomica Italiana Supplementi*, 24, 128
- Amara, A. & Quanz, S. P. 2012, *Monthly Notices of the Royal Astronomical Society*, 427, 948
- Andrews, S. M., Huang, J., Pérez, L. M., et al. 2018, *ApJ*, 869, L41
- Aoyama, Y., Ikoma, M., & Tanigawa, T. 2018, *ApJ*, 866, 84
- Bacon, R., Accardo, M., Adjali, L., et al. 2010, in *Proc. SPIE*, Vol. 7735, *Ground-based and Airborne Instrumentation for Astronomy III*, 773508
- Bailer-Jones, C. A. L., Rybizki, J., Fouesneau, M., Mantelet, G., & Andrae, R. 2018, *AJ*, 156, 58
- Baraffe, I., Chabrier, G., Allard, F., & Hauschildt, P. H. 2002, *A&A*, 382, 563
- Baraffe, I., Chabrier, G., Barman, T. S., Allard, F., & Hauschildt, P. H. 2003, *A&A*, 402, 701
- Bell, C. P. M., Mamajek, E. E., & Naylor, T. 2015, *MNRAS*, 454, 593
- Beust, H., Bonnefoy, M., Maire, A. L., et al. 2016, *A&A*, 587, A89
- Biller, B. A., Liu, M. C., Wahhaj, Z., et al. 2010, *The Astrophysical Journal Letters*, 720, L82
- Biller, B. A., Liu, M. C., Wahhaj, Z., et al. 2013, *The Astrophysical Journal*, 777, 160
- Blunt, S., Nielsen, E. L., De Rosa, R. J., et al. 2017, *AJ*, 153, 229
- Borgniet, S., Boisse, I., Lagrange, A. M., et al. 2014, *A&A*, 561, A65

- Borgniet, S., Lagrange, A. M., Meunier, N., et al. 2019a, *A&A*, 621, A87
- Borgniet, S., Perraut, K., Su, K., et al. 2019b, *A&A*, 627, A44
- Bowler, B. P. 2016, *PASP*, 128, 102001
- Bowler, B. P., Liu, M. C., Kraus, A. L., & Mann, A. W. 2014, *ApJ*, 784, 65
- Butler, R. P., Marcy, G. W., Vogt, S. S., et al. 2003, *ApJ*, 582, 455
- Cantalloube, F., Mouillet, D., Mugnier, L. M., et al. 2015, *A&A*, 582, A89
- Cardelli, J. A., Clayton, G. C., & Mathis, J. S. 1989, *ApJ*, 345, 245
- Chauvin, G., Desidera, S., Lagrange, A. M., et al. 2017, in *SF2A-2017: Proceedings of the Annual meeting of the French Society of Astronomy and Astrophysics*, ed. C. Reyl e, P. Di Matteo, F. Herpin, E. Lagarde, A. Lan on, Z. Meliani, & F. Royer, Di
- Chauvin, G., Lagrange, A. M., Bonavita, M., et al. 2010, *A&A*, 509, A52
- Chauvin, G., Vigan, A., Bonnefoy, M., et al. 2015, *A&A*, 573, A127
- Chen, C. H., Mittal, T., Kuchner, M., et al. 2014, *The Astrophysical Journal Supplement Series*, 211, 25
- Close, L. M., Follette, K. B., Males, J. R., et al. 2014, *The Astrophysical Journal*, 781, L30
- Cugno, G., Quanz, S. P., Hunziker, S., et al. 2019, *A&A*, 622, A156
- Currie, T., Marois, C., Cieza, L., et al. 2019, *ApJ*, 877, L3
- David, T. J. & Hillenbrand, L. A. 2015, *ApJ*, 804, 146
- Desidera, S., Covino, E., Messina, S., et al. 2015, *A&A*, 573, A126
- Dodson-Robinson, S. E., Su, K. Y. L., Bryden, G., Harvey, P., & Green, J. D. 2016, *ApJ*, 833, 183
- Ehrenreich, D., Lovis, C., Allart, R., et al. 2020, *arXiv e-prints*, arXiv:2003.05528
- Ercolano, B. & Pascucci, I. 2017, *Royal Society Open Science*, 4, 170114
- Esa, . 1997, *VizieR Online Data Catalog*, 1239
- Fang, J. & Margot, J.-L. 2013, *ApJ*, 767, 115
- Feroz, F., Hobson, M. P., & Bridges, M. 2009, *Monthly Notices of the Royal Astronomical Society*, 398, 1601
- Ford, E. B. 2006, *ApJ*, 642, 505
- Foreman-Mackey, D., Hogg, D. W., Lang, D., & Goodman, J. 2013, *PASP*, 125, 306

- Fortney, J. J., Marley, M. S., Saumon, D., & Lodders, K. 2008, *ApJ*, 683, 1104
- Gaia Collaboration, Brown, A. G. A., Vallenari, A., et al. 2018, *A&A*, 616, A1
- Gaia Collaboration, Prusti, T., de Bruijne, J. H. J., et al. 2016, *A&A*, 595, A1
- Galicher, R., Marois, C., Macintosh, B., et al. 2016, *A&A*, 594, A63
- Gelman, A. & Rubin, D. B. 1992, *Statistical Science*, 7, 457
- Gillon, M., Triaud, A. H. M. J., Demory, B.-O., et al. 2017, *Nature*, 542, 456
- Ginski, C., Berndt, A., Mugrauer, M., et al. 2014, *Monthly Notices of the Royal Astronomical Society*, 444, 2280
- Ginski, C., Stolker, T., Pinilla, P., et al. 2016, *A&A*, 595, A112
- Goodman, J. & Weare, J. 2010, *Communications in Applied Mathematics and Computational Science*, 5, 65
- Grankin, K. N. 2016, *Astronomy Letters*, 42, 314
- Haffert, S. Y., Bohn, A. J., de Boer, J., et al. 2019, *Nature Astronomy*, 329
- Hagelberg, J., Ségransan, D., Udry, S., & Wildi, F. 2016, *MNRAS*, 455, 2178
- Heng, K. & Tremaine, S. 2010, *MNRAS*, 401, 867
- Hintz, D., Fuhrmeister, B., Czesla, S., et al. 2019, *A&A*, 623, A136
- Holland, W. S., Matthews, B. C., Kennedy, G. M., et al. 2017, *MNRAS*, 470, 3606
- Hughes, A. M., Duchêne, G., & Matthews, B. C. 2018, *ARA&A*, 56, 541
- Husser, T., Wende-Von Berg, S., Dreizler, S., et al. 2013, *Astronomy and Astrophysics*, 553
- Ishihara, D., Onaka, T., Kataza, H., et al. 2010, *A&A*, 514, A1
- Janson, M., Brandt, T. D., Moro-Martín, A., et al. 2013, *ApJ*, 773, 73
- Jarrett, T. H., Cohen, M., Masci, F., et al. 2011, *ApJ*, 735, 112
- Jenkins, J. S., Pavlenko, Y. V., Ivanyuk, O., et al. 2012, *Monthly Notices of the Royal Astronomical Society*, 420, 3587
- Johnson, J. A., Howard, A. W., Marcy, G. W., et al. 2010, *PASP*, 122, 149
- Kains, N., Wyatt, M. C., & Greaves, J. S. 2011, *MNRAS*, 414, 2486
- Kennedy, G. M., Bryden, G., Ardila, D., et al. 2018, *MNRAS*, 476, 4584

- Kennedy, G. M. & Wyatt, M. C. 2014, *MNRAS*, 444, 3164
- Kenyon, S. J. & Bromley, B. C. 2002, *AJ*, 123, 1757
- Kenyon, S. J. & Bromley, B. C. 2008, *ApJS*, 179, 451
- Keppler, M., Benisty, M., Müller, A., et al. 2018, *A&A*, 617, A44
- Kervella, P., Arenou, F., Mignard, F., & Thévenin, F. 2019, *A&A*, 623, A72
- Konopacky, Q. M., Rameau, J., Duchêne, G., et al. 2016, *ApJ*, 829, L4
- Krivov, A. V. & Booth, M. 2018, *MNRAS*, 479, 3300
- Kruse, E. A., Berger, E., Knapp, G. R., et al. 2010, *The Astrophysical Journal*, 722, 1352
- Küçük, I. & Akkaya, I. 2010, *Rev. Mexicana Astron. Astrofis.*, 46, 109
- Lafrenière, D., Doyon, R., Marois, C., et al. 2007, *ApJ*, 670, 1367
- Lagrange, A.-M., Bonnefoy, M., Chauvin, G., et al. 2010, *Science*
- Launhardt, R., Henning, T., Quirrenbach, A., et al. 2020, *A&A*, 635, A162
- Lee, K.-G., Berger, E., & Knapp, G. R. 2009, *The Astrophysical Journal*, 708, 1482
- Lehtinen, J., Jetsu, L., Hackman, T., Kajatkari, P., & Henry, G. W. 2016, *A&A*, 588, A38
- Lenzen, R., Hartung, M., Brandner, W., et al. 2003, in *Proc. SPIE*, Vol. 4841, *Instrument Design and Performance for Optical/Infrared Ground-based Telescopes*, ed. M. Iye & A. F. M. Moorwood, 944–952
- Liu, M. C., Magnier, E. A., Deacon, N. R., et al. 2013, *ApJ*, 777, L20
- Liu, M. C., Wahhaj, Z., Biller, B. A., et al. 2010, *Society of Photo-Optical Instrumentation Engineers (SPIE) Conference Series*, Vol. 7736, *The Gemini NICI Planet-Finding Campaign*, 77361K
- Luhman, K. L., Patten, B. M., Marengo, M., et al. 2007, *ApJ*, 654, 570
- Lyubimkov, L. S., Rachkovskaya, T. M., Rostopchin, S. I., & Lambert, D. L. 2002, *MNRAS*, 333, 9
- Macintosh, B. 2013, *The Gemini Planet Imager Exoplanet Survey*, NASA OSS Proposal
- Macintosh, B., Graham, J. R., Ingraham, P., et al. 2014, *Proceedings of the National Academy of Science*, 111, 12661
- Mackay, D. J. C. 2003, *Information Theory, Inference and Learning Algorithms*, 640

- Maire, A. L., Bonnefoy, M., Ginski, C., et al. 2016, *A&A*, 587, A56
- Maire, A. L., Skemer, A. J., Hinz, P. M., et al. 2015, *A&A*, 579, C2
- Maire, J., Perrin, M. D., Doyon, R., et al. 2010, in *Proc. SPIE*, Vol. 7735, Ground-based and Airborne Instrumentation for Astronomy III, 773531
- Marois, C., Lafreniere, D., Doyon, R., Macintosh, B., & Nadeau, D. 2006, *The Astrophysical Journal*, 641, 556
- Marois, C., Macintosh, B., Barman, T., et al. 2008, *Science*, 322, 1348
- Marois, C., Zuckerman, B., Konopacky, Q. M., Macintosh, B., & Barman, T. 2010, *Nature*, 468, 1080
- Marshall, J. P., Kirchschrager, F., Ertel, S., et al. 2014, *A&A*, 570, A114
- Mason, B. D., Wycoff, G. L., Hartkopf, W. I., Douglass, G. G., & Worley, C. E. 2014, *AJ*, 122, 3466
- Mawet, D., Absil, O., Delacroix, C., et al. 2013, *A&A*, 552, L13
- Mawet, D., Milli, J., Wahhaj, Z., et al. 2014, *The Astrophysical Journal*, 792, 97
- Mayor, M. & Queloz, D. 1995, *Nature*, 378, 355
- Mayor, M. & Queloz, D. 1995, A Jupiter-mass companion to a solar-type star
- Meeus, G., Montesinos, B., Mendigutía, I., et al. 2012, *A&A*, 544, A78
- Milli, J., Hiben, P., Christiaens, V., et al. 2017, *A&A*, 597, L2
- Morales, F. Y., Bryden, G., Werner, M. W., & Stapelfeldt, K. R. 2016, *ApJ*, 831, 97
- Mugrauer, M., Röhl, T., Ginski, C., et al. 2012, *Monthly Notices of the Royal Astronomical Society*, 424, 1714
- Mugrauer, M., Vogt, N., Neuhäuser, R., & Schmidt, T. O. B. 2010, *Astronomy & Astrophysics*, 523, L1
- Musso Barucci, A. in prep.
- Musso Barucci, A., Cugno, G., Launhardt, R., et al. 2019a, *A&A*, 631, A84
- Musso Barucci, A., Launhardt, R., Kennedy, G. M., et al. 2019b, *A&A*, 627, A77
- Mustill, A. J. & Wyatt, M. C. 2009, *MNRAS*, 399, 1403
- Nielsen, E. L., Rosa, R. J. D., Macintosh, B., et al. 2019, *The Astronomical Journal*, 158, 13

- Patat, F., Moehler, S., O'Brien, K., et al. 2011, *A&A*, 527, A91
- Paunzen, E. 2015, *A&A*, 580, A23
- Pawellek, N. 2016, PhD thesis, University of Jena
- Pawellek, N. & Krivov, A. V. 2015, *MNRAS*, 454, 3207
- Pearce, T. D., Wyatt, M. C., & Kennedy, G. M. 2015, *MNRAS*, 448, 3679
- Perrier, C., Sivan, J. P., Naef, D., et al. 2003, *A&A*, 410, 1039
- Perryman, M. 2018, *The Exoplanet Handbook*
- Petrus, S., Bonnefoy, M., Chauvin, G., et al. 2020, *A&A*, 633, A124
- Racine, R., Walker, G. A. H., Nadeau, D., Doyon, R., & Marois, C. 1999, *Publications of the Astronomical Society of the Pacific*, 111, 587
- Rameau, J., Chauvin, G., Lagrange, A.-M., et al. 2013, *The Astrophysical Journal Letters*, 772, L15
- Reiners, A., Zechmeister, M., Caballero, J. A., et al. 2018, *A&A*, 612, A49
- Riviere-Marichalar, P., Barrado, D., Montesinos, B., et al. 2014, *A&A*, 565, A68
- Robertson, P., Endl, M., Cochran, W. D., & Dodson-Robinson, S. E. 2013, *The Astrophysical Journal*, 764, 3
- Rosa, R. J. D., Nielsen, E. L., Blunt, S. C., et al. 2015, *The Astrophysical Journal*, 814, L3
- Rousset, G., Lacombe, F., Puget, P., et al. 2003, in *Proc. SPIE*, Vol. 4839, *Adaptive Optical System Technologies II*, ed. P. L. Wizinowich & D. Bonaccini, 140–149
- Sallum, S., Follette, K. B., Eisner, J. A., et al. 2015, *Nature*, 527, 342
- Santamaría-Miranda, A., Cáceres, C., Schreiber, M. R., et al. 2018, *MNRAS*, 475, 2994
- Schmid, H. M., Bazzon, A., Milli, J., et al. 2017, *A&A*, 602, A53
- Schmid, H. M., Bazzon, A., Roelfsema, R., et al. 2018, *A&A*, 619, A9
- Schmid, H. M., Joos, F., & Tschan, D. 2006, *A&A*, 452, 657
- Schmidt, T. O. B., Mugrauer, M., Neuhäuser, R., et al. 2014, *A&A*, 566, A85
- Shannon, A., Bonsor, A., Kral, Q., & Matthews, E. 2016, *MNRAS*, 462, L116
- Skemer, A., Apai, D., Bailey, V., et al. 2014, in *IAU Symposium*, Vol. 299, *Exploring the Formation and Evolution of Planetary Systems*, ed. M. Booth, B. C. Matthews, & J. R. Graham, 70–71

- Skrutskie, M. F., Cutri, R. M., Stiening, R., et al. 2006, *AJ*, 131, 1163
- Skrutskie, M. F., Jones, T., Hinz, P., et al. 2010, in *Ground-based and Airborne Instrumentation for Astronomy III*, ed. I. S. McLean, S. K. Ramsay, & H. Takami, Vol. 7735, International Society for Optics and Photonics (SPIE), 1368 – 1378
- Soter, S. 2006, *AJ*, 132, 2513
- Spiegel, D. S. & Burrows, A. 2012, *ApJ*, 745, 174
- Steele, A., Hughes, A. M., Carpenter, J., et al. 2016, *ApJ*, 816, 27
- Stolker, T., Bonse, M. J., Quanz, S. P., et al. 2019, *A&A*, 621, A59
- Stone, J. M., Skemer, A. J., Hinz, P. M., et al. 2018, *AJ*, 156, 286
- Szulágyi, J. & Mordasini, C. 2017, *MNRAS*, 465, L64
- Tamura, M. 2009, in *American Institute of Physics Conference Series*, Vol. 1158, American Institute of Physics Conference Series, ed. T. Usuda, M. Tamura, & M. Ishii, 11–16
- Thalmann, C., Janson, M., Garufi, A., et al. 2016, *ApJ*, 828, L17
- Tokunaga, A. T. 2014, in *Encyclopedia of the Solar System* (Elsevier), 1089–1105
- Uyama, T., Hashimoto, J., Muto, T., et al. 2018, *AJ*, 156, 63
- Veyette, M. J. & Muirhead, P. S. 2018, *ApJ*, 863, 166
- Vigan, A., Bonavita, M., Biller, B., et al. 2017, *A&A*, 603, A3
- Vigan, A., Patience, J., Marois, C., et al. 2012, *A&A*, 544, A9
- Vogt, S. S., Butler, R. P., Marcy, G. W., et al. 2005, *ApJ*, 632, 638
- Wagner, K., Follete, K. B., Close, L. M., et al. 2018, *ApJ*, 863, L8
- Wang, J. J., Rajan, A., Graham, J. R., et al. 2014, in *Society of Photo-Optical Instrumentation Engineers (SPIE) Conference Series*, Vol. 9147, *Ground-based and Airborne Instrumentation for Astronomy V*, 914755
- Wertz, O., Absil, O., Gómez González, C. A., et al. 2017, *A&A*, 598, A83
- West, A. A., Hawley, S. L., Walkowicz, L. M., et al. 2004, *The Astronomical Journal*, 128, 426
- West, R. G., Hellier, C., Almenara, J. M., et al. 2016, *A&A*, 585, A126
- Winn, J. N. & Fabrycky, D. C. 2015, *ARA&A*, 53, 409
- Wolszczan, A. & Frail, D. A. 1992, *Nature*, 355, 145

- Wright, E. L., Eisenhardt, P. R. M., Mainzer, A. K., et al. 2010, *AJ*, 140, 1868
- Wyatt, M. C. 2008, *Annual Review of Astronomy and Astrophysics*, 46, 339
- Wyatt, M. C., Panić, O., Kennedy, G. M., & Matrà, L. 2015, *Ap&SS*, 357, 103
- Zhou, Y., Apai, D., Metchev, S., et al. 2018, *The Astronomical Journal*, 155, 132
- Zhou, Y., Herczeg, G. J., Kraus, A. L., Metchev, S., & Cruz, K. L. 2014, *ApJ*, 783, L17
- Zhu, Z. 2015, *ApJ*, 799, 16
- Zuckerman, B., Song, I., Bessell, M. S., & Webb, R. A. 2001, *ApJ*, 562, L87

Publications

The following publications were used in this Thesis:

- **Musso Barucci, A.**, Launhardt, R., Kennedy, G., Avenhaus, H., Brems, S., van Boekel, R., Cantalloube, F., Cheetham, A., Cugno, G., Girard, J., Godoy, N., Henning, Th., Metchev, S., Müller, A., Olofsson, J., Pepe, F., Quanz, S., Quirrenbach, A., Reffert, S., Rickman, E. L., Samland, M., Segransan, D. (2019). ‘*ISPY - NaCo Imaging Survey for Planets around Young stars - Discovery of an M dwarf in the gap between HD 193571 and its debris ring*’. Published in *Astronomy&Astrophysics*, 627, A77, 10.
- **Musso Barucci, A.**, Cugno, G., Launhardt, R., Müller, A., Szulagyi, J., van Boekel, R., Henning, Th., Bonnefoy, M., Quanz, S. (2019). ‘*Detection of H α emission from PZ Telescopii B using SPHERE/ZIMPOL*’. Published in *Astronomy&Astrophysics*, 631, A84, 9.

I am also a co-author of the following publications, which have not been included in this Thesis:

- Cugno, G., Quanz, S. P., Launhardt, R., **Musso Barucci, A.**, et. al., (2019). ‘*ISPY - NaCo Imaging Survey for Planets around Young stars. A young companion candidate embedded in the R CrA cloud*’. Published in *Astronomy&Astrophysics*, 624, A29, 7.
- Launhardt, R., Henning, Th., Quirrenbach, A., Segransan, D., [...], **Musso Barucci, A.**, et. al., (2020). ‘*ISPY-NACO Imaging Survey for Planets around Young stars. Survey description and results from the first 2.5 years of observations*’. Published in *Astronomy&Astrophysics*, 635, A162, 23.

Acknowledgements

When I started to write these acknowledgements I felt almost more stressed than while writing the actual Thesis. I sat down at my desk and tried to think how to better condense 4 years of my life in a page and a half. It cannot be done. There is not enough space to remember all the memories, fun, happiness, adventures, challenges, and friends I made along the way. But I will try my best.

I would like to thank my supervisors, Thomas Henning, Ralf Launhardt, and Roy van Boekel, for all the help and support during the four years of my Thesis. Thank you for giving me the opportunity of doing my PhD at MPIA, and thanks for helping me along the way!

Thanks to André Müller, for his infinite patience with all the times I bothered him with my endless scientific questions, and for a couple of really fun football games.

Thanks to Christian Fendt, for all the relentless work and passion he puts in the IMPRS program, and for all the extra miles he goes for us.

And thanks to all the stuff at MPIA, that makes it such a wonderful place.

To my IMPRS generation, for the amazing community and bonds we created, for all the retreats, and the fun, for all the Christmas markets, and for the Porto in Porto! Thank you for all the boardgames evenings at MPIA, and for the bar nights, and for the daily student coffee!

And to all the amazing people I was lucky enough to meet in these last few years: to Asmita (thanks for everything girl, keep being the best and kindest person I have ever known!), to Manuel (for introducing me to one of my favourite hobbies, and for sharing it with me!), to Johanna (for being always there for a chat, for the love and support, and for the dresses!), to Felipe (for the games and the fun, and the cinnamon rolls!), to Arianna (for that pizza at 4 am on the Alte Brücke), to Paula (forever my Bürokollegin!), to Faustine (for the best cheese fondue I have ever had), to Miriam (for her smiles and her colourful sweaters), to Sepideh (for being the sweetest

person), to Ivana (for brownies and ice cream and Croatia, and all the puns!), to Vince and Jacob (for all the laughs, and the concerts, and those damn Youths!), to Sara (for those 6 hours in a car towards Austria, and for so much fun!), and to Christos (the wisest man I will ever know). And to so many others: to Melanie, and Camille, and Francisco, and Christian, and to Aida, Micha, Christina, Alex and Matthias.

To Josha, for his love, for his support, for his affection, for the best treasure hunts of my life, for everything. To all our amazing years so far, and to many more to come.

To the brother who was with me since the beginning: grazie fratello, firmato: sorella ;)

And to the sisters I picked up along the way: to Giulia, Isabella, Linda, Elena, Martina e Betta. I love you girls.

Ed infine, alla mia famiglia, ed ai miei genitori: grazie per il vostro affetto e sostegno, grazie per aver sempre creduto in me, grazie per tutto.